

**FRACTIONAL OXIDATION STATE CONTROL OF  
THREE-WAY CATALYST WITH STOICHIOMETRIC  
SPARK-IGNITION NATURAL GAS ENGINES  
INCORPORATING CYLINDER DEACTIVATION**

by

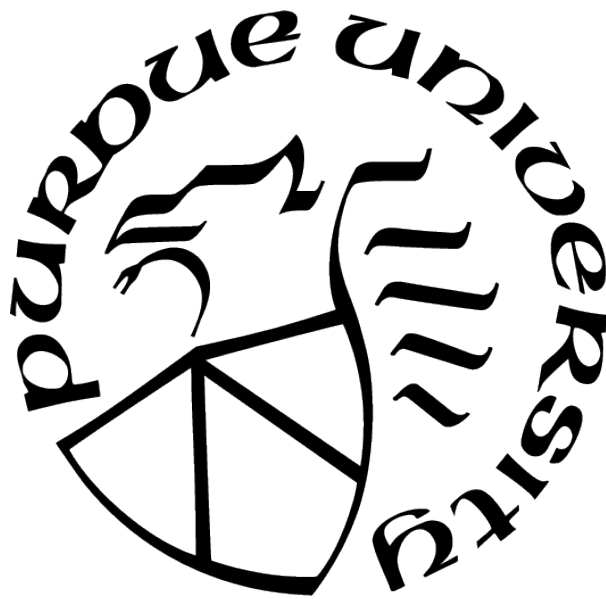
**Yunpeng Xu**

**A Dissertation**

*Submitted to the Faculty of Purdue University*

*In Partial Fulfillment of the Requirements for the degree of*

**Doctor of Philosophy**



School of Mechanical Engineering

West Lafayette, Indiana

December 2022

**THE PURDUE UNIVERSITY GRADUATE SCHOOL  
STATEMENT OF COMMITTEE APPROVAL**

**Dr. Gregory M. Shaver, Chair**

School of Mechanical Engineering

**Dr. George T. C. Chiu**

School of Mechanical Engineering

**Dr. Peter H. Meckl**

School of Mechanical Engineering

**Dr. Stanislaw H. Zak**

School of Electrical and Computer Engineering

**Approved by:**

**Dr. Nicole Key, Associate Head for Graduate Studies**

School of Mechanical Engineering

## ACKNOWLEDGMENTS

The work presented in the thesis consists of two projects, one being funded by U.S. Department of Energy and in collaboration with Cummins Inc., and the other being funded by Cummins Inc. It would have not been possible without the collaboration and support from numerous Cummins Colleagues, including but not limited to Dr. Carlos Lana, Dr. Dheeraj Gosala, Dr. Dat Le, Akash Desai, and Timothy Shipp from Cummins Inc.

Part of the work in the thesis has been jointly accomplished and/or assisted by former graduate students Dr. Xu Zhang and Michael Anthony, and current graduate students Doni Thomas and Adil Shaikh. I would also like to thank Weijin Qiu and Shubham Ashta for your helps from time to time - Those mean a lot to me.

Sincere thanks to Dr. George Chiu, Dr. Peter Meckl, and Dr. Stanislaw Zak to be in my advisory committee. Special thanks to Dr. Gregory Shaver to be my research advisor. I'm grateful to have joined "Shaver Group" and learned a lot from you both academically and personally. You are a super charming person to look up to. It is my honor and pleasure to work with your wonderful group of people who are willing to share and help each other, with whom I also developed true friendships.

I'd also like to thank some people outside of Shaver Group to whom I owe a lot. Thank you, Dr. Bin Yao, for introducing me into Purdue and sharing your knowledge and insights. Thank you, Jie Wang, for your sincere talks and guidance; you are a big brother to me. Thank you, Dr. Jeffrey Shelton, for introducing me into my first grader/TA job and your guidance being a great lecturer yourself. Thank you, Zeshen Chen and Cheng Ji, for your supports and camaraderie in the old days.

The last paragraph belongs to my family. My parents and in-laws, Xiaoming Xu, Xuemei Wang, Yuan Liu, and Wenjuan Wang, you never doubt me and always encourage me to pursue my career. My dear, dear wife, Mingmin Liu, I can't wait to start the new chapter with you.

# TABLE OF CONTENTS

LIST OF TABLES . . . . .	7
LIST OF FIGURES . . . . .	8
ABBREVIATIONS . . . . .	12
ABSTRACT . . . . .	14
1 INTRODUCTION . . . . .	16
2 TWC MODELLING AND EMISSION CONTROL . . . . .	23
2.1 Dynamic, control-oriented TWC oxygen storage model . . . . .	23
2.2 Robust controller design . . . . .	24
2.3 Extended Kalman filter design . . . . .	28
2.4 Simulation setup . . . . .	31
2.5 Control strategies . . . . .	32
2.5.1 Strategy 1: Constant $\lambda_{ref}$ Control . . . . .	33
2.5.2 Strategy 2: Inner Loop AFR Control + Baseline Outer Loop Control . . . . .	33
2.5.3 Strategy 3: Inner Loop AFR Control + Binary Outer Loop Control . . . . .	34
2.5.4 Strategy 4: Inner AFR Control + PI Outer Loop Control with EKF . . . . .	35
2.5.5 Strategy 5: Inner AFR Control + Robust Outer loop Control with EKF . . . . .	36
2.6 Otto-FTP drive cycle . . . . .	36
2.7 Fuel cut-off . . . . .	37
2.8 Model calibration . . . . .	38
Find the saturation point of the air flow rate $W_{air}$ , i.e., $f_{sat}$ . . . . .	38
Find the effective TWC1 oxygen capacity, i.e., $C$ . . . . .	40
Find $a_L$ , $b_L$ , $a_R$ , $b_R$ , $\alpha_L$ , and $\alpha_R$ . . . . .	41
2.9 Sensor measurements, FOS status and their effect on instantaneous emission . . . . .	43
2.9.1 Controllers' performances for engine with fuel cut-off, during warm cycle . . . . .	43
Strategy 1: Constant $\lambda_{ref}$ Control . . . . .	43



	Strategy 2: Inner Loop AFR Control + Baseline Outer Loop Control	46
	Strategy 3: Inner Loop AFR Control + Binary Outer Loop Control	50
	Strategy 4: Inner AFR Control + PI Outer Loop Control with EKF	50
	Strategy 5: Inner AFR Control + Robust Outer loop Control with EKF	51
2.9.2	Comparison of engine with vs. without fuel cut-off, Warm cycle	52
	Strategy 1	53
	Strategy 5	55
	Fuel consumption and $CO_2$ emission	55
2.9.3	Comparison between Cold cycle vs. Warm cycle, with fuel cut-off	56
2.10	Cumulative emission comparison	58
3	NATURAL GAS SI ENGINE MODELLING	65
3.1	Project background	65
3.2	Cummins B6.7N engine	65
	3.2.1 AFR controller	68
	3.2.2 Intake throttle controller	68
	3.2.3 EGR fraction controller	68
	3.2.4 Boost pressure controller	68
3.3	Measurement system	68
	3.3.1 dSPACE	69
	3.3.2 Calterm	69
	3.3.3 Indicom Indicating software	69
	3.3.4 Power Test Dynamometer	69
3.4	GT-Power engine modelling	70
3.5	Engine fuel map and Tested operations	73
3.6	Burn rate calculation from measured cylinder pressures	73
	3.6.1 Closed volume analysis	74
	3.6.2 Three pressure analysis	75
	Single cylinder setup	77
	Multiple cylinder setup	80

3.6.3	Comparison of different pressure analysis methods . . . . .	81
3.6.4	TPA multi-cylinder setup: Additional observations . . . . .	85
3.7	GT model calibration and comparison with test cell engine . . . . .	88
3.7.1	Operating condition, pressures, and temperatures . . . . .	89
3.7.2	Engine efficiencies and mean effective pressures . . . . .	96
4	NATURAL GAS VARIABLE VALVE ACTUATION . . . . .	105
4.1	Variable Valve Actuation Technology . . . . .	105
4.2	Intake Valve Closure Modulation . . . . .	105
4.3	Cylinder de-Activation . . . . .	116
4.4	CDA on TWC emission control . . . . .	122
4.4.1	CDA on TWC's FOS variation . . . . .	123
4.4.2	CDA on emissions during fuel-cut events . . . . .	128
5	SUMMARY AND FUTURE WORK . . . . .	143
5.1	Summary . . . . .	143
5.2	Future work . . . . .	145
	REFERENCES . . . . .	146
	VITA . . . . .	148

## LIST OF TABLES

3.1	Cummins B6.7N engine specifications. . . . .	67
3.2	Tested baseline operating points. . . . .	73
3.3	GT-Power model checklist. . . . .	88
4.1	Fuel consumption reduction - CDA modulation, at 1300rpm. . . . .	118
4.2	Fuel consumption reduction - CDA modulation, at 1000rpm. . . . .	118
4.3	Fuel consumption reduction - CDA modulation, at 1600rpm. . . . .	119
4.4	Fuel consumption reduction - CDA modulation, at 1300rpm. . . . .	123
4.5	Changes on the fuel consumption under Otto-FTP cycle, after CDA implementation compared to before CDA, during fuel-cut events only. . . . .	130
4.6	Changes on the $CO_2$ emission under Otto-FTP cycle, after CDA implementation compared to before CDA, during fuel-cut events only. . . . .	132
4.7	Changes on the tailpipe emissions under Otto-FTP cycle, after CDA implementation compared to before CDA, during fuel-cut events only. . . . .	133
4.8	Changes on the fuel consumption under Otto-FTP cycle, after CDA implementation compared to before CDA. . . . .	136
4.9	Changes on the $CO_2$ emission under Otto-FTP cycle, after CDA implementation compared to before CDA. . . . .	137
4.10	Changes on the tailpipe emissions under Otto-FTP cycle, CDA during fuel-cut events only full CDA, compared to without CDA. . . . .	138
4.11	Changes on the fuel consumption under Otto-FTP cycle, after CDA implementation compared to before CDA, for engine without fuel-cut. . . . .	139
4.12	Changes on the $CO_2$ emission under Otto-FTP cycle, after CDA implementation compared to before CDA, for engine without fuel-cut. . . . .	140
4.13	Changes on the tailpipe emissions under Otto-FTP cycle, with full CDA compared to without CDA, for engine without fuel-cut. . . . .	142

## LIST OF FIGURES

1.1	Powertrain solutions with respect to $CO_2$ & $NO_x$ emissions [2] . . . . .	17
1.2	Emissions before (dashed) and after (solid) the catalyst . . . . .	18
2.1	MISO Robust Controller Design. . . . .	25
2.2	Proposed Control Architecture. . . . .	26
2.3	Original controller vs. simplified lower-order controller. . . . .	28
2.4	TWC Structure. . . . .	32
2.5	HEGO sensor mapping: Voltage $\sim \lambda$ . . . . .	33
2.6	Control Strategy 1. . . . .	34
2.7	Control Strategy 2. . . . .	34
2.8	Control Strategy 3. . . . .	35
2.9	Control Strategy 4. . . . .	36
2.10	Engine's reference torque and speed for Otto-FTP drive cycle. . . . .	37
2.11	$\lambda_{up}$ , $\lambda_{dn}$ and TWC1's $FOS$ under different air flow rate - Triangular input. . . . .	39
2.12	$\lambda_{up}$ , $\lambda_{dn}$ and TWC1's $FOS$ under different air flow rate - Square input. . . . .	39
2.13	$\lambda_{up}$ , $\lambda_{dn}$ and TWC1's $FOS$ under extremely high work loads - Square input. . . . .	40
2.14	TWC1's $FOS$ and $O_2$ before and after TWC1 - Square input. . . . .	42
2.15	Sensor measurements for Strategy 1 - Warm cycle. . . . .	44
2.16	TWC1's & TWC2's $FOS$ for Strategy 1 - Warm cycle. . . . .	44
2.17	Instantaneous emissions for Strategy 1 - Warm cycle. . . . .	45
2.18	Sensor measurements for Strategy 2 - Warm cycle, with fuel cut. . . . .	46
2.19	TWC1's & TWC2's $FOS$ for Strategy 2 - Warm cycle, with fuel cut. . . . .	47
2.20	Instantaneous emissions for Strategy 2 - Warm cycle, with fuel cut. . . . .	47
2.21	Strategy 1 - 3000s $\sim$ 3200s, Warm cycle, with fuel cut. . . . .	48
2.22	Strategy 2 - 3000s $\sim$ 3200s, Warm cycle, with fuel cut. . . . .	49
2.23	Strategy 3 - 3000s $\sim$ 3200s, Warm cycle, with fuel cut. . . . .	51
2.24	Strategy 4 - 3000s $\sim$ 3200s, Warm cycle, with fuel cut. . . . .	52
2.25	Strategy 5 - 3000s $\sim$ 3200s, Warm cycle, with fuel cut. . . . .	53
2.26	Strategy 1 - 3000s $\sim$ 3200s, Warm cycle, without fuel cut. . . . .	54

2.27	Strategy 5 - 3000s ~3200s, Warm cycle, without fuel cut. . . . .	56
2.28	Fuel Consumption during Warm cycle - Fuel cut vs. No Fuel cut. . . . .	57
2.29	$CO_2$ emission during Warm cycle - Fuel cut vs. No Fuel cut. . . . .	57
2.30	Strategy 5 - 0s ~200s, Cold cycle, with fuel cut. . . . .	58
2.31	Strategy 5 - 2400s ~2600s, Warm cycle, with fuel cut. . . . .	59
2.32	Emission comparison for engine with fuel cut-off. . . . .	61
2.33	Emission comparison for engine without fuel cut-off. . . . .	62
2.34	Weighted Otto-FTP emission for engine with fuel cut-off. . . . .	63
2.35	Weighted Otto-FTP emission for engine without fuel cut-off. . . . .	63
3.1	Cummins B6.7N spark-ignition natural gas engine. . . . .	66
3.2	Engine schematics. . . . .	67
3.3	GT-Power engine model. . . . .	71
3.4	Engine fuel map and Tested baseline operating points (circled). . . . .	73
3.5	Closed volume analysis (CPOA) setup. . . . .	74
3.6	CPOA at rated (2400rpm, 543 ft-lbf) - Cylinder #1. . . . .	76
3.7	Three pressure analysis (TPA), Single cylinder setup. . . . .	78
3.8	TPA single cylinder at rated (2400rpm, 543 ft-lbf) - Cylinder #1. . . . .	79
3.9	Three pressure analysis (TPA), Multi-cylinder setup. . . . .	80
3.10	TPA multi cylinder at rated (2400rpm, 543 ft-lbf) - Cylinder #1. . . . .	82
3.11	TPA multi cylinder at rated (2400rpm, 543 ft-lbf) - All cylinders. . . . .	83
3.12	Comparison of different pressure analysis methods at rated (2400rpm, 543 ft-lbf) - Cylinder #1. . . . .	84
3.13	Comparison of different cylinders using TPA multi cylinder method at rated (2400rpm, 543 ft-lbf). . . . .	86
3.14	Comparison using TPA multi cylinder method at different operations - Cylinder #1. . . . .	87
3.15	Engine speed: GT Model vs. Test Cell. . . . .	90
3.16	Brake torque: GT Model vs. Test Cell. . . . .	90
3.17	Mass air flow: GT Model vs. Test Cell. . . . .	91
3.18	Mass fuel flow: GT Model vs. Test Cell. . . . .	92
3.19	Brake specific fuel consumption: GT Model vs. Test Cell. . . . .	93

3.20	Intake manifold pressure: GT Model vs. Test Cell. . . . .	94
3.21	Intake manifold temperature: GT Model vs. Test Cell. . . . .	94
3.22	Average peak in-cylinder pressure: GT Model vs. Test Cell. . . . .	95
3.23	Turbine inlet pressure: GT Model vs. Test Cell. . . . .	95
3.24	Turbine inlet temperature: GT Model vs. Test Cell. . . . .	96
3.25	LogP ~LogV diagram demonstration. . . . .	97
3.26	Closed cycle efficiency: GT Model vs. Test Cell. . . . .	98
3.27	Open cycle efficiency: GT Model vs. Test Cell. . . . .	99
3.28	Mechanical efficiency: GT Model vs. Test Cell. . . . .	100
3.29	Brake thermal efficiency: GT Model vs. Test Cell. . . . .	101
3.30	Friction mean effective pressure: GT Model vs. Test Cell. . . . .	102
3.31	Absolute pumping mean effective pressure: GT Model vs. Test Cell. . . . .	103
3.32	Gross indicated mean effective pressure: GT Model vs. Test Cell. . . . .	103
3.33	Net indicated mean effective pressure: GT Model vs. Test Cell. . . . .	104
4.1	VVA standalone system in test cell. . . . .	106
4.2	VVA installation on engine in test cell. . . . .	107
4.3	Intake & Exhaust valve lift profiles. . . . .	108
4.4	Early & Late intake valve closure (IVC). . . . .	108
4.5	Operating condition - IVC modulation. . . . .	109
4.6	Air & Fuel flows - IVC modulation. . . . .	110
4.7	Brake specific fuel consumption - IVC modulation. . . . .	110
4.8	Volumetric efficiency - IVC modulation. . . . .	111
4.9	Pressures and temperatures - IVC modulation. . . . .	112
4.10	Mean effective pressures - IVC modulation. . . . .	113
4.11	LogP~LogV at 1300rpm, 111ft-lbf - IVC modulation. . . . .	114
4.12	Engine efficiencies - IVC modulation. . . . .	115
4.13	Cylinder de-activation modes. . . . .	117
4.14	Air & Fuel flows - CDA modulation, at 1300rpm. . . . .	118
4.15	Brake specific fuel consumption - CDA modulation. . . . .	119
4.16	Pressures and temperatures - CDA modulation. . . . .	120

4.17	LogP~LogV at 1300rpm, 50ft-lbf - CDA modulation. . . . .	121
4.18	Engine efficiencies - CDA modulation. . . . .	122
4.19	Parameter variations with CDA modulation, under 1300 rpm and 50 ft-lbf. . . .	125
4.20	Instantaneous emissions with CDA modulation, under 1300 rpm and 50 ft-lbf. .	126
4.21	Parameter variations with CDA modulation, under 1300 rpm and 50 ft-lbf. . . .	127
4.22	Fuel consumption under Otto-FTP cycle, without CDA vs. with CDA of 80% flow during fuel-cut events. . . . .	129
4.23	Tailpipe emissions under Otto-FTP cycle, without CDA vs. with CDA during fuel-cut events. . . . .	131
4.24	Fuel consumption under Otto-FTP cycle, without CDA vs. with various CDA during fuel-cut events. . . . .	132
4.25	CO <sub>2</sub> emission under Otto-FTP cycle, without CDA vs. with various CDA during fuel-cut events. . . . .	133
4.26	Tailpipe emissions under Otto-FTP cycle, with CDA of 70% flow during fuel-cut events. . . . .	134
4.27	Tailpipe emissions under Otto-FTP cycle, with CDA of 60% flow during fuel-cut events. . . . .	135
4.28	Fuel consumption under Otto-FTP cycle, without CDA vs. with CDA during fuel-cut events only vs. with full CDA. . . . .	136
4.29	CO <sub>2</sub> emission under Otto-FTP cycle, without CDA vs. with CDA during fuel-cut events only vs. with full CDA. . . . .	137
4.30	Tailpipe emissions under Otto-FTP cycle, with full CDA. . . . .	138
4.31	Fuel consumption under Otto-FTP cycle, without CDA vs. with full CDA, for engine without fuel-cut. . . . .	139
4.32	CO <sub>2</sub> emission under Otto-FTP cycle, without CDA vs. with full CDA, for engine without fuel-cut. . . . .	140
4.33	Tailpipe emissions under Otto-FTP cycle, without CDA vs. with full CDA, for engine without fuel-cut. . . . .	141

## ABBREVIATIONS

SI	Spark Ignition
CI	Compression Ignition
IC Engine	Internal Combustion Engine
CNG	Compressed Natural Gas
AFR	Air-Fuel Ratio
$\lambda$	Air-Fuel Equivalence Ratio
TWC	Three-Way Catalyst
TWC1	First (half of) TWC in series
TWC2	Second (half of) TWC in series
FOS	Fractional Oxidation State
UEGO	Universal Exhaust Gas Oxygen (Sensor)
HEGO	Heated Exhaust Gas Oxygen (Sensor)
Stoich.	Stoichiometry
OLC	Outer Loop Controller
RC	Robust Controller
EKF	Extended Kalman-Filter
CR	Compression Ratio
ECM	Engine Control Module
Dyno	Dynamometer
GT	Gamma Technologies
CPOA	Cylinder Pressure Only Analysis / Closed Volume Analysis
TPA	Three Pressure Analysis
EGR	Exhaust Gas Re-circulation
CAC	Charge Air Cooler
BSFC	Brake Specific Fuel Consumption
Veff	Volumetric Efficiency
BMEP	Brake Mean Effective Pressure
FMEP	Friction Mean Effective Pressure



GIMEP	Gross Indicated Mean Effective Pressure
PMEP	Pumping Mean Effective Pressure
NIMEP	Net Indicated Mean Effective Pressure
PCP	Peak Cylinder Pressure
CCE	Closed Cycle Efficiency
OCE	Open Cycle Efficiency
ME	Mechanical Efficiency
BTE	Brake Thermal Efficiency
VVA	Variable Valve Actuation
IVO	Intake Valve Opening
IVC	Intake Valve Closure
EVO	Exhaust Valve Opening
EVC	Exhaust Valve Closure
CDA	Cylinder De-Activation

## ABSTRACT

A novel two-loop estimation and control strategy is proposed to reduce the natural gas (NG) spark-ignition (SI) engine tail pipe emissions, with focus on the outer loop development. In the outer loop, an fractional oxidation state (FOS) estimator consisting of a three-way catalyst (TWC) model and an extended Kalman-filter is used to estimate the real-time TWC's FOS, and a robust controller is used to control the first-half TWC's FOS by manipulating the desired engine  $\lambda$  (i.e., air-fuel equivalence ratio;  $\lambda=1$  at stoichiometry). The outer loop estimator and controller are combined with an industry-production baseline inner loop controller, which controls the engine  $\lambda$  based on the desired  $\lambda$  value. This novel two-loop control strategy reduces more  $CH_4$  and  $NO_x$  emissions over no-outer-loop control strategy and the conventional two-loop control strategies through simulation.

Engine with and without fuel cut-off are both investigated. Although fuel cut-off brings better fuel economy, it also over-oxidizes the TWC during fuel cut events, which makes the FOS-based controller's competence in  $NO_x$  reduction over non-FOS-based controllers less significant. By comparing simulation results with and without fuel cut-off, it shows huge potential for much better emission result if fuel cut-off's side effect can be alleviated. Considering that fuel cut-off generally being cutting engine fueling during zero load periods and introducing unreacted oxygen into the after-treatment system, the best way of dealing with the issue is to cut off or reduce the oxygen input to the TWC during those events. Several advanced engine technologies such as cylinder deactivation and exhaust gas re-circulation are good candidates to approach this issue.

An industry-production Cummins B6.7N natural gas SI engine was installed in the Ray W. Herrick Laboratories for study of variable valve actuation (VVA) technology, for the purpose of evaluating/improving SI engine's fuel efficiency, emission reduction, and engine knock resistance. A one-dimensional, physics-based natural gas SI engine model was investigated and calibrated in GT-Power software. To calculate the burn rates in the cylinder, three different pressure analysis methods were investigated and implemented. It is observed that all six cylinders' pressure curves are different, which in turn render different burn rates cylinder-to-cylinder. Cylinder with a higher peak cylinder pressure has a faster burn rate.

Each operating condition has its unique pressure curve, and their burn rates are different under different operating conditions. Considering that the burn rate profile can vary cylinder-to-cylinder and operation-to-operation, to make the GT combustion model work for a larger range of loads, a fixed burn rate model may help in the preliminary research phase, but a predictive combustion model is more preferable.

The GT-Power model's VVA capability is investigated, where intake valve closure (IVC) modulation and cylinder de-activation (CDA) are built and analyzed. To mitigate TWC's over-oxidation issue during engine's fuel cut-off events, the CDA is implemented and simulated to demonstrate its benefit on further emission and fuel consumption reductions.

# 1. INTRODUCTION

There are about 2 billion internal combustion (IC) engines in use in the world today, in fields including transportation, electricity generation and power supplies. It has been almost 150 years since the first spark-ignited engine was developed by Nicholas Otto in 1876. In the long history of engine development, countless numbers of technologies are invented and improved for better engine performance, better manufacturing quality, lower fuel consumption, better fuel options, and less pollution productions, etc.[1] There are two major types of internal combustion engines: spark-ignition (SI) and compression-ignition (CI). Spark-ignition engines generate combustion in cylinder chambers by igniting the spark plugs; while compression-ignition engines don't have spark plugs and start combustion themselves under high chamber pressure. The work in the thesis has been all based on spark-ignition type engines, namely a 4-stroke natural gas engine and its after-treatment system.

The majority of IC engines in vehicles that are actively used today are powered by either gasoline or diesel. Numerous researches have been conducted on gasoline/ diesel IC engines worldwide for decades to achieve improvements mentioned previously. However, as the U.S. governors and public agencies (especially EPA, Environmental Protection Agency, and CARB, California Air Resources Board) place more and more stringency on emissions of conventional-nonrenewable-fuel powered engines, namely traditional gasoline and diesel, the automobile industry in general invests more and more on new power solutions for next generation vehicles. The two major long-term approaches taken by automotive industry are either developing alternative vehicle engine such as electric batteries and fuel cells, or looking for more environmental friendly fuel sources, natural gas being one of them (Fig. 1.1).

The advantages of natural gas as an alternative fuel in the U.S. include but not are limited to its domestic availability, established distribution network, relatively low cost, and emission benefits. But it can also bring some new issues that are worth studying. One of the most discussed issues is tail-pipe emission pollution.  $HC$  emission in gasoline / diesel engines contains low methane ( $CH_4$ ), while  $HC$  emission in NG engines is mostly  $CH_4$ , which requires a higher temperature for  $HC$  oxidization to occur, and can potentially aggravate the three-way catalyst (TWC) aging phenomenon. To ensure the TWC model's

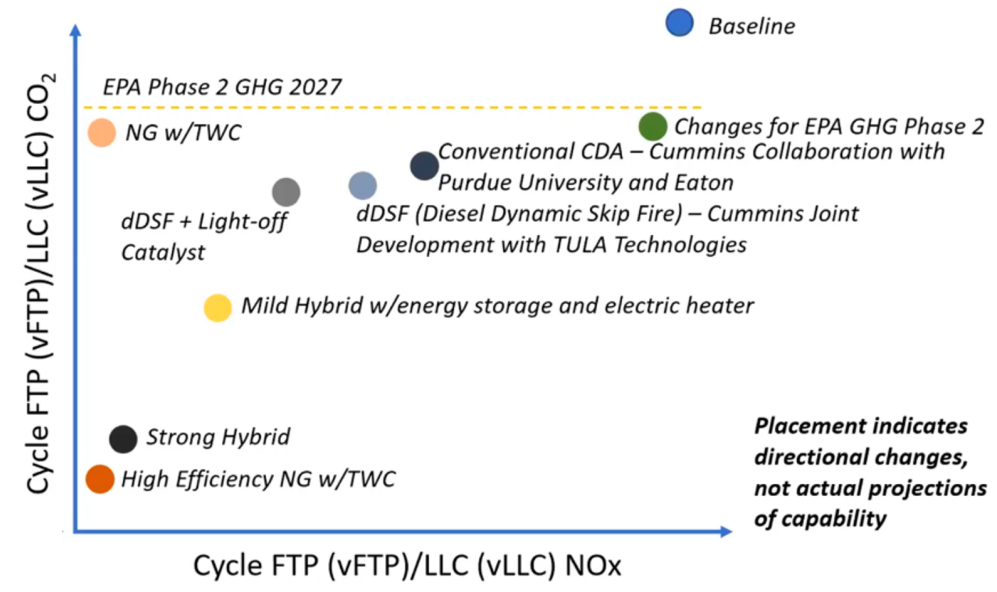


**Figure 1.1.** Powertrain solutions with respect to  $CO_2$  &  $NO_x$  emissions [2]

accuracy over time, especially for advanced feedback control strategies, a model observer is expected to capture the change in parameters. Furthermore,  $CH_4$  oxidization requires higher amounts of platinum group metal (PGM) loadings [3], which increases NG engine's TWC size and cost. Natural gas's comparatively higher compression ratio (also comes with higher in-cylinder pressure) and higher working temperature lead to higher  $NO_x$  emissions than gasoline engines; To help mitigate the issue, a slightly richer condition may be preferred, but it could also introduce more  $NH_3$ , which poses a significant trade-off among engine performance, exhaust emission, and fuel consumption [4].

The three-way-catalyst (TWC) is the most commonly used after-treatment system in SI engines. Consisting of Cerium oxides and precious metals, the TWC reacts with the three major pollutants coming out of the engine, which are carbon monoxide ( $CO$ ), unburnt hydrocarbons ( $UHC$ ) and nitrogen oxides ( $NO_x$ ). There are reduction reactions when the exhaust gas passing through TWC is in lean condition, and oxidation reactions when the exhaust gas is in rich condition. Therefore, TWC works as a buffer to store or release oxygen. The reductants  $UHC$  and  $CO$  can be oxidized into carbon dioxide ( $CO_2$ ) and water ( $H_2O$ ), while the oxidant  $NO_x$  can be reduced into nitrogen ( $N_2$ ) and  $CO_2$  by  $CO$ .

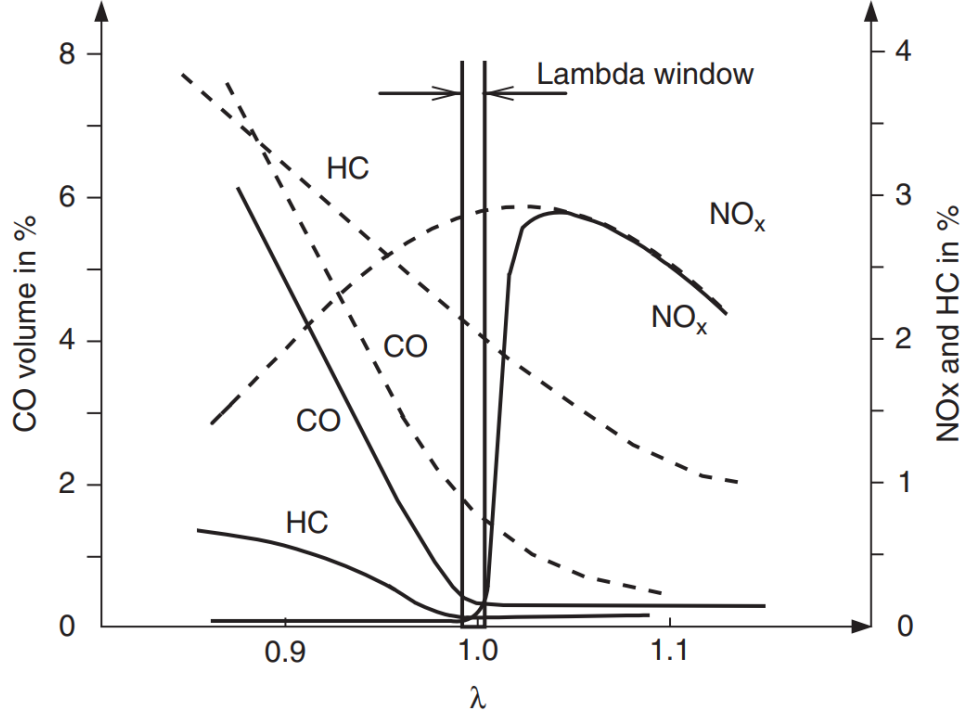


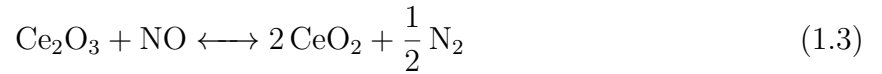
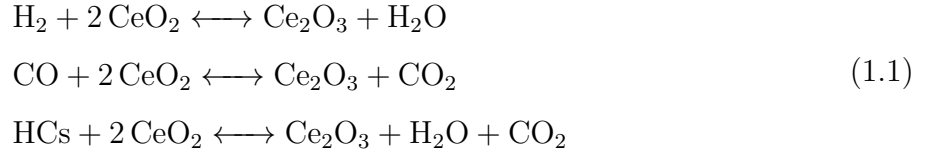
**Figure 1.2.** Emissions before (dashed) and after (solid) the catalyst

The air-fuel-ratio (AFR) window for achieving both oxidation and reduction simultaneously and effectively is very narrow, which requires a highly accurate AFR control system [5]. Fig. 1.2 shows a typical SI engines' emissions of  $CO$ ,  $UHC$  and  $NO_x$  before and after TWC, with respect to engine  $\lambda$ , for steady flow operation. When the absolute difference between actual  $\lambda$  and stoichiometry (where  $\lambda$  is typically 1) is beyond the  $\lambda$  window, the TWC conversion efficiency for certain gases is greatly reduced.

The performance of the TWC can change slowly over its lifetime due to the aging issue. This issue can be caused by poisoning, i.e., a deactivation of the catalytic activity by components such as sulfur or oil additives. Another possible issue is thermal aging, which leads to sintering of the porous catalytically active material and the loss of dispersion of the noble metals. Such issues contribute to a reduced catalytically active surface over time and thus worsen the TWC capability [6].

The emission conversion rate of the TWC depends not only on the AFR of the engine-out exhaust gas, but also on the catalyst state, which is determined by the temperature and the

real-time storage levels of the different species inside the TWC [6]. Today's TWC consists of precious metals and metal oxides. The precious metals catalyze the reactions and metal oxides store oxygen in lean conditions and release oxygen in rich conditions. Oxygen storage components inside TWC, such as Ceria or Ceria and Zirconia solution, react with exhaust gases through reduction and oxidation reactions [7]. Reduction reactions using  $H_2$ ,  $CO$  and  $UHC$  are shown in (1.1), while oxidation reaction when  $O_2$  is exposed to the reduced Ceria is shown in (1.2). Some literature also considers  $NO_x$  as an oxidant and react with reduced Ceria as in (1.3) [8].



Previous researches have found that the emission reduction performance of TWC can be further improved by proper control of the TWC's fractional oxidation state (FOS) [9], which can also be called OSC (oxygen storage capacity) or ROL (relative oxygen level) in other literature. Since TWC takes effect by reduction and oxidation of Ceria, its FOS is typically represented as in (1.4).

$$FOS = \frac{\text{Stored } O_2}{\text{Total } O_2 \text{ capacity}} = \frac{2 [CeO_2]}{2 [CeO_2] + [Ce_2O_3]} \quad (1.4)$$

However, due to the insufficiency of sensors in after-treatment system, a model is typically required to estimate the FOS. An inaccurate model can lead to inaccurate estimation, thus limits the control performance. There have been researches on developing detailed chemical and thermodynamic-based models to describe the complex reactions inside TWC, by a set of partial differential equations (PDEs) in time and space [7], [9]. Although such models could provide relatively good FOS estimations, they are not well-suitable for controller designs due

to their complexity and high dimension, which also require a large amount of calibrations and modifications in model development for any specific TWC.

During transient vehicle operations such as aggressive acceleration or braking, temporary excursions of the air-to-fuel ratio occur due to the different dynamics of the air and fuel paths. As more engines nowadays come with fuel cut-off features for fuel economy /  $CO_2$  reduction concerns, the exhaust gas during fuel cut-off event are mostly pure air, which is a very lean mixture that oxidizes the catalyst surface in TWC. Today's most common TWC feedback control strategies basically use a PI controller on the deviation of the downstream lambda sensor from stoichiometry without considering the oxygen storage dynamics of the catalyst. This can lead to undesired control actions after fuel cut-off phases resulting in  $NO_x$  breakthroughs [10]. When the fuel cut-off events are over,  $NO_x$  spikes can be observed in the TWC outlet emissions.

An advanced control strategy for the TWC can potentially help reduce engine-out emissions, and increase the operating window about the stoichiometric AFR. For a similar performance requirement, control strategies are expected to help reduce catalyst size and cost for optimal system integration. Several TWC control strategies have been studied in literature. A conventional approach is to use a PI controller to correct the engine fueling command by a multiplicative factor based on a single switch-type sensor positioned upstream of the TWC [11]. The controller parameters need to be experimentally identified for specific operating point and the TWC oxygen storage dynamics are not considered in this method. A more advanced TWC control method is to use a cascade control structure based on both TWC upstream and downstream  $\lambda$  sensors. In [12], a fore controller is designed to respond relatively quickly to AFR disturbances on the basis of pre-catalyst UEGO sensor signal and an Aft controller is developed to adjust the setpoint of the fore controller on the basis of both pre-catalyst and post-catalyst UEGO sensors' measurements. In [13], a model predictive controller was designed as the primary control loop within a multi-rate cascade control configuration that adapted the parameters of a postcatalyst HEGO relay controller in an optimal manner using a predictive functional control approach. The relay controller adjusted the target of a delay-compensated feedback controller for the pre-catalyst AFR to maintain the post-catalyst HEGO sensor signal within a specified range of the desired voltage. The



cascade control structure can further be combined with TWC FOS estimators. In [14], a TWC model was developed based on detailed first-principles reaction kinetics, subsequent averaging and model reduction. An outer loop PI controller was designed to control the model predicted TWC oxygen storage level by correcting the engine  $\lambda$  set point and an inner controller was applied to control the engine  $\lambda$  based on the outer loop command.

In Chapter 2, I will expand on the development of a novel two-loop control strategy for the TWC oxygen storage level control with focus on emission pollutant reduction. In the outer loop, an FOS estimator consisting of a TWC model and an extended Kalman-filter was designed to estimate the TWC's real-time FOS and a robust controller was developed to control the TWC's FOS by manipulating the desired engine  $\lambda$ . The outer loop estimator and controller were combined with an existing inner loop controller which controlled the engine  $\lambda$  based on the  $\lambda$  set point. The inner loop control inaccuracies are considered and compensated by the outer loop robust controller, which is different from the conventional TWC control strategies. Then I will expand on simulation results and analyses. To further justify the advantage and necessity of the novel control strategy, several other control strategies are also simulated for emission comparison. The Otto-FTP drive cycle is used in the simulation which consists of both cold cycle and warm cycle. All control strategies show more contribution in the warm cycle mainly because of the unignorable difference in starting temperature between two cycles. Modern engines with fuel cut-off feature introduce more  $NO_x$  emissions than engines without fuel-cut, because of TWC's over-oxidation during fuel-cut events.

Besides the tail-pipe emission, since companies plan to deploy natural gas engines in place of traditional fuel engines, there are some performance gaps that need to be addressed and investigated. In the project that part of this work belongs to, a Cummins 6.7L natural gas SI engine was investigated both software-wise and hardware-wise. This engine is used in medium-duty applications expecting to replace some of the 6.7L diesel engines that have been in both production and development for decades. In order to make the natural gas engine appealing to targeted market and customers, modifications and improvements are required to bring the natural gas engine on par with, if not better than, its diesel predecessor/competitor.

There have been researches within the group for the past decade on 6.7L diesel engine VVA technology developments and the findings have been recognized both industrially by the sponsor and academically by peer researchers. The same VVA technologies are also expected to help improve natural gas engine performance. Therefore, a Cummins 6.7L natural gas engine is installed and tested in the Ray W. Herrick Laboratories, and a GT-Power virtual model is also calibrated with test data, both for the purpose of evaluating the benefits of VVA technology on stoichiometric spark ignited fuel efficiency,  $CO_2$  emissions and knock resistance. Furthermore, it's planned that after the VVA technology is tuned, tested and proven beneficial to the natural gas engine, a continuation to explore requirements and operation of natural gas engines in range extended electric vehicle (REEV) application is advocated, because hybrid powertrain is an inevitable path in the near future. Range extended vehicles are of particular interest with natural gas due to the potential for low  $CO_2$  and  $NO_x$  emission. In Chapter 3, I will expand on the natural gas engine and test cell setup. Then I'll mainly elaborate my work in GT-Power model investigation and calibration. Three burn rate calculation methods and results will be discussed. With the calculated burn rate implemented, I'll present data comparison between GT-Power model and test cell.

In order to maintain stoichiometric condition for three-way catalyst emission control, spark ignited engines are throttled to control air flow at low loads and have reduced efficiency. VVA technologies can be helpful in remedying the issues. IVC (intake valve closure) modulation can be used to reduce effective compression ratio and reduce knock, while CDA (cylinder de-activation) can retain stoichiometric operation without the throttling losses. Additionally with CDA at engine low torque region, the active cylinders can work at a higher pressure and temperature condition which can lead to a reduced gas flow, thus it can be beneficial for alleviating the TWC over-oxidation issue coming from fuel cut-off events. In Chapter 4, I'll expand on the VVA technologies, especially the IVC modulation and CDA modulation, and present some results with analyses and remarks. I'll also implement CDA dynamics on the engine of the TWC emission control work, and demonstrate CDA's benefits on the overall system, especially for the emission reduction and fuel economy.

In the end, I'll talk about my takings on the work presented and my perspectives on challenges and future work in Chapter 5.

## 2. TWC MODELLING AND EMISSION CONTROL

### 2.1 Dynamic, control-oriented TWC oxygen storage model

The control-oriented model is developed based on the model proposed in [15] for FOS controller and observer designs.

$$\frac{dFOS}{dt} = \begin{cases} 0.21 \times f_{sat}(W_{air}) \times \left(1 - \frac{1}{\lambda_{up}}\right) \times \rho(\lambda_{up}, FOS) \times \frac{1}{C} & 0 < FOS < 1 \\ 0 & otherwise \end{cases} \quad (2.1)$$

where  $W_{air}$  is the engine-out mass air flow rate (can also be approximated by the mixture mass flow rate),  $f_{sat}$  is the saturation function of  $W_{air}$ ,  $C$  is the effective TWC oxygen capacity (i.e., the total mass of oxygen that can be stored in the TWC),  $\lambda_{up}$  is the TWC upstream AFR (engine-out AFR) and  $\rho$  describes the exchange of oxygen between the engine-out exhaust and the TWC. The saturation function  $f_{sat}$  is used for mathematical simplicity to describe the phenomenon that the effective TWC oxygen capacity  $C$  increases as flow rate increases at high flow rate [15].  $\rho$  is modeled as a function of  $\lambda_{up}$  and FOS:

$$\rho(\lambda_{up}, FOS) = \begin{cases} \alpha_L \times f_L(FOS) & \lambda_{up} > 1 \\ \alpha_R \times f_R(FOS) & otherwise \end{cases} \quad (2.2)$$

where  $\alpha_L$  and  $\alpha_R$  are the adsorption and desorption rate of oxygen, respectively.  $0 \leq f_L \leq 1$  represents the fraction of oxygen from the engine-out exhaust gas sticking to a site in the TWC, and  $0 \leq f_R \leq 1$  represents the fraction of oxygen being released by the TWC and recombining with the engine-out exhaust gas.  $f_L$  and  $f_R$  are defined as:

$$\begin{aligned} f_L(FOS) &= \frac{e^{g_L(FOS)} - e^{g_L(1)}}{e^{g_L(1)} - 1} \\ f_R(FOS) &= \frac{e^{g_R(FOS)} - 1}{e^{g_R(1)} - 1} \end{aligned} \quad (2.3)$$

where:

$$\begin{aligned} g_L(FOS) &= a_L \times FOS^2 + b_L \times FOS \\ g_R(FOS) &= a_R \times FOS^2 + b_R \times FOS \end{aligned} \quad (2.4)$$

$a_L$ ,  $b_L$ ,  $a_R$  and  $a_R$  are tuning parameters.  $f_L$  is monotonically decreasing with FOS while  $f_R$  is monotonically increasing with FOS, and FOS is bounded by 0 and 1. The term  $0.21 \times f_{sat}(W_{air}) \times (1 - 1/\lambda_{up})$  is the differential total mass of  $O_2$  in the engine-out exhaust gas with respect to stoichiometry.

The  $TWC_{out} \lambda_{dn}$  can be expressed as:

$$\lambda_{dn} = \lambda_{up} - (\lambda_{up} - 1) \times \rho(\lambda_{up}, FOS) \quad (2.5)$$

With the state  $x$  being FOS, the input  $u$  being  $\lambda_{up}$ , the disturbance input  $u_d$  being  $W_{air}$ , and the outputs  $\{y_1, y_2\}$  being  $\{FOS, \lambda_{dn}\}$ , the system can be expressed as:

$$\begin{aligned} \dot{x} &= \begin{cases} 0.21 \times f_{sat}(u_d) \times \left(1 - \frac{1}{u}\right) \times \alpha_L \times f_L(x) \times \frac{1}{C} & 0 < x < 1 \& u > 1 \\ 0.21 \times f_{sat}(u_d) \times \left(1 - \frac{1}{u}\right) \times \alpha_R \times f_R(x) \times \frac{1}{C} & 0 < x < 1 \& u \leq 1 \\ 0 & otherwise \end{cases} \\ y_1 &= x \\ y_2 &= \begin{cases} u - (u - 1) \times \alpha_L \times f_L(x) & u > 1 \\ u - (u - 1) \times \alpha_R \times f_R(x) & u \leq 1 \end{cases} \end{aligned} \quad (2.6)$$

## 2.2 Robust controller design

A robust multi-input-single-output (MISO) outer-loop controller is designed to control the TWC's FOS by manipulating the desired engine  $\lambda$ . Fig. 2.1 shows the control block for the robust controller. The robust controller has 3 inputs, the desired FOS ( $FOS_{des}$ ), EKF estimated FOS ( $FOS_{est}$ ), measured engine-out air flow rate  $W_{air}$  (approximated by the exhaust flow rate  $W_{exh}$ ). Three error/uncertainty blocks, inner AFR control error, TWC model uncertainty, and output measurement errors, are considered in the robust controller. Fig. 2.2 shows the general control architecture for the TWC FOS control. The perturbed closed-loop system has three exogenous inputs, the sensor noises  $n$  (including the TWC upstream sensor noise  $nu_0$  and downstream sensor noise  $n_0$ ), the disturbance input ( $W_{air}$ ) and the reference input ( $FOS_{des}$ ). The two exogenous outputs of the closed-loop system are

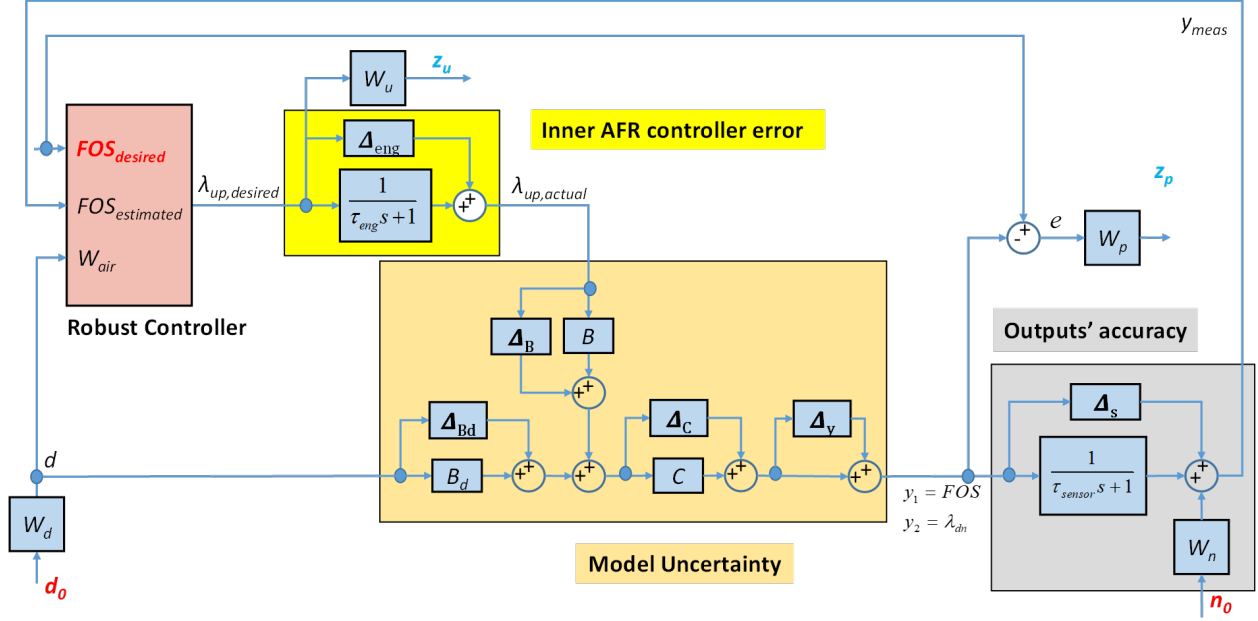


**Figure 2.1.** MISO Robust Controller Design.

the weighted output performance (FOS control error) and the weighted input performance (desired engine  $\lambda$ ).

The inner loop AFR control error is modelled by a first-order approximation:

$$\delta\lambda_{up,act} = \frac{\delta\lambda_{des}}{\tau_{eng}s + 1} (1 + \Delta_{eng}) \quad (2.7)$$

where the time constant  $\tau_{eng}$  is approximated by 0.05s and the frequency-shaped uncertainty  $\Delta_{eng}$  is:

$$\Delta_{eng} = \frac{\frac{1}{20}s + 0.001}{\frac{1}{20 \times 0.01}s + 1} \delta, \text{ where } -1 < \delta < 1 \quad (2.8)$$

The model uncertainty block includes the parametric state-space uncertainty and multiplicative output uncertainty. The parametric uncertainty is to account for the uncertain parameters in the state space model and is expressed as:

$$\delta y_{ss} = C_p(sI - A)^{-1} B_p \delta u + C_p(sI - A)^{-1} B_{pd} \delta u_d \quad (2.9)$$

where the perturbed state space matrices are derived from the model:

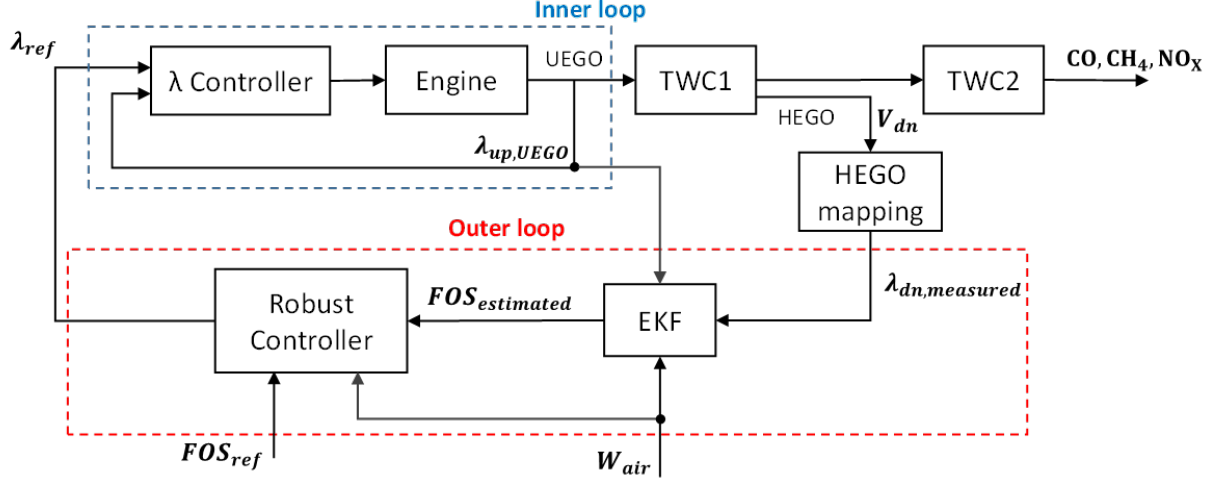


**Figure 2.2.** Proposed Control Architecture.

$$\begin{aligned}
 B_p &= B(x_e, u_e + \Delta u, u_{de} + \Delta u_d) \\
 B_{pd} &= B_d(x_e, u_e + \Delta u, u_{de} + \Delta u_d) \\
 C_p &= C(x_e, u_e + \Delta u, u_{de} + \Delta u_d)
 \end{aligned} \tag{2.10}$$

The multiplicative output uncertainty  $\Delta_y$  is to account for the uncaptured dynamics of the state-space model:

$$\delta y = (1 + \Delta_y) \delta y_{ss} \tag{2.11}$$

The output measurement errors are expressed as:

$$\delta y_{meas} = \frac{\delta y}{\tau_y s + 1} + \delta y \Delta_s + W_n n_0 \tag{2.12}$$

where  $\tau_y$  is the time constant,  $\Delta_s$  is the measurement bias error,  $W_n$  is the noise shaping function and  $n_0$  is noise.

For the FOS estimator, the first-order dynamics and the shaped noise are ignored, i.e.,  $\tau_{y1} = 0$  and  $W_{n1} = 0$ :

$$\delta y_{1,meas} = (1 + \Delta_{s1}) \delta y_1, \text{ where } -0.1 < \Delta_{s1} < 0.1 \tag{2.13}$$

For the TWC downstream lambda sensor, the measurement bias error is ignored, i.e.  $\Delta_{s2}=0$ :

$$\delta y_{2, meas} = \frac{\delta y_2}{\tau_{y2}s + 1} + W_{n2}n_2, \quad (2.14)$$

where  $W_{n2} = 0.024 \times \frac{(\frac{1}{0.18}s+1)(\frac{1}{2.1}s+1)}{(\frac{1}{1.2}s+1)(\frac{1}{9}s+1)(\frac{1}{80}s+1)(\frac{1}{100}s+1)}$ , and  $\tau_{y2} = 0.3s$ .

The following second-order output weighting function is used to shape the FOS control error in the frequency domain (The inverse of  $W_p$  representing the shaped upper bound of the FOS control error):

$$W_p = \left( \frac{\frac{s}{\sqrt{M}} + \omega^*}{s + \omega\sqrt{A}} \right)^2 \quad (2.15)$$

where  $M$  is the maximum error at high frequencies,  $A$  is the steady-state error and  $\omega$  is the frequency where error reaches 100%. The values of these three parameters are listed as follows:  $M = 1$ ,  $A = 0.3$ ,  $\omega = 1rad/s$ .

The input weighting function  $W_u$  is used to set the physical limits of the controlled input.  $W_u$  is modeled as a first-order high-pass filter in the following format:

$$W_u = \frac{\tau_u s + 1}{\frac{\tau_u s}{100} + 1} \quad (2.16)$$

where  $\tau_u = 30ms$  is the actuator response time.

The commanded engine  $\lambda$  is penalized by a factor of 0.01 at high frequencies. A disturbance shaping function  $W_d$  is used to identify the bandwidth of the disturbance input  $W_{air}$ :

$$\delta u_d = \frac{\delta u_{d0}}{\tau_{ud}s + 1} \quad (2.17)$$

where  $\delta u_{d0}$  denotes the normalized disturbance input. The time constant  $\tau_{ud}$  is 0.05s. The robust controller is computed based on the mu-synthesis method. The toolbox “dksyn” for performing DK-iteration in MATLAB is used for the controller synthesis.

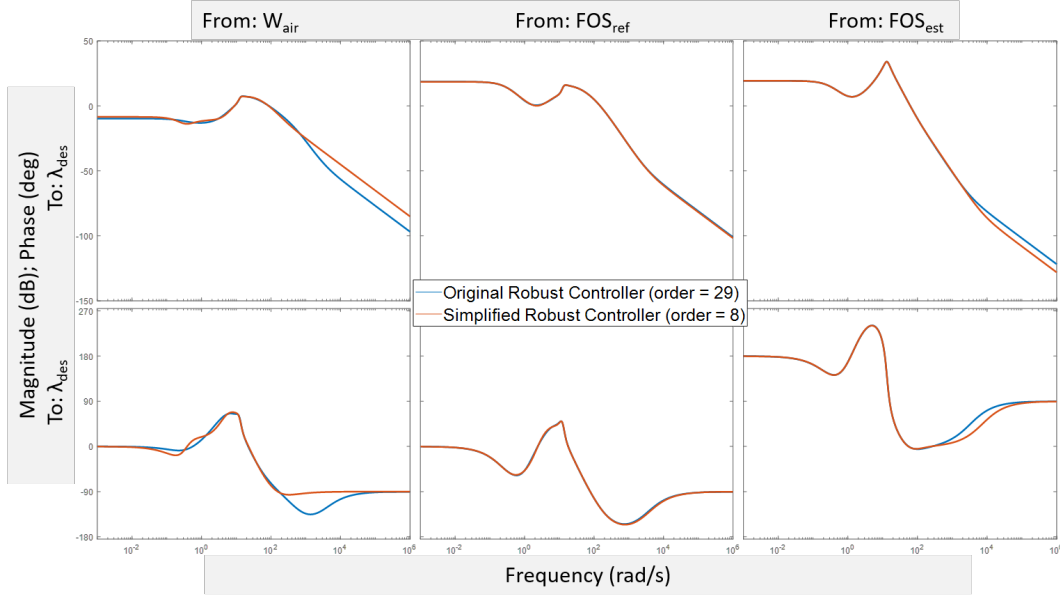


**Figure 2.3.** Original controller vs. simplified lower-order controller.

Since the original synthesized MISO controller's order is relatively too high, it is then reduced by referring to the controller's Hankel singular values. Hankel singular values can be used to quantify the importance of each state in the corresponding input-output map and guide the model reduction by keeping only the first several important states. Fig. 2.3 shows the comparison of the original high-order controller and the simplified controller.

### 2.3 Extended Kalman filter design

In a manner similar to the approach taken in [16], an extended Kalman filter is used as observer to update the model parameters and correct FOS estimation. With change of working condition and TWC aging, model parameters  $\alpha_L$ ,  $\alpha_R$  and  $1/C$  are subject to change over time, which can bring inaccuracy to open-loop model's FOS estimation. Based on  $\lambda_{up}$  and  $\lambda_{dn}$  from sensor measurements, the FOS estimation can be corrected in real-time. The basic equations for a linearized system are:

$$\begin{aligned} \dot{x} &= A(t)x(t) + B(t)u(t) + Nw(t) \\ y &= Cx(t) + Rv(t) \end{aligned} \tag{2.18}$$



These equations consider both measurement and process noises. The variables  $w$  and  $v$  are the zero mean, unit variance, mutually independent Gaussian random variables, and  $N$  and  $R$  are the corresponding square roots of the noise covariances.

The general framework of the EKF for a discrete-time system consists of a prediction step and a correction step. The prediction step estimates based only on previous data. (2.19) represents the predicted state estimate while (2.20) represents the predicted error covariance estimate. The notation  $\hat{x}_{k+1|k}$  means that the estimate of the parameter  $\hat{x}$  at time  $(k+1)T_s$  is based on the observations up to and including at time  $kT_s$ . The time step size,  $T_s$ , was chosen to be 0.01s.

$$\begin{aligned}
\hat{x}_{k+1|k} &= \hat{x}_k + T_s \dot{\hat{x}}_k \\
&= \hat{x}_k + T_s f(\hat{x}_k, u_k) \\
&= \hat{x}_k + T_s (A\hat{x}_k + Bu_k) \\
&= (I + T_s A)\hat{x}_k + T_s Bu_k
\end{aligned} \tag{2.19}$$

$$P_{k+1|k} = A_{k+1} P A_{k+1}^T + N_{k+1} N_{k+1}^T \tag{2.20}$$

In the correction step, (2.21) represents the EKF gain, (2.22) represents the correct state estimation, while (2.23) represents the posterior error covariance.

$$L_{k+1} = P_{k+1|k} C_{k+1}^T (R_{k+1} R_{k+1}^T + C_{k+1}^T P_{k+1|k} C_{k+1})^{-1} \tag{2.21}$$

$$\hat{x}_{k+1} = x_{k+1|k} + L_{k+1} (y_{k+1} - h_{k+1}(\hat{x}_{k+1})) \tag{2.22}$$

$$P_{k+1} = (I - L_{k+1} C_{k+1}) P_{k+1|k} \tag{2.23}$$

To implement the extended Kalman filter, the state(s) of TWC model in (2.6) is augmented from  $FOS$  to  $[FOS, \lambda_{dn}, \alpha_L, \alpha_R, 1/C]^T$ . The control input  $u$  is still  $\lambda_{up,desired}$ , the disturbance input  $u_d$  is still  $W_{air}$ , while the output  $y$  is estimation of  $\lambda_{dn}$ . Then the state space equations for the observer system are as follows:

$$\begin{aligned}\dot{\hat{x}}_1 &= \begin{cases} 0.21 \times \hat{x}_3 \times f_{sat}(u_d) \times (1 - \frac{1}{u}) \times \hat{x}_5 \times f_L(\hat{x}_1) & u > 1, \hat{x}_1 < 1 \\ 0.21 \times \hat{x}_4 \times f_{sat}(u_d) \times (1 - \frac{1}{u}) \times \hat{x}_5 \times f_R(\hat{x}_1) & u \leq 1, \hat{x}_1 > 0 \\ 0 & otherwise \end{cases} \\ \dot{\hat{x}}_2 &= \begin{cases} \frac{1}{C} \times [\hat{x}_2 + u - (u - 1) \times \hat{x}_3 \times f_L(\hat{x}_1)] & u > 1 \\ \frac{1}{C} \times [\hat{x}_2 + u - (u - 1) \times \hat{x}_4 \times f_R(\hat{x}_1)] & u \leq 1 \end{cases} \end{aligned} \quad (2.24)$$

$$\dot{\hat{x}}_3 = 0$$

$$\dot{\hat{x}}_4 = 0$$

$$\dot{\hat{x}}_5 = 0$$

The measured output is  $\hat{y} = \hat{x}_2$ . The discrete-time 5x5 A matrix varies with time. Therefore, A matrix is linearized from nonlinear system at each time step in the following format.

$$A = \begin{bmatrix} A_{11} & 0 & A_{13} & A_{14} & A_{15} \\ A_{21} & A_{22} & A_{23} & A_{24} & 0 \\ 0 & 0 & 0 & 0 & 0 \\ 0 & 0 & 0 & 0 & 0 \\ 0 & 0 & 0 & 0 & 0 \end{bmatrix} \quad (2.25)$$

The elements in the A matrix are represented by the following equations:

$$A_{11} = \begin{cases} 0.21 \times \hat{x}_3 \times f_{sat}(u_d) \times (1 - \frac{1}{u}) \times \hat{x}_5 \times \frac{(2a_L\hat{x}_1+b_L)e^{a_L\hat{x}_1^2+b_L\hat{x}_1}}{e^{a_L+b_L}-1} & u > 1, \hat{x}_1 < 1 \\ 0.21 \times \hat{x}_4 \times f_{sat}(u_d) \times (1 - \frac{1}{u}) \times \hat{x}_5 \times \frac{(2a_R\hat{x}_1+b_R)e^{a_R\hat{x}_1^2+b_R\hat{x}_1}}{e^{a_R+b_R}-1} & u \leq 1, \hat{x}_1 > 0 \\ 0 & otherwise \end{cases} \quad (2.26)$$

$$A_{13} = \begin{cases} 0.21 \times f_{sat}(u_d) \times (1 - \frac{1}{u}) \times \hat{x}_5 \times f_L(\hat{x}_1) & u > 1, \hat{x}_1 < 1 \\ 0 & otherwise \end{cases} \quad (2.27)$$

$$A_{14} = \begin{cases} 0.21 \times f_{sat}(u_d) \times (1 - \frac{1}{u}) \times \hat{x}_5 \times f_R(\hat{x}_1) & u \leq 1, \hat{x}_1 > 0 \\ 0 & otherwise \end{cases} \quad (2.28)$$

$$A_{15} = \begin{cases} 0.21 \times \hat{x}_3 f_{sat}(u_d) \times (1 - \frac{1}{u}) \times \hat{x}_5 \times f_L(\hat{x}_1) & u > 1, \hat{x}_1 < 1 \\ 0.21 \times \hat{x}_4 f_{sat}(u_d) \times (1 - \frac{1}{u}) \times \hat{x}_5 \times f_R(\hat{x}_1) & u \leq 1, \hat{x}_1 > 0 \\ 0 & otherwise \end{cases} \quad (2.29)$$

$$A_{21} = \begin{cases} -\frac{1}{0.3} \times (u - 1) \times \hat{x}_3 \times \frac{(2a_L \hat{x}_1 + b_L) e^{a_L \hat{x}_1^2 + b_L \hat{x}_1}}{e^{a_L + b_L} - 1} & u > 1 \\ -\frac{1}{0.3} \times (u - 1) \times \hat{x}_4 \times \frac{(2a_R \hat{x}_1 + b_R) e^{a_R \hat{x}_1^2 + b_R \hat{x}_1}}{e^{a_R + b_R} - 1} & u \leq 1 \end{cases} \quad (2.30)$$

$$A_{22} = -\frac{1}{0.3} \quad (2.31)$$

$$A_{23} = \begin{cases} -\frac{1}{0.3} \times (u - 1) \times f_L(\hat{x}_1) & u > 1, \hat{x}_1 < 1 \\ 0 & otherwise \end{cases} \quad (2.32)$$

$$A_{24} = \begin{cases} \frac{1}{0.3} \times (1 - u) \times f_R(\hat{x}_1) & u \leq 1, \hat{x}_1 > 0 \\ 0 & otherwise \end{cases} \quad (2.33)$$

The C matrix also varies with time and represents the output, which is always  $\hat{x}_2$ . Therefore, the output matrix C is always given by:

$$C = \begin{bmatrix} 0 & 1 & 0 & 0 & 0 \end{bmatrix} \quad (2.34)$$

## 2.4 Simulation setup

Simulation tests are run under MATLAB/Simulink environment. A chemically thermodynamics based TWC model is built in AVL/Boost and implemented in the Simulink environment. The structure of TWC Boost model is shown in Fig. 2.4. It is a dual-site TWC model developed consisting of two equal sized halves connected in-series based on [7]. The

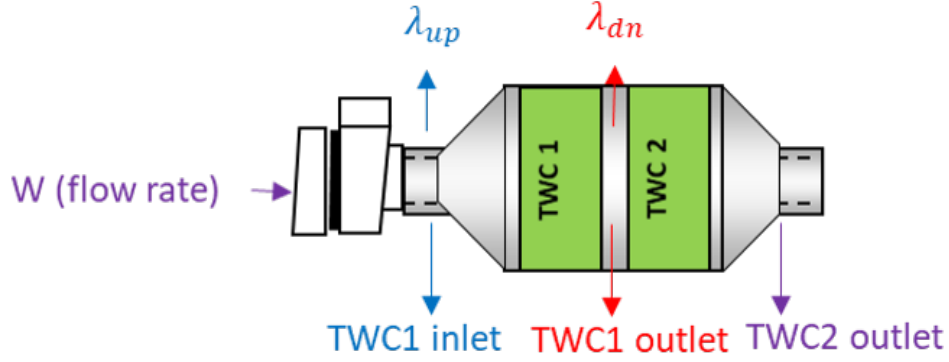


**Figure 2.4.** TWC Structure.

TWC halves are named as “TWC1” and “TWC2” for the rest of the thesis. The TWC Boost model provides exhaust gas data with time for emission analyses and comparisons among various control strategies which will be discussed later in this chapter. In the dual-loop controller that is applied in the work (Fig. 2.2), a pre-existing inner loop AFR controller is used to control the engine  $\lambda$  based on the commanded  $\lambda$  input. Both the inner loop AFR controller and the TWC Boost model are built by our industrial partner. Although no disclosed information is given in terms of the model accuracy in comparison with real product, it’s suggested by industrial partner to use the models as high fidelity truth reference for simulation verification.

Two EGO (exhaust gas oxygen) sensors and one flow rate sensor are used for real-time data measurement. A UEGO sensor is placed upstream the entire TWC and an HEGO sensor is placed downstream the TWC1 for outer loop feedback. The response time of both the UEGO and HEGO sensors is assumed 0.3s. The TWC2 is outside of the outer feedback loop, and used as a passive catalyst for eliminating extra exhaust gas pollutants coming out of TWC1. The final emission data are taken at the Boost model’s TWC2 outlet. A  $\lambda \sim$  Voltage conversion mapping is developed for the HEGO sensor based on existing sensor data sheet, as is shown in Fig. 2.5.

## 2.5 Control strategies

Five different control strategies are tested for emission comparisons.

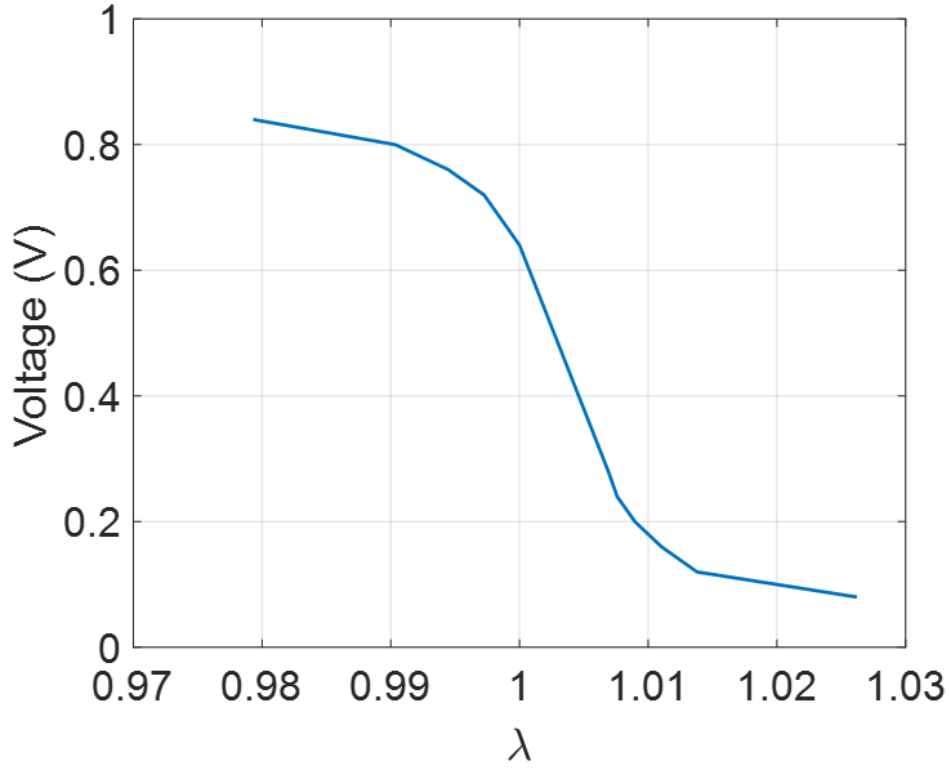


**Figure 2.5.** HEGO sensor mapping: Voltage  $\sim \lambda$ .

### 2.5.1 Strategy 1: Constant $\lambda_{ref}$ Control

In this control strategy, there is no outer loop feedback from the after-treatment (TWC) system, and only the engine block is controlled by a pre-existing inner loop AFR controller (Fig. 2.6).  $\lambda_{ref}$  is set to a constant value (typically the stoichiometric point) to ensure best fuel consumption and least exhaust gas emission. Here the constant  $\lambda_{ref}$  value is set as 0.9944 based on calibration of the high fidelity TWC model. This control strategy serves to show the difference between before and after adding outer loop feedback control strategies.

### 2.5.2 Strategy 2: Inner Loop AFR Control + Baseline Outer Loop Control

In this control strategy, a simplified version of industrially applied PI-based controller is implemented for the outer loop (the TWC after-treatment system), together with the same inner loop AFR controller as in Strategy 1 (Fig. 2.7). By adding outer loop feedback

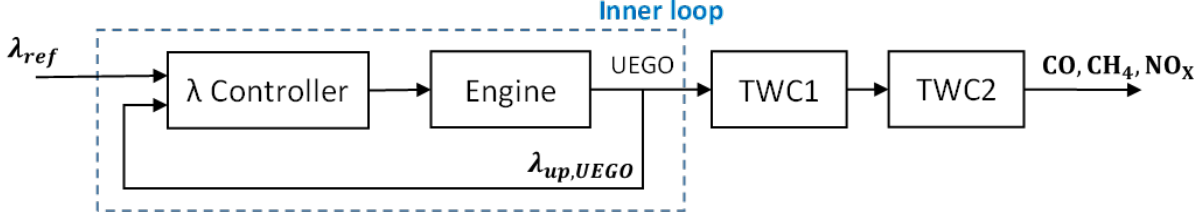


**Figure 2.6.** Control Strategy 1.

control, the desired  $\lambda$  is now determined by the outer loop controller instead of a constant  $\lambda_{ref}$  set point. The outer loop controller generate the desired  $\lambda$  command based on the TWC1 downstream HEGO sensor voltage, the sensor's stoichiometric voltage set point (0.5 V), the TWC1 downstream internal temperature, and the air flow rate. This outer loop controller has been tuned and provided by our industrial partner to serve as a baseline outer loop controller for emission comparison.

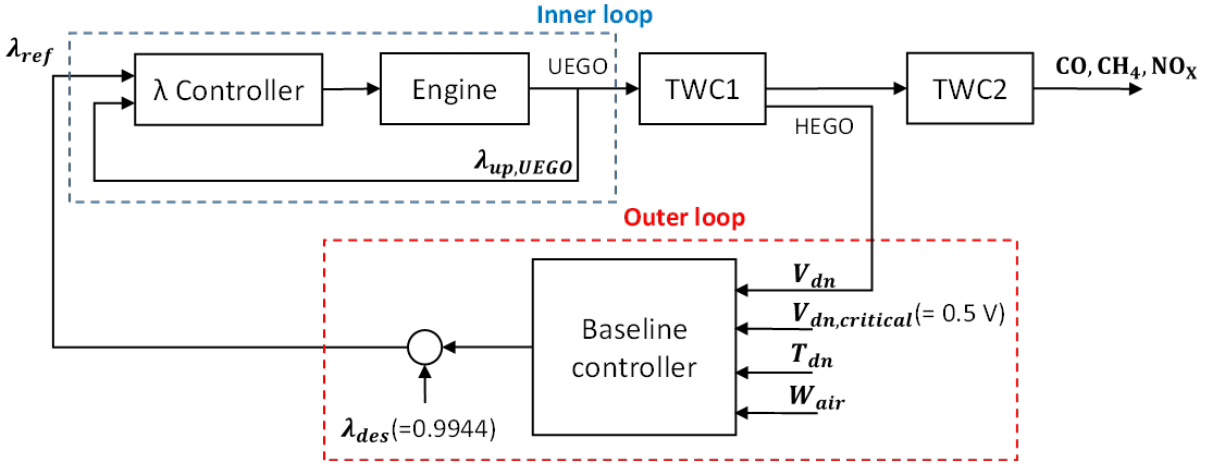


**Figure 2.7.** Control Strategy 2.

### 2.5.3 Strategy 3: Inner Loop AFR Control + Binary Outer Loop Control

In this control strategy, a switch-type HEGO sensor based controller is implemented for the outer loop (Fig. 2.8). The inner loop AFR controller is kept the same for all the control strategies, and the desired  $\lambda$  is determined by the outer loop controller for all the control strategies with outer loop feedback. The TWC1 downstream HEGO sensor voltage

is mapped to the  $\lambda$  value via reverse look-up table based on sensor data sheet (Fig. 2.5). The outer loop controller switches the desired  $\lambda$  command based on the mapped TWC1 downstream  $\lambda$  signal and the  $\lambda_{dn}$  set point. If the mapped HEGO signal is less than the set point ( $\Delta\lambda_{dn} > 0$ ), the outer loop controller reduces the  $\lambda_{ref}$  set point by  $K_P$  to be the desired  $\lambda$  command; Otherwise it increases  $\lambda_{ref}$  by  $K_P$ . This control strategy is the simplest strategy of all candidates to implement and is used for comparison with more complicated control strategies.

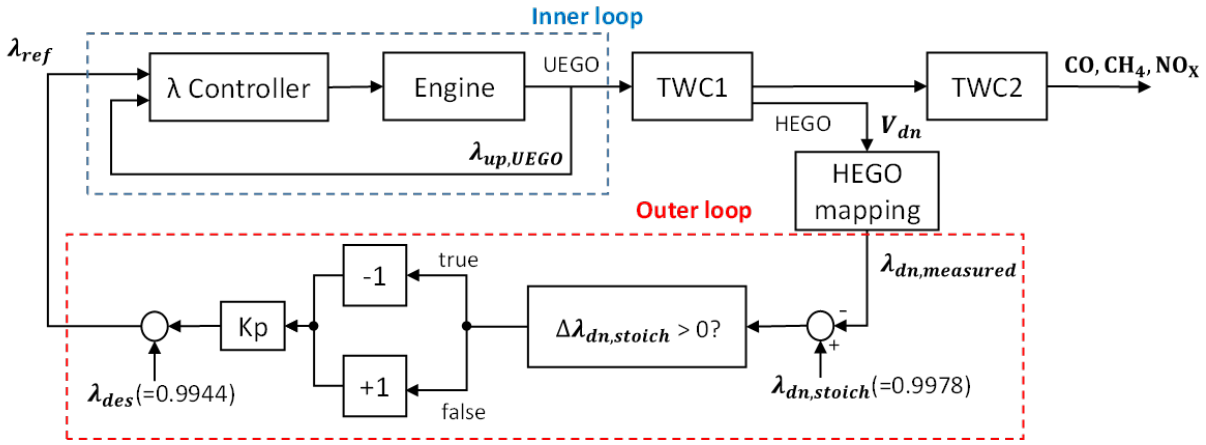


**Figure 2.8.** Control Strategy 3.

#### 2.5.4 Strategy 4: Inner AFR Control + PI Outer Loop Control with EKF

In this control strategy, the outer loop feedback control consists of a PI controller and an extended Kalman filter for FOS estimation (Fig. 2.9). The outer loop controller controls the desired  $\lambda$  command to keep the TWC1 FOS from reaching 0 and 1, which in other words, keeps the TWC1 from both over-reduction and over-oxidation. The same HEGO signal mapping method as in Strategy 3 is used in this control strategy. The engine-out exhaust air flow rate required by TWC modeling is approximated by the exhaust flow rate.

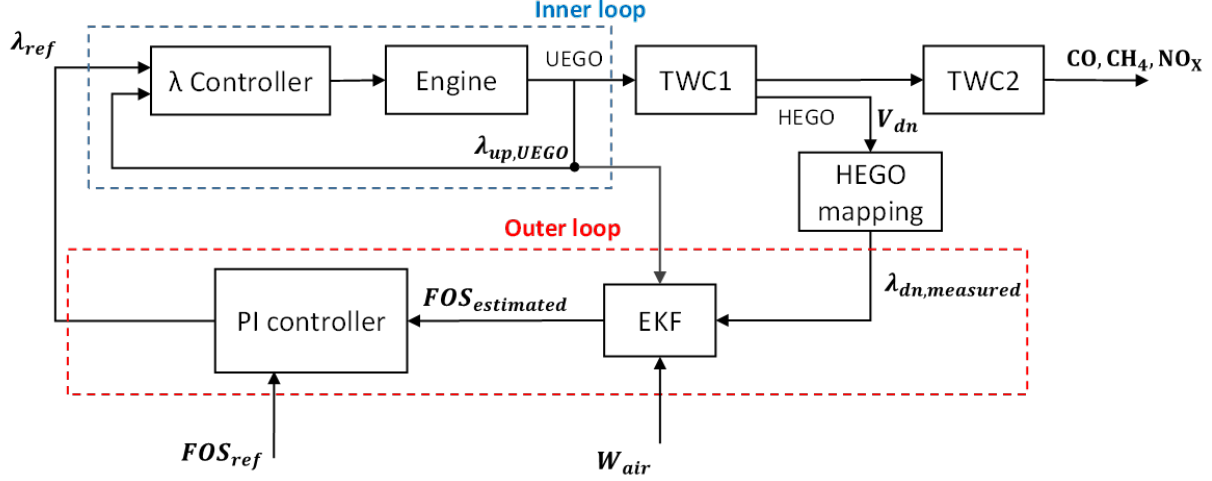


Figure 2.9. Control Strategy 4.

### 2.5.5 Strategy 5: Inner AFR Control + Robust Outer loop Control with EKF

In this control strategy, the PI controller in Strategy 4 is replaced by the robust controller developed previously. It is the proposed outer loop control strategy in the thesis, which was previously shown in Fig. 2.2.

## 2.6 Otto-FTP drive cycle

The Otto-FTP drive cycle is introduced for simulation test. The Otto-FTP drive cycle is commonly used in testing medium / heavy duty natural gas trucks in the United States. The entire procedure consists of a 20-min cold start cycle, followed by a 20-min soak period and a 20-min warm start drive cycle. The engine's reference torque and speed of the entire procedure is shown in Fig. 2.10.

As is mentioned in Chapter 1, natural gas SI engine's after-treatment system requires relatively higher temperatures than traditional SI engines such as gasoline engine to effectively react with engine-out gases, especially considering the difference in  $UHC$  composition (methane -  $CH_4$  vs. other  $HC$ ). Without new technologies for reaching lower catalytic reaction temperature point or new catalyst material for better exhaust gas consumption, the beginning half to one minute of the cold start cycle does not have sufficient temperature to



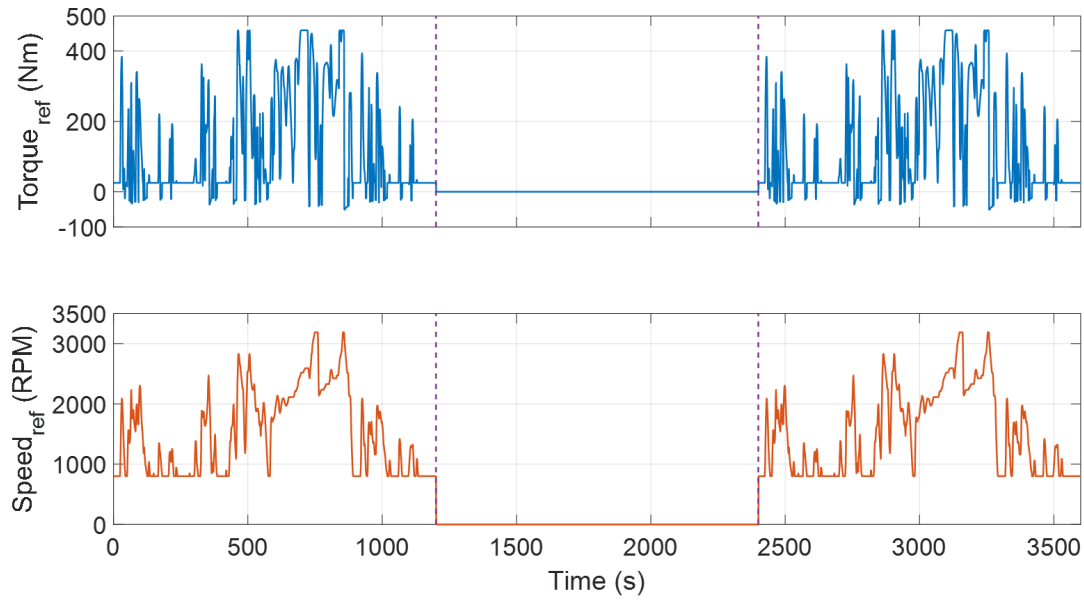


**Figure 2.10.** Engine's reference torque and speed for Otto-FTP drive cycle.

activate chemical reactions inside the TWC, no matter what outer-loop control strategy is used. It will be expanded in later sections about this phenomenon, where higher emissions are observed in cold cycle than in warm cycle. The overall emission is the sum of 1/7 of cold cycle's cumulative emission and 6/7 of warm cycle's cumulative emission.

## 2.7 Fuel cut-off

Fuel cut-off (or fuel cut) in IC engines is cutting the supply of fuel by disabling fuel injector signal from the vehicle's electronic control unit (ECU) [17]. The fuel cut-off is typically activated when vehicle decelerates or stops, since no load/ throttle is actually demanded from engine during those periods. The main purpose of including fuel cut-off is for fuel economy and potential emission reduction (especially  $CO_2$  because of the decrease in fuel combustion).

In this thesis, engines both with the fuel cut-off feature and without the feature are investigated in the simulation. It will be expanded in later sections that the results with fuel cut-off show better fuel economy than those without. However, fuel cut-off leads to higher

tail pipe emission, which also brings new research potentials that will be detailed in Chapter 4.

## 2.8 Model calibration

The parameters  $a_L$ ,  $b_L$ ,  $a_R$ ,  $b_R$ ,  $f_{sat}$ ,  $\alpha_L$ ,  $\alpha_R$ , and  $C$  are calibrated based on the high fidelity TWC Boost model in the Simulink. As mentioned previously, the Boost model is built by industrial partner based on its own test bench data to emulate the TWC dynamics, with no disclosed information on the model accuracy in comparison with real product. It's suggested by industrial partner to use the Boost model as the truth reference and virtual test bench for the model-in-loop simulation, which provides necessary measurement information for the control-oriented model, such as EGO sensors and flow rate sensors.

In the Boost model, more specifically, TWC1 and TWC2 are each divided into four equal pieces and modeled piece-wise, which provides datasets at multiple locations, including gaseous and solid temperature, the catalyst surface and subsurface oxidation state, as well as gas species densities. Since we are more focused on transient response throughout drive cycle, which we'll talk in detail in later sections, the average of catalyst's surface  $CeO_2$  mole fraction is used as the reference FOS. Since only the TWC1 is in the outer feedback loop, TWC1 is thus taken as the truth reference for the thesis dynamic model's calibration.

### Find the saturation point of the air flow rate $W_{air}$ , i.e., $f_{sat}$

Under the same  $\lambda_{up}$  profile, send in a constant and incrementally increasing air flow rate until the point where the TWC breakthrough time slows down changing until it stops. Then that air flow rate can be considered  $W_{air}$ 's saturation point. Fig. 2.11 and Fig. 2.12 are two examples of  $W_{air}$ 's effect on TWC's reaction rate under triangular (/ramp)  $\lambda_{ref}$  input and square (/step)  $\lambda_{ref}$  input respectively. For each figure, the same  $\lambda_{ref}$  is applied at three different flow rates, blue curve being the lowest rate, red curve being the intermediate rate and orange curve being the highest rate of the three. It is clear that TWC1's reaction to the same  $\lambda_{up}$  input varies significantly as air flow rate varies. The effect is shown in the different behavior of  $\lambda_{dn}$  as well. It is also observed that the  $\lambda_{dn}$  and  $FOS$  has some abnormal behavior

in ultra low flow rate. It is probably because of higher order complexity in Boost chemical model during low load condition.

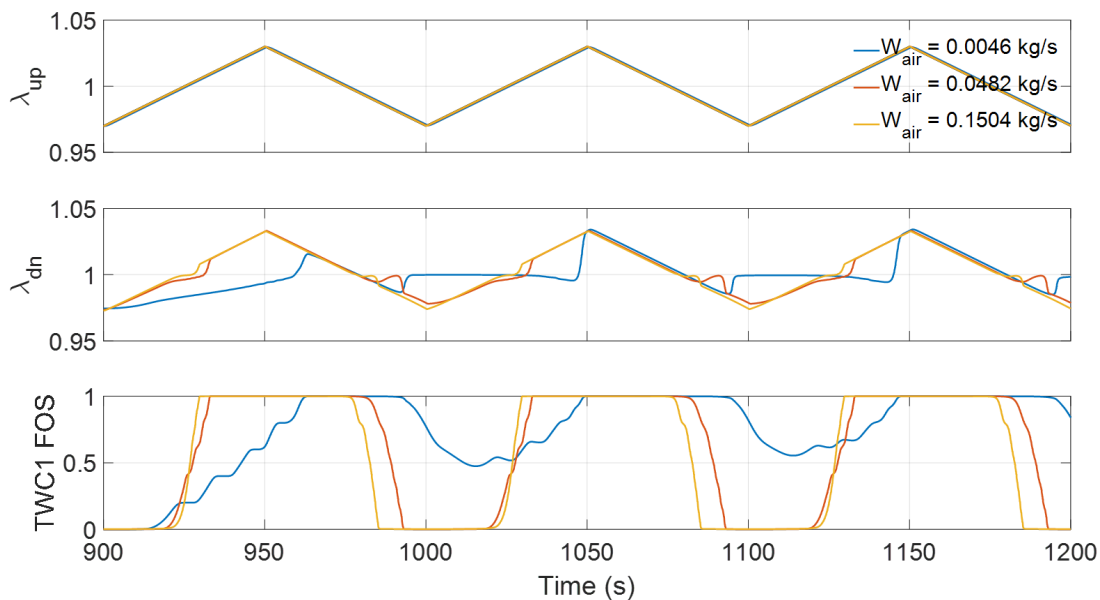


**Figure 2.11.**  $\lambda_{up}$ ,  $\lambda_{dn}$  and TWC1's  $FOS$  under different air flow rate - Triangular input.

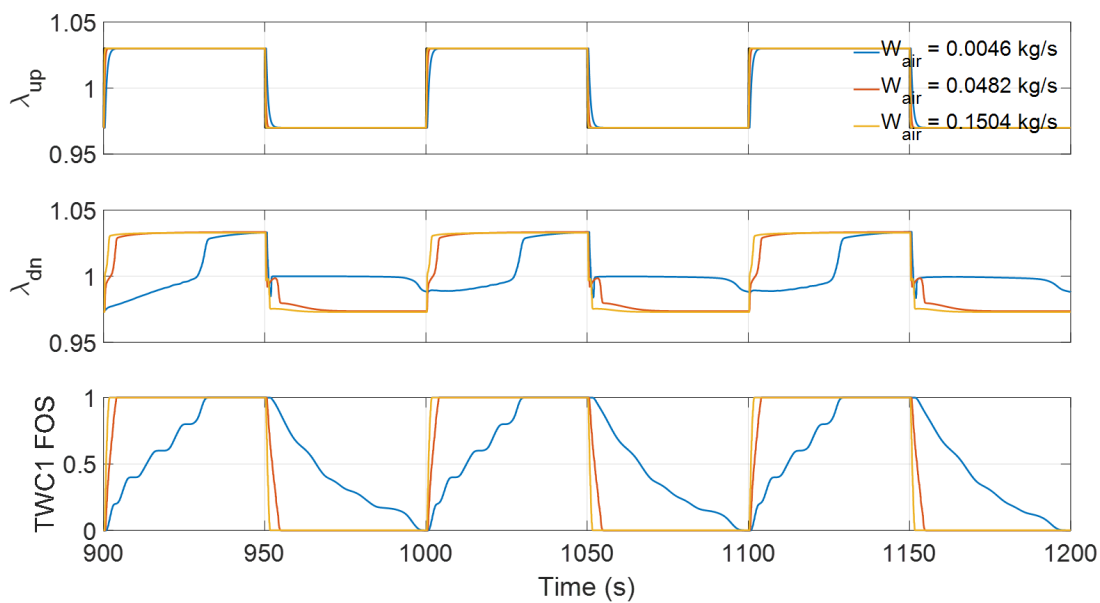


**Figure 2.12.**  $\lambda_{up}$ ,  $\lambda_{dn}$  and TWC1's  $FOS$  under different air flow rate - Square input.

The NG engine in our simulink model actually comes with hardware limits on the achievable Torque and Speed, which are [800Nm, 3500Nm] and [0rpm, 450rpm], respectively. Therefore, instead of slowly finding the saturation point by increasing  $W_{air}$ , we first check whether the maximum achievable work load being [3500Nm 450rpm] is within the saturation range. [3500Nm 450rpm] generates an air flow rate of  $W_{air} = 0.1504 \text{ kg/s}$ , then two slightly smaller  $W_{air}$ -s are compared in Fig. 2.13. In the left plots  $\lambda_{up}$  rises from rich to lean, and TWC1 turns from fully reduced to fully oxidized, while in the right plots  $\lambda_{up}$  drops from lean to rich, and TWC1 turns from fully oxidized to fully reduced. It is observed that TWC1's reaction rate still increases as  $W_{air}$  increases. So, the saturation point is beyond the range of the air flow rate in the test, which means  $f_{sat}$  is not an issue in this test.

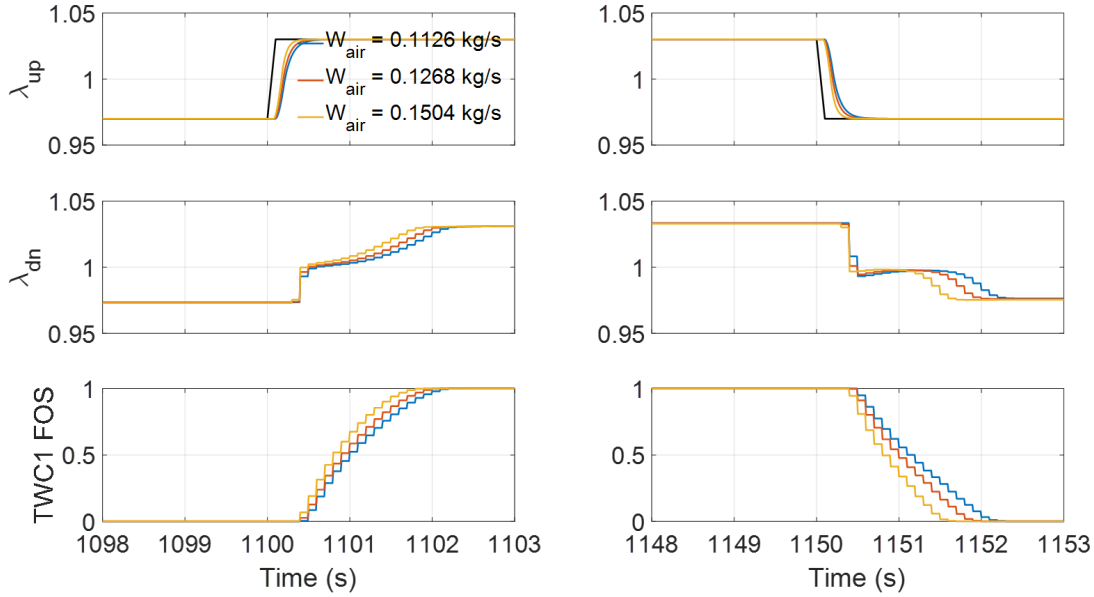


**Figure 2.13.**  $\lambda_{up}$ ,  $\lambda_{dn}$  and TWC1's  $FOS$  under extremely high work loads - Square input.

**Find the effective TWC1 oxygen capacity, i.e.,  $C$**

From (1.2) and (1.4), the effective TWC1 oxygen capacity is estimated by calculating the  $O_2$  mass difference between the TWC upstream and downstream exhaust gas.

$$C = \frac{M_{O_2}}{M_{exh}} \int_{t_1}^{t_2} W_{exh} (C_{O_2,in} - C_{O_2,out}) \quad (2.35)$$

Two work loads are analyzed for  $C$  estimation. An exhaust flow rate of  $W_{air} = 0.0482kg/s$  is applied in Fig. 2.14a, and an exhaust flow rate of  $W_{air} = 0.1504kg/s$  is applied in Fig. 2.14b. In each figure, the blue curve is  $FOS$  during rich to lean transition, the red solid curve is TWC1's inlet  $O_2$  in ppm (parts-per million) and the red dotted curve is TWC1's outlet  $O_2$  in ppm. As was mentioned in the beginning of this section, the truth reference  $FOS$  is based on the average of catalyst's surface  $CeO_2$  mole fraction because the comparison work uses a transient drive cycle. The oxygen change outside of purple dashed lines are not due to catalyst's surface oxidation and are thus not considered. The estimated value of  $C$  from both figures are  $0.4648e-3kg$  and  $0.4254e-3kg$  respectively. It is noted that the estimation of  $C$  here is not very precise because other species in the exhaust gas also contribute to the  $FOS$  change, but it offers a rough estimate to start with, especially when incorporating EKF in later work.

**Find  $a_L$ ,  $b_L$ ,  $a_R$ ,  $b_R$ ,  $\alpha_L$ , and  $\alpha_R$**

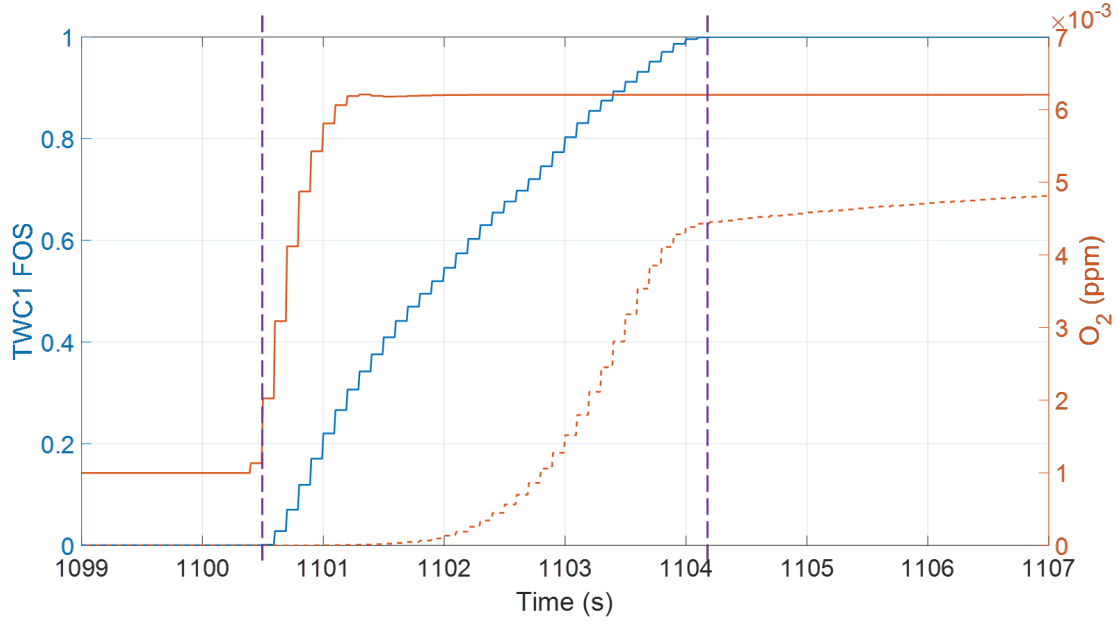
The least-square fitting method is used to minimize the  $\rho$  error for both lean and rich conditions. The reference  $\rho$  value is calculated by the measured TWC1 upstream  $\lambda$  and downstream  $\lambda$  based on (2.5), i.e.,  $\rho = \frac{\lambda_{up}-\lambda_{dn}}{\lambda_{up}-1}$ . The optimization problem is then expressed as follows and solved by using MATLAB function “*lsqcurvefit*”.

$$\begin{cases} \min_{\alpha_L, a_L, b_L} \sum (\rho_{model} - \rho_{meas})^2 & \lambda_{up, meas} > 1 \\ \min_{\alpha_R, a_R, b_R} \sum (\rho_{model} - \rho_{meas})^2 & \lambda_{up, meas} < 1 \end{cases} \quad (2.36)$$

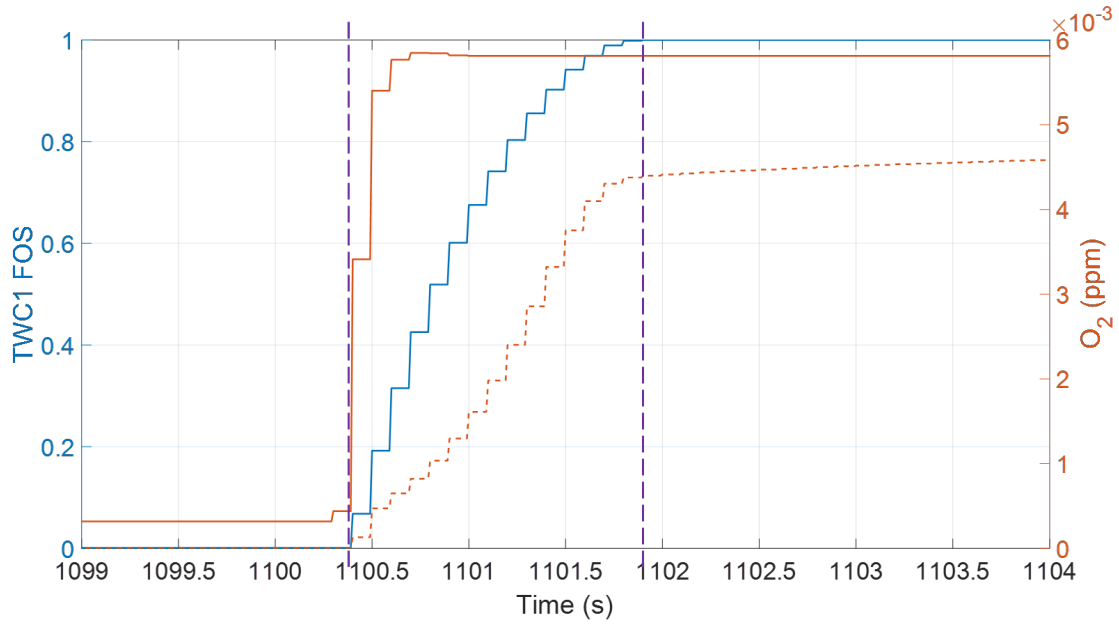
By substituting  $\rho_{model}$  from (2.2) and  $\rho_{meas}$  from (2.5), (2.36) turns into:

$$\begin{cases} \min_{\alpha_L, a_L, b_L} \sum \left( \alpha_L \times \left( \frac{e^{(a_L \times FOS^2 + b_L \times FOS)} - e^{(a_L + b_L)}}{e^{(a_L + b_L)} - 1} \right) - \frac{\lambda_{up, meas} - \lambda_{dn, meas}}{\lambda_{up, meas} - 1} \right)^2 & \lambda_{up, measured} > 1 \\ \min_{\alpha_R, a_R, b_R} \sum \left( \alpha_R \times \left( \frac{e^{(a_R \times FOS^2 + b_R \times FOS)} - 1}{e^{(a_R + b_R)} - 1} \right) - \frac{\lambda_{up, meas} - \lambda_{dn, meas}}{\lambda_{up, meas} - 1} \right)^2 & \lambda_{up, measured} < 1 \end{cases} \quad (2.37)$$

$a_R$  and  $b_R$  are fitted at 13.45 and -20.63.  $a_L$  and  $b_L$  are fitted at 2.55 and 1.2. During calibration, it is observed that the Boost model was built on neutral  $\lambda_{up}$  and mid-bed  $\lambda_{dn}$



(a)  $W_{air} = 0.0482kg/s$



(b)  $W_{air} = 0.01504kg/s$

**Figure 2.14.** TWC1's  $FOS$  and  $O_2$  before and after TWC1 - Square input.

(values at which the  $\lambda$ s cross rich & lean and the engine consumes fuel most efficiently) slightly different from 1 (typical stoichiometry point). After some trials using EKF for different  $\lambda$  set, the neutral point of  $\lambda_{up}$  and  $\lambda_{dn}$  are set at 0.9944 and 0.9978 respectively.  $\alpha_L$ ,  $\alpha_R$  and  $C$  are updated to 1.06, 0.91 and  $1/1.18e3kg$ .

## 2.9 Sensor measurements, FOS status and their effect on instantaneous emission

In this section, simulation results of all five control strategies will be presented and analyzed in terms of the sensor-measured variable updates including  $\lambda_{up}$ , mid-bed  $\lambda_{dn}$  and mass air flow rate  $W_{air}$ . To further differentiate the differences in working mechanism between  $\lambda_{dn}$  feedback based controllers and FOS feedback based controllers, the FOS update is also discussed in this section. Instantaneous emission results for exhaust gases  $CO$ ,  $CH_4$  and  $NO_x$  are also presented and analyzed for controller performance.

This section will be divided into three different aspects. First is to analyze and compare warm start drive cycle's results of all five control strategies for engine with fuel cut-off; the purpose of this subsection is to compare the controller performance when the TWC is warmed up and doesn't impede control performance during the cycle. Secondly, a comparison of engines with vs. without fuel cut-off will be shown for selected control cases, to demonstrate TWC's over-oxidation issue coming from fuel cut-offs. Thirdly, a comparison between cold start cycle and hot start cycle is shown for demonstration of temperature's effect on the controller performance.

### 2.9.1 Controllers' performances for engine with fuel cut-off, during warm cycle

In this part, sensor-measured variables  $\lambda_{up}$ ,  $\lambda_{dn}$  and  $W_{air}$  as well as oxidation level FOS will be discussed and compared amongst control strategies, for the warm start drive cycle.

#### Strategy 1: Constant $\lambda_{ref}$ Control

Fig. 2.15 shows Strategy 1's variable updates, Fig. 2.16 shows the FOS updates for both inside TWC1 and TWC2, and Fig. 2.17 shows the instantaneous emission of  $CO$ ,  $CH_4$  and  $NO_x$  in unit of ppm (parts per million). As is mentioned previously, Strategy 1 serves as a baseline to illustrate the necessity of outer-loop controller in general. So the results in Strategy 1 will be frequently brought about later when analyzing other control strategies (which all include outer-loop controllers in contrast).

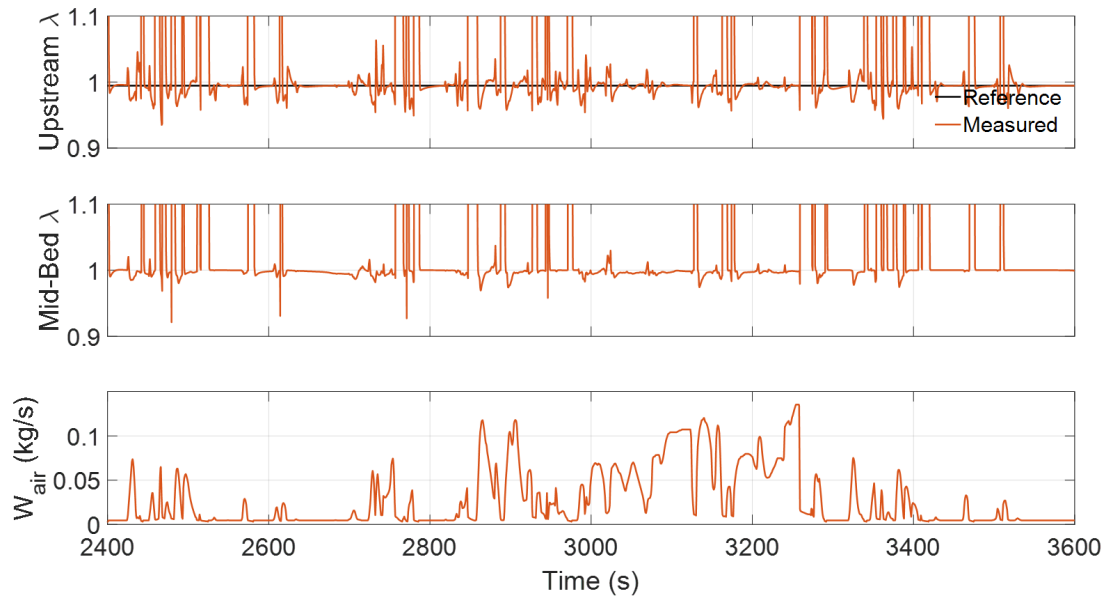


**Figure 2.15.** Sensor measurements for Strategy 1 - Warm cycle.

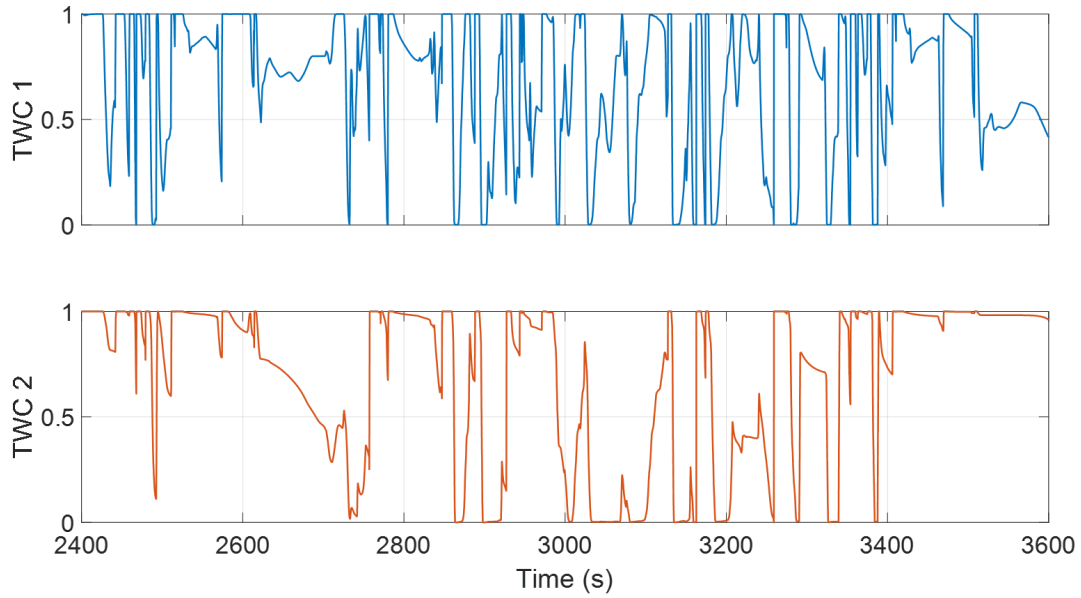


**Figure 2.16.** TWC1's & TWC2's FOS for Strategy 1 - Warm cycle.

In Fig. 2.15, the upper plot includes reference  $\lambda_{up}$  in black and measured  $\lambda_{up}$  in red; the middle plot shows the measured mid-bed  $\lambda_{dn}$  in red; while the lower plot shows the measured mass air flow rate  $W_{air}$  in red. It's observed that although the reference  $\lambda_{up}$  has been constant



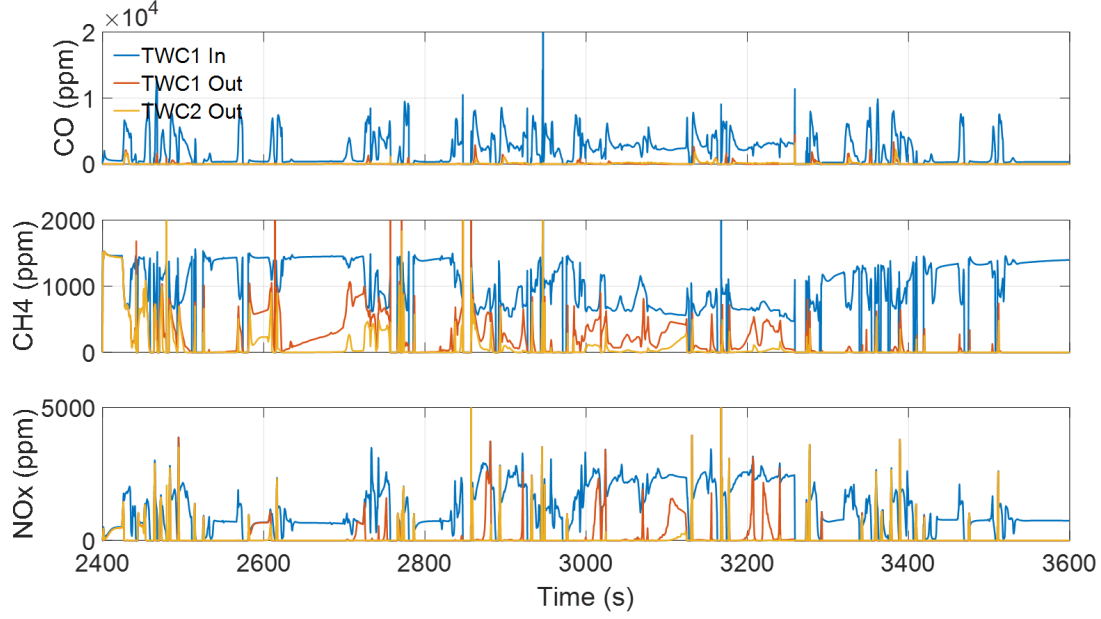


**Figure 2.17.** Instantaneous emissions for Strategy 1 - Warm cycle.

(at 0.9944) throughout the drive cycle for Strategy 1, the measured  $\lambda_{up}$  still fluctuates with time. It is due to the changes in engine's working condition, namely the desired torque and speed in Fig. 2.10.  $W_{air}$  is also directly influenced by the working condition, being highest (up to  $\sim 0.15kg/s$ ) when both torque and speed are high, and lowest (down to  $\sim 0.01kg/s$ ) when both torque and speed are low.

In Fig. 2.16, the upper plot shows TWC1's FOS and the lower plot shows TWC2's FOS. Both FOSs change with time as  $\lambda_{up}$ , engine speed and torque changes throughout drive cycle. It is worth noting that only TWC1 sits in outer feedback loop for those control strategies with outer loop controller, while TWC2 serves as complementary catalyst to react with excessive exhaust gases that TWC1 have not reacted with. However, the dynamics inside TWC2 is still worth looking at since it is correlated with the tail pipe emissions.

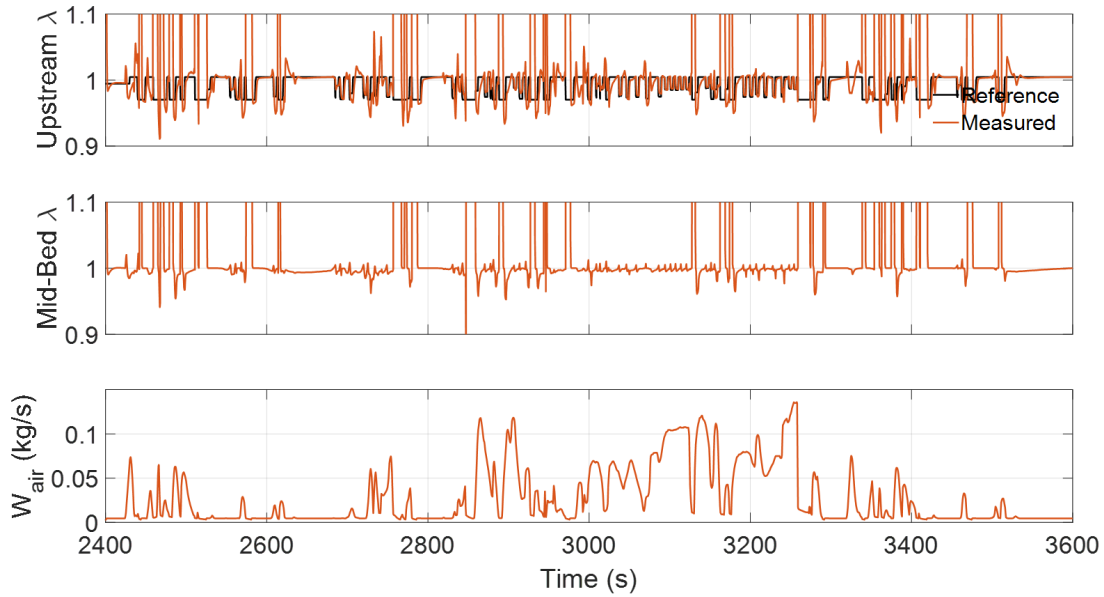
In Fig. 2.17, the emission data of  $CO$ ,  $CH_4$  and  $NO_x$  are shown from top to bottom, respectively. In each subplot, the blue curve represents density of the corresponding species before entering TWC1 (i.e., entering TWC); the red curve represents its density after exiting TWC1 (also entering TWC2), which is also the direct emission output from outer loop

controller; the orange curve represents its density exiting TWC2 (i.e., exiting TWC), which is the final emission out of tail pipe.

When TWC1's and TWC2's FOSs both stay at 0 or 1 for a period of time, it is possible that the catalyst is fully reduced or oxidized, which leaves catalyst least effective in reacting with certain species in the exhaust gas. For example, in Fig. 2.16, both TWC1 and TWC2 are fully oxidized for a while after 2400s, so the tail pipe  $CH_4$  and  $NO_x$  are not effectively reduced.

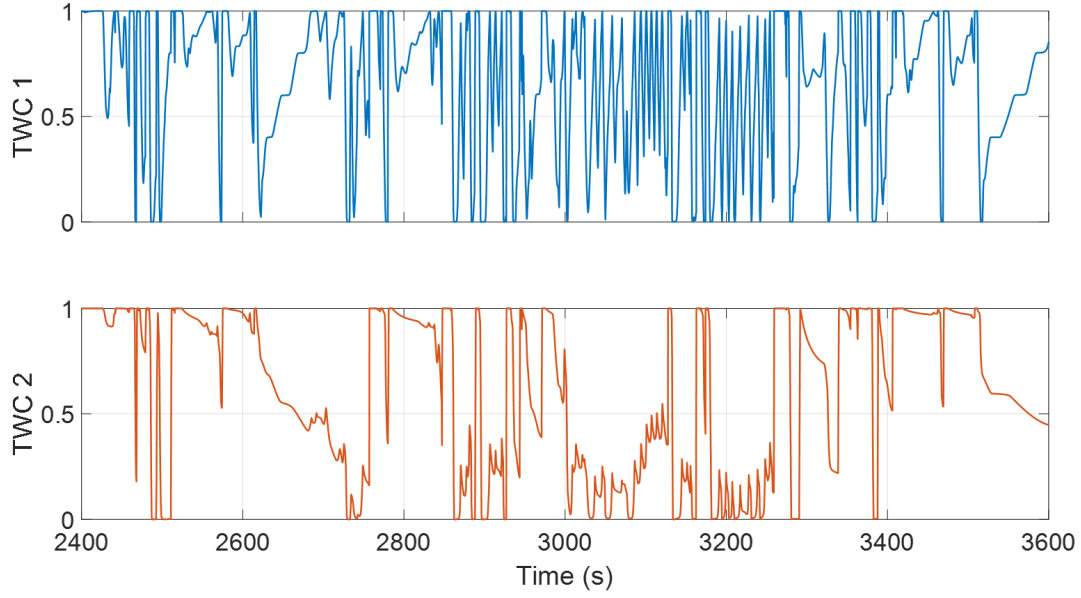
### Strategy 2: Inner Loop AFR Control + Baseline Outer Loop Control

Fig. 2.18 shows Strategy 2's variable updates, Fig. 2.19 shows the FOS updates for both TWC1 and TWC2, and Fig. 2.20 shows the instantaneous emissions of  $CO$ ,  $CH_4$  and  $NO_x$ . Strategy 2 serves as a baseline to compare with other outer loop controllers, especially the FOS-based controllers in the thesis.



**Figure 2.18.** Sensor measurements for Strategy 2 - Warm cycle, with fuel cut.

Strategy 2's plots are compared with Strategy 1's plots to demonstrate how the outer loop controller takes effect. First noticeable change is the difference in reference  $\lambda_{up}$  between Fig. 2.15 and Fig. 2.18. The baseline outer loop controller gives time-variant reference  $\lambda_{up}$



**Figure 2.19.** TWC1's & TWC2's FOS for Strategy 2 - Warm cycle, with fuel cut.

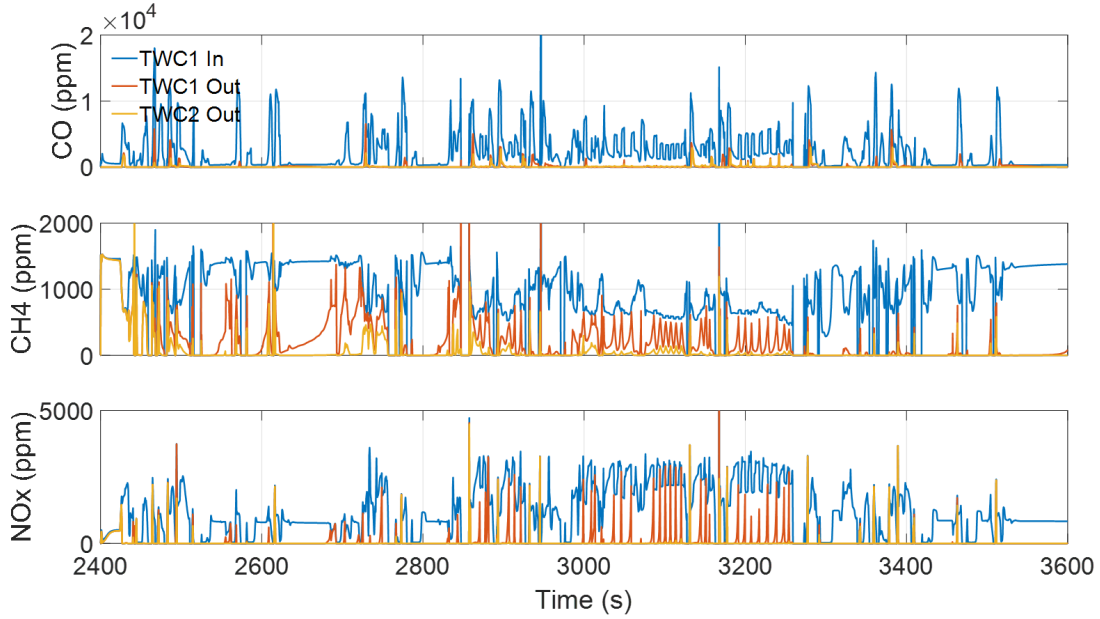


**Figure 2.20.** Instantaneous emissions for Strategy 2 - Warm cycle, with fuel cut.

command based on feedback of  $\lambda_{dn}$ ,  $W_{air}$  and  $T_{dn}$ . The purpose of outer loop feedback is to use measured signals to make corrections to input command. Through outer loop feedback, the net average  $\lambda$  stays closer to  $\lambda$  window and thus renders a more efficient exhaust gas

reaction. In comparing Fig. 2.16 with Fig. 2.19, Strategy 2's TWC1 FOS is less likely to stay at boundaries 0 and 1 than Strategy 1 because of outer loop feedback, which helps emission reduction which is more clear in the zoomed-plot comparison between Fig. 2.21 and Fig. 2.22. Fig. 2.21 and Fig. 2.22 each presents the updates of  $\lambda_{up}$ , FOS,  $CO$ ,  $CH_4$  and  $NO_x$  in Strategy 1 and Strategy 2 respectively, during 3000s  $\sim$  3200s.

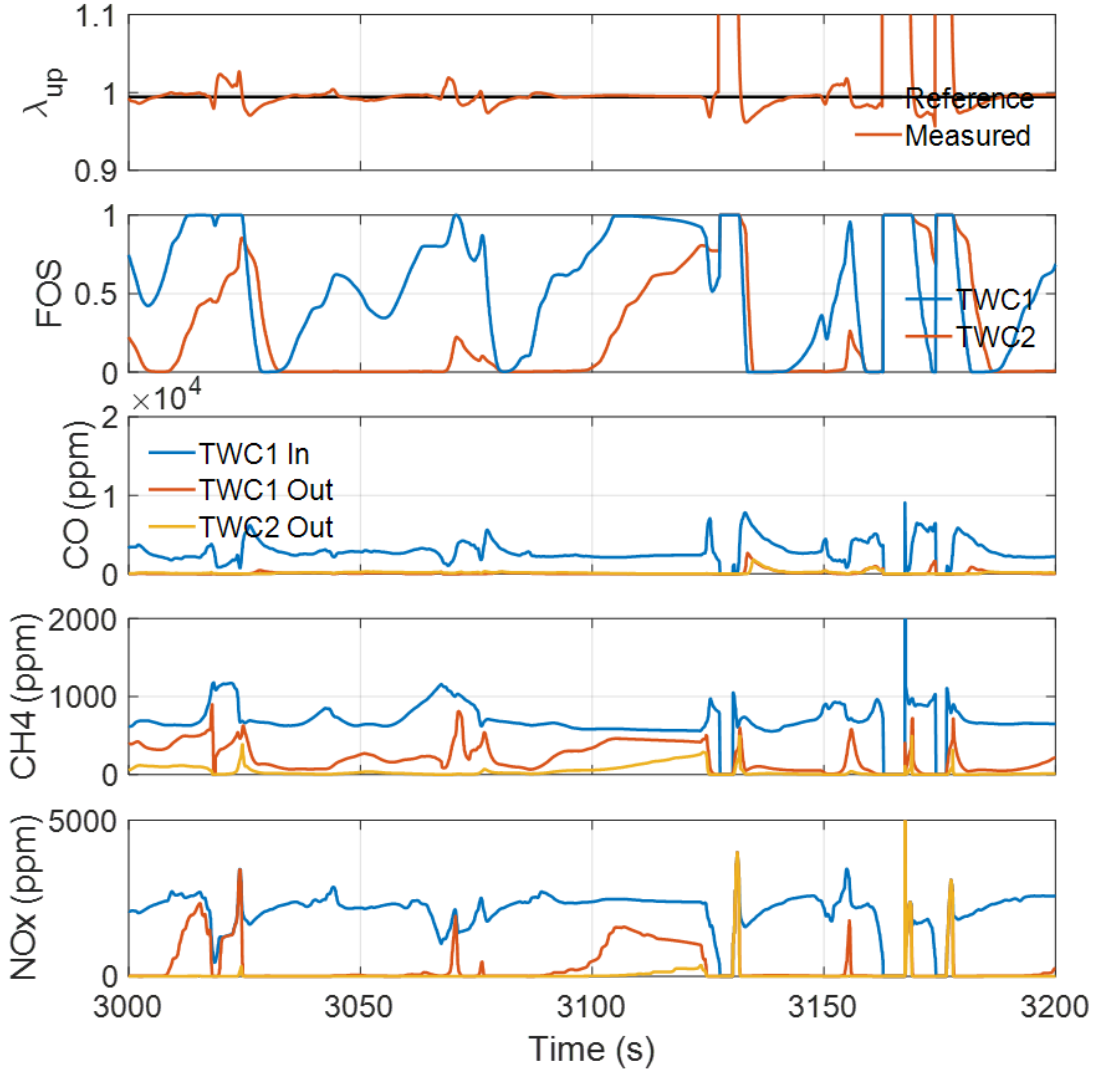


**Figure 2.21.** Strategy 1 - 3000s  $\sim$  3200s, Warm cycle, with fuel cut.

The high peaks in actual  $\lambda_{up}$  (surpassing 1.1) are those during fuel cut-offs, where there is theoretically only pure air flowing through, resulting in an extremely lean exhaust gas. The main side effect of fuel cut-offs, which will also be explained in more details in later section,

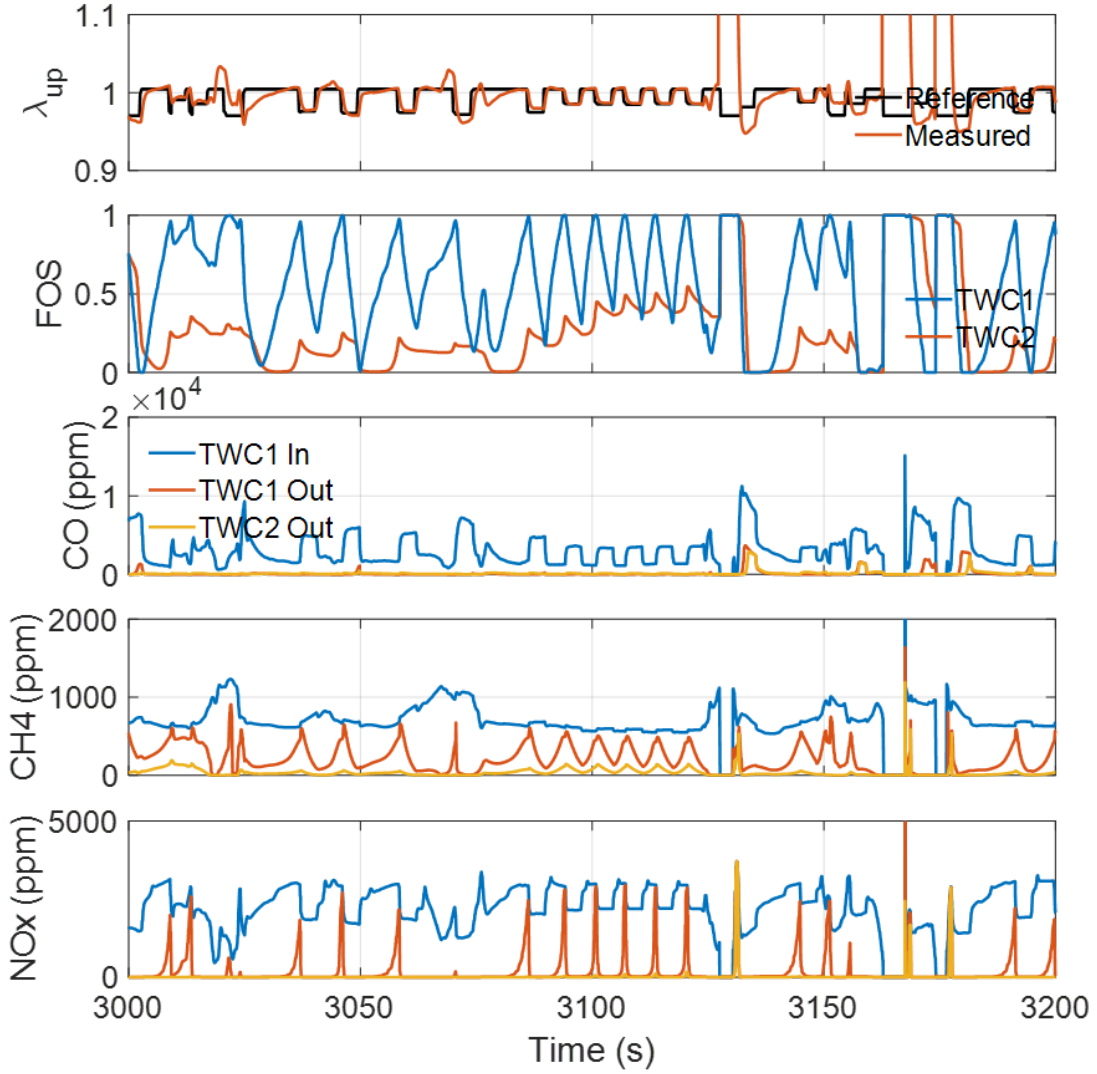


**Figure 2.22.** Strategy 2 - 3000s ~3200s, Warm cycle, with fuel cut.

is that the TWC is easy to be over-oxidized during those fuel cut-off events. It is also shown in the FOS subplot where both TWC1's and TWC2's FOSes reach and stay at 1. This side effect can not be solved by outer loop feedback controllers and need other technologies for mitigation.

With the TWC at high FOS (=1) after each fuel cut-off event, all outer loop controllers generate rich reference  $\lambda_{up}$  command which helps TWC reduce faster, as shown at 3130s and 3170s. Additionally, the fluctuations in FOS help eliminate the tail pipe  $NO_x$  hump at around 3120s. It will be shown in later section that outer loop controllers really make

significant improvement on  $NO_x$  emissions and noticeable improvement on  $CH_4$  emissions. Slightly higher  $CO$  emissions than Strategy 1 are observed but it makes sense since  $CO$  is more in favor of lean conditions (especially with fuel cut-off).

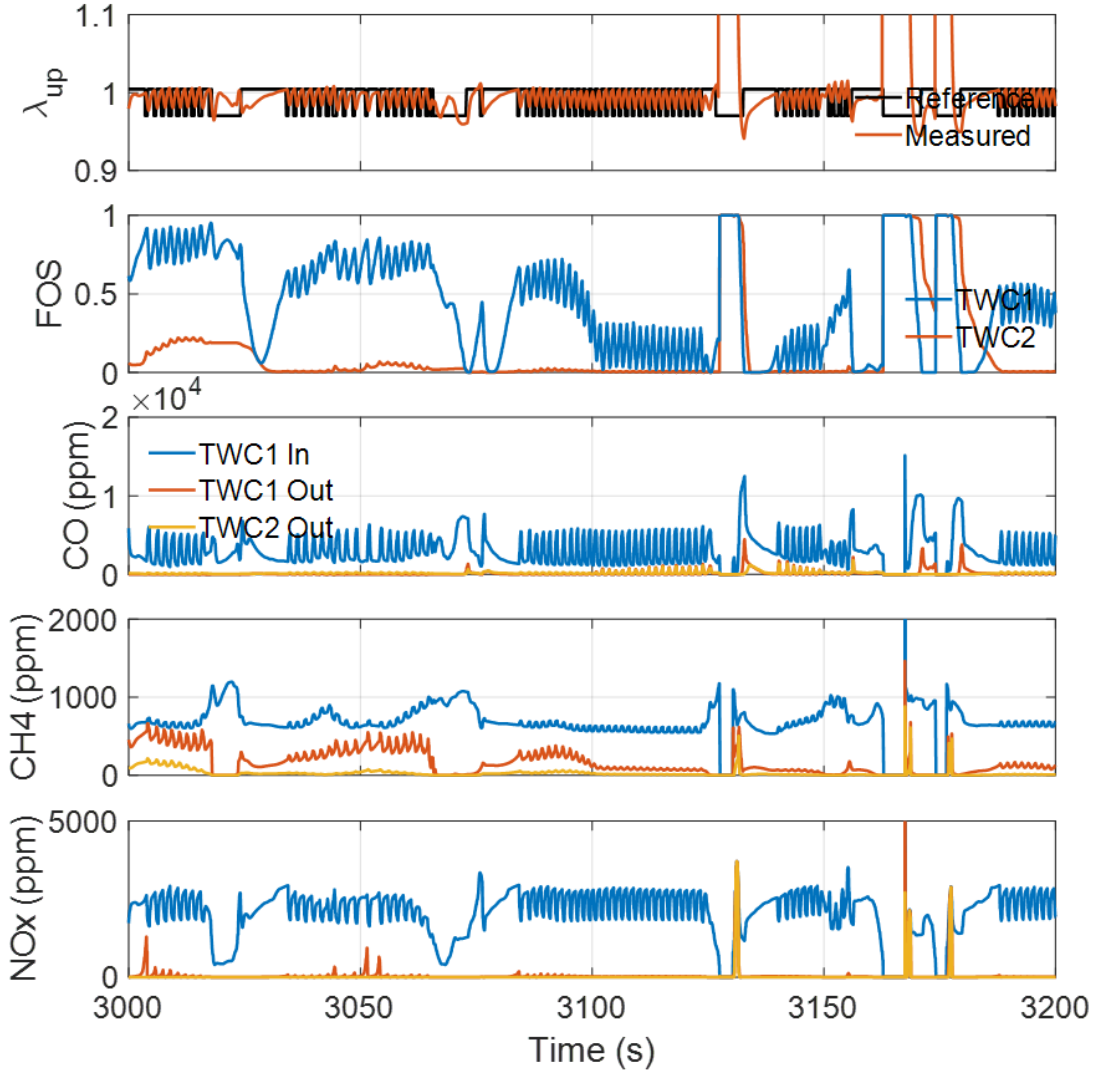
### Strategy 3: Inner Loop AFR Control + Binary Outer Loop Control

Fig. 2.23 shows zoomed plot of Strategy 3's  $\lambda_{up}$ , FOS,  $CO$ ,  $CH_4$  and  $NO_x$  during the same period (3000s  $\sim$  3200s). Strategy 3 only gives switching rich/lean reference  $\lambda_{up}$  command by comparing feedback  $\lambda_{dn}$  with its set point (0.9978). It is a simpler control strategy than baseline Strategy 2 and is easy to implement. It is tested to compare with more advanced outer loop controllers and to observe their differences.

In comparing Fig. 2.23 with Fig. 2.22. Strategy 3's reference  $\lambda_{up}$  command differs from Strategy 2's command in a way that the reference command here is very sensitive to measured  $\lambda_{dn}$  and is thus easy to fluctuate up and down repeatedly. It is unknown if it will bring material fatigue to engine faster since the engine always works with its hardware limit despite the input command, but in the performance viewpoint, Strategy 3 manages to keep FOS less from boundaries 0 and 1 than Strategy 1 (Fig. 2.21), which similar to Strategy 2, leads to smaller  $CH_4$  and  $NO_x$  emissions.

### Strategy 4: Inner AFR Control + PI Outer Loop Control with EKF

Fig. 2.24 shows zoomed plot of Strategy 4's  $\lambda_{up}$ , FOS,  $CO$ ,  $CH_4$  and  $NO_x$  during the same period (3000s  $\sim$  3200s). Strategy 4 estimates TWC1's FOS with EKF based on sensor measurements and then gives reference  $\lambda_{up}$  command by comparing estimated FOS with its set point (0.4). Theoretically, Strategy 4 and 5 are different outer loop control strategies from Strategy 2 and 3 because they are using different control target (FOS vs.  $\lambda_{dn}$ ), despite that they use the same sensor information. FOS-based strategies keep the TWC1's oxidation state FOS around the set point, leaving the TWC space for either extra reduction or extra oxidation. It is justified when comparing Fig. 2.24 with Fig. 2.22, that Strategy 4's TWC1 FOS is kept within middle range instead of fluctuating up and down like Strategy 2.



**Figure 2.23.** Strategy 3 - 3000s ~3200s, Warm cycle, with fuel cut.

### Strategy 5: Inner AFR Control + Robust Outer loop Control with EKF

Fig. 2.24 shows zoomed plot of Strategy 5's  $\lambda_{up}$ , FOS,  $CO$ ,  $CH_4$  and  $NO_x$  during the same period (3000s ~ 3200s). The main difference between Strategy 4 and 5 is the choice of controller. Strategy 5, which is the MISO controller developed in the thesis, takes more system dynamics into consideration, and should show more robustness to system disturbances. In comparing Fig. 2.25 with Fig. 2.24, both strategies manage to keep FOS in the middle range. Strategy 5 exploits more potential of TWC1 in a way that, its TWC2 has not been

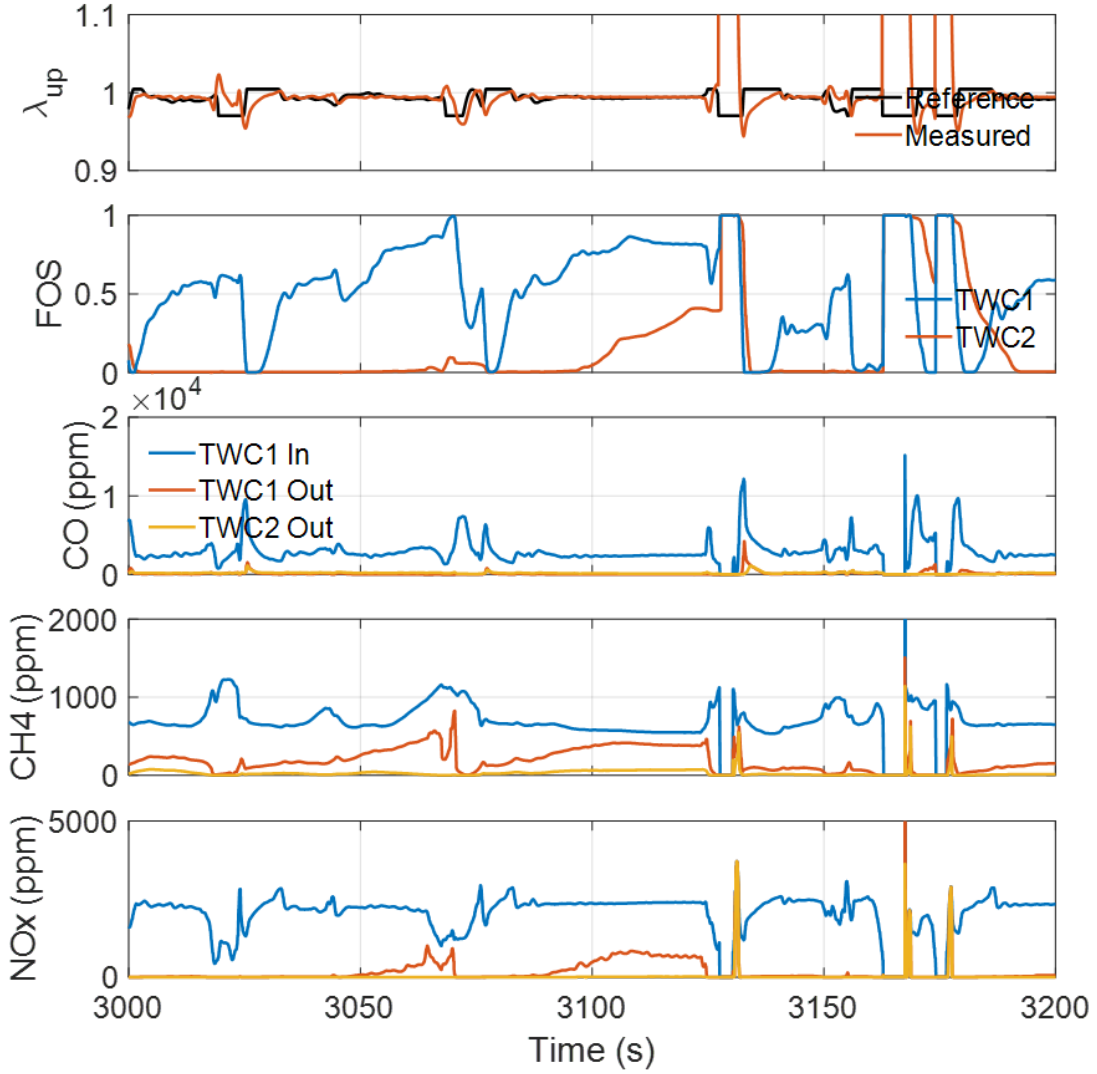


**Figure 2.24.** Strategy 4 - 3000s ~3200s, Warm cycle, with fuel cut.

used as much as when Strategy 4 is implemented. It also shows difference from Strategy 4 in TWC1's outlet  $CH_4$  and  $NO_x$  emissions, where Strategy 5 reduces almost all of  $NO_x$  in TWC1 and reduces more  $CH_4$  than Strategy 4 in TWC1.

### 2.9.2 Comparison of engine with vs. without fuel cut-off, Warm cycle

In this section, the difference between including fuel cut-off and not including fuel cut-off is discussed. Only results of Strategy 1 and Strategy 5 will be presented for the sake of



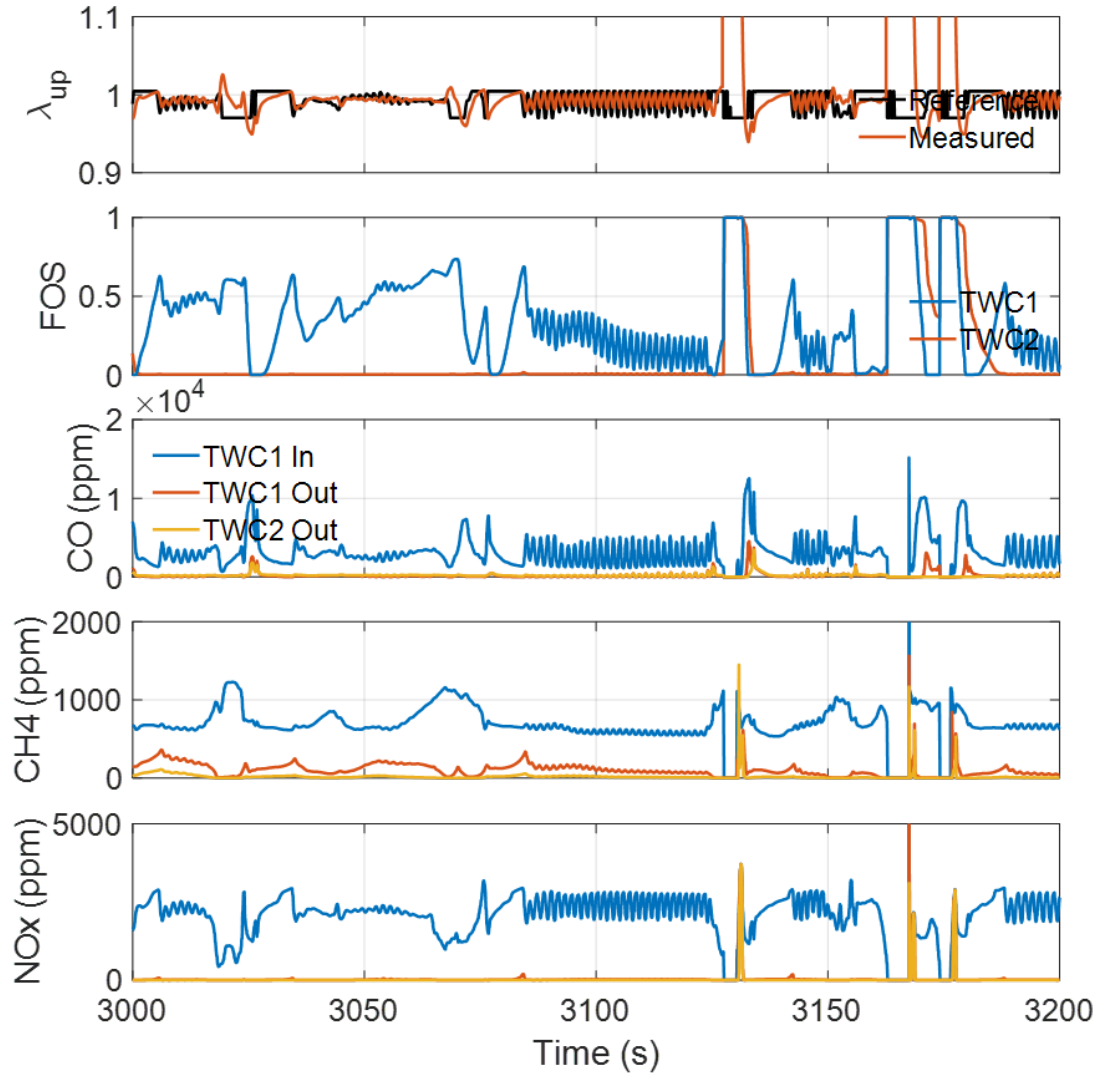


**Figure 2.25.** Strategy 5 - 3000s ~3200s, Warm cycle, with fuel cut.

demonstrating fuel cut-off's effect either with or without outer loop controller. To ease the comparison, the same zoomed time period as last section is chosen, which is 3000s ~ 3200s.

### Strategy 1

Fig. 2.26 shows zoomed plot of Strategy 1's  $\lambda_{up}$ , FOS,  $CO$ ,  $CH_4$  and  $NO_x$  for engine without fuel cut-offs. Since there doesn't involve outer loop feedback in Strategy 1, any difference that is shown in this comparison is due to the difference in engine's characteristics.

Between Fig. 2.26 and Fig. 2.21, the first observation is the difference in measured  $\lambda_{up}$ 's profile. As is briefly mentioned in the last section, engine  $\lambda$  will be infinitely high (lean) if it is during fuel cut-off event. However, it is not the case with engine without fuel cut-off, where measured  $\lambda_{up}$  keeps within relatively small range around stoichiometry. Such difference in  $\lambda_{up}$  leads to totally different TWC response during and right after those periods where fuel cut-offs are supposed to happen. FOS for engines without fuel cut-offs is much less likely to remain at 1 (i.e., TWC fully oxidized), which is favorable for a low  $NO_x$  emission outcome.

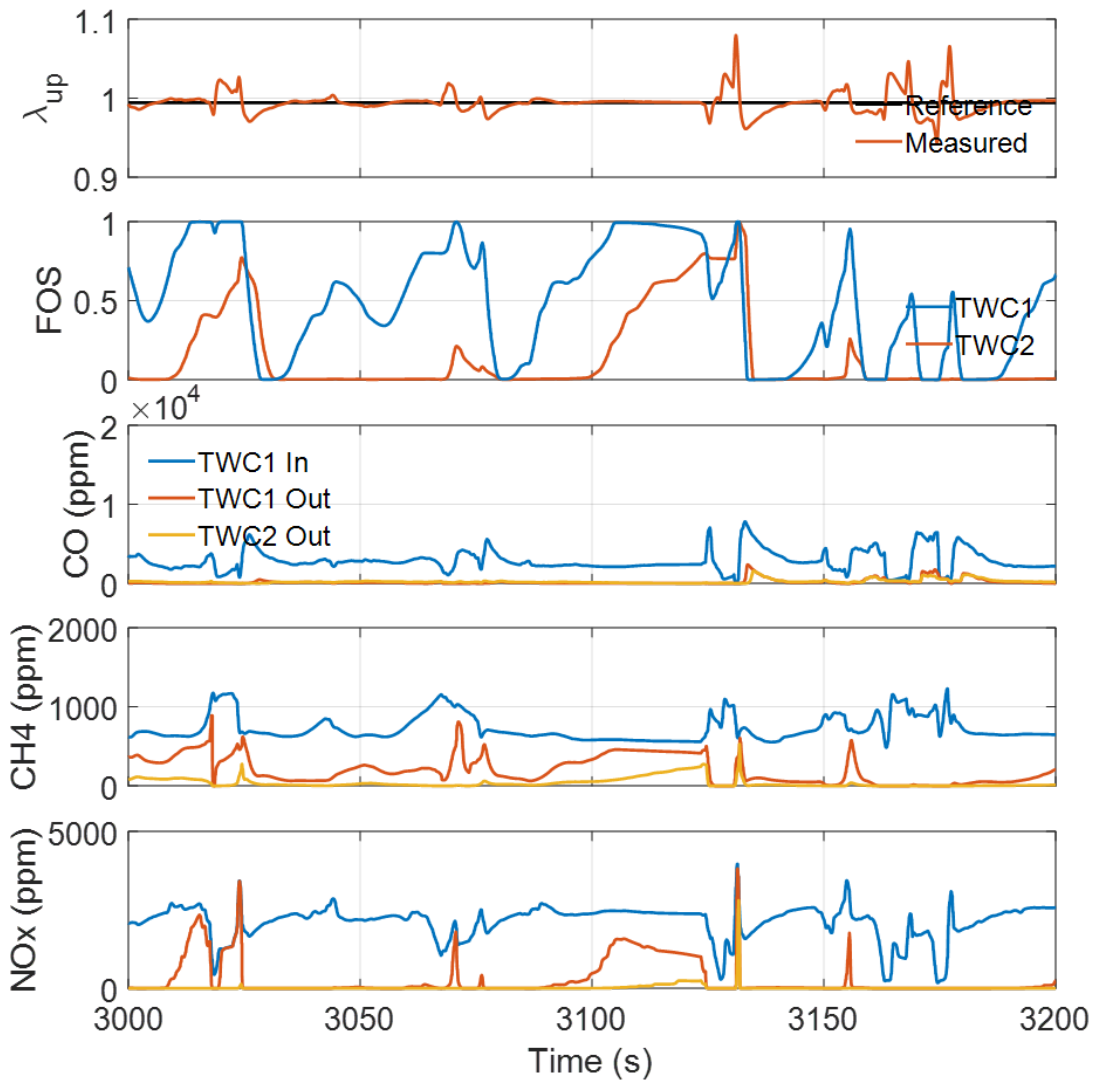


**Figure 2.26.** Strategy 1 - 3000s ~3200s, Warm cycle, without fuel cut.

## Strategy 5

Fig. 2.26 shows zoomed plot of Strategy 5's  $\lambda_{up}$ , FOS,  $CO$ ,  $CH_4$  and  $NO_x$  for engine without fuel cut-offs. Not only does it show the difference in this novel strategy's performance between having fuel cut-off or not, but also it serves to demonstrate the limitation of only improving outer-loop controller for the entire emission reduction of vehicle system.

In Fig. 2.26, when no fuel cut-off exists, Strategy 5 handles most of  $NO_x$ 's reduction with ease. However, for engine with fuel cut-off, whenever after fuel cut-off is introduced, although the outer loop controller intends to give the richest input command to compensate for the ultimate lean condition, there is still an unignorable period of time during which TWC's FOS turns back to a point where the catalyst can reduce  $NO_x$ .

## Fuel consumption and $CO_2$ emission

Although fuel cut-off introduce noticeable issue in tail pipe  $NO_x$  emission, it is still adopted in modern engines for the benefit of engine protection and fuel economy. Fuel cut-off avoids engine from load damage when no load/ throttle is needed and also saves fuel for cutting fuel injection during such periods. Fig. 2.28 shows the total fuel consumption during warm drive cycle, both using fuel cut-off and not using fuel cut-off. The difference in using different control strategies is much smaller than the difference in whether or not implementing fuel cut-off. Engine with fuel cut-off generally renders around 2% fuel savings.

Fig. ?? shows the total  $CO_2$  emission during warm drive cycle, both using fuel cut-off and not using fuel cut-off. The difference in using different control strategies is much smaller than the difference in whether or not implementing fuel cut-off. Engine with fuel cut-off generally renders around 1.8%  $CO_2$  emission reduction. Therefore, from environmental and consumer financial aspect, fuel cut-off is favored. To enjoy the benefit from fuel cut, researches on advanced technologies of preventing or slowing down the TWC oxidation during fuel cut-off events are in need, which will be shown in chapter 4.

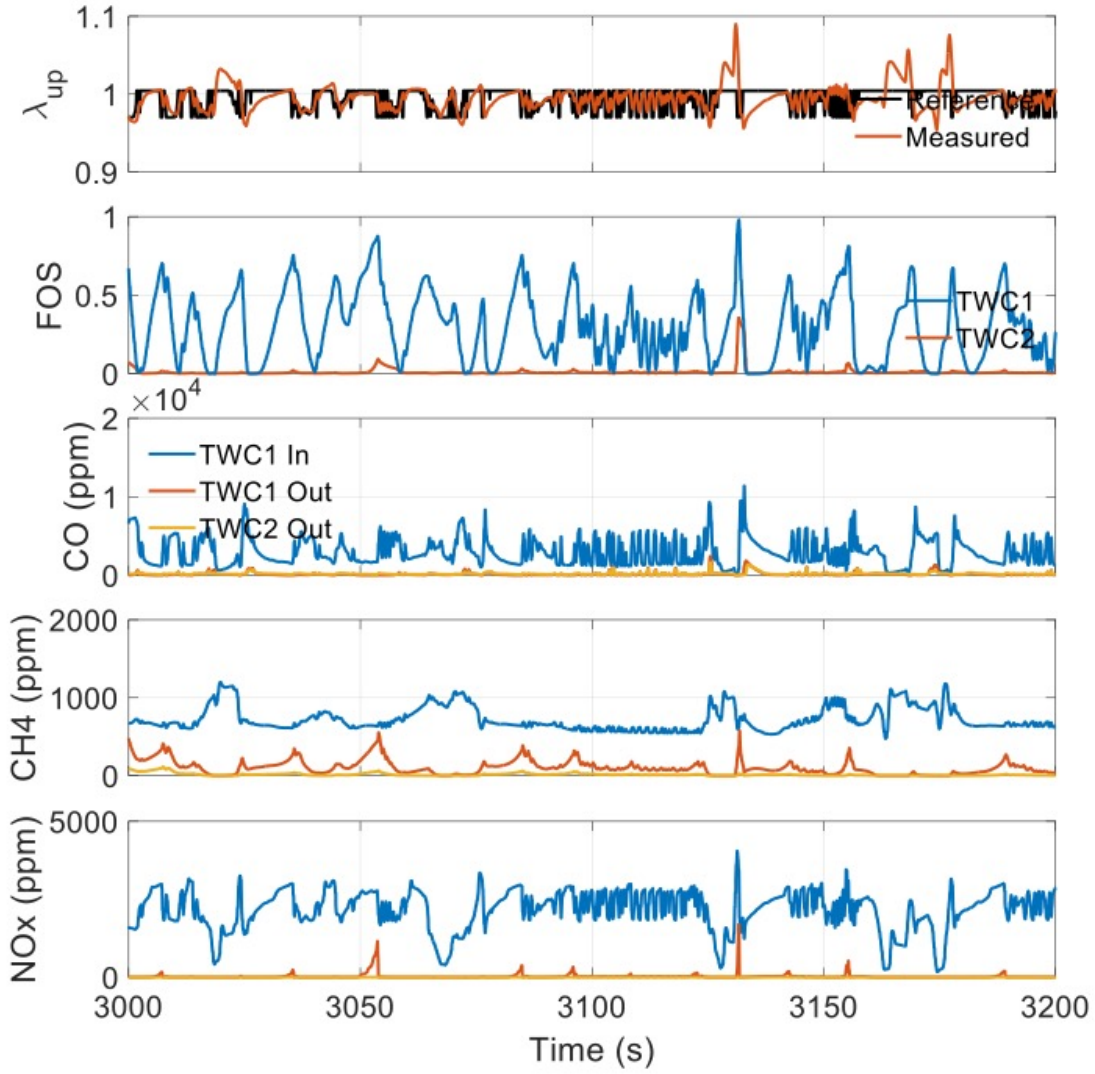


**Figure 2.27.** Strategy 5 - 3000s ~3200s, Warm cycle, without fuel cut.

### 2.9.3 Comparison between Cold cycle vs. Warm cycle, with fuel cut-off

Although outer-loop controller improvement has been the main focus in the thesis, it is still worth taking a look at how TWC has been handling cold cycle and warm cycle differently. Fig. 2.30 and Fig. 2.31 present the initial 200s of cold cycle and warm cycle respectively, using Strategy 5 for engine with fuel cut-off. Despite the fact that TWC doesn't start at equal oxidation level for cold and warm cycle, the emission profiles are still very different for both cases. All three species  $CO$ ,  $CH_4$  and  $NO_x$  are barely reacted during the first 50s

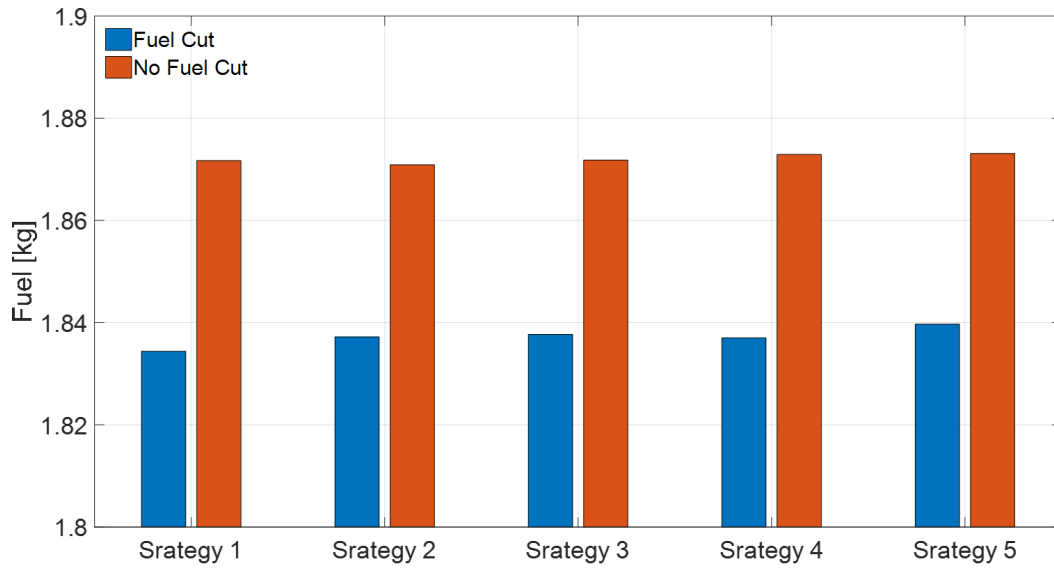


**Figure 2.28.** Fuel Consumption during Warm cycle - Fuel cut vs. No Fuel cut.

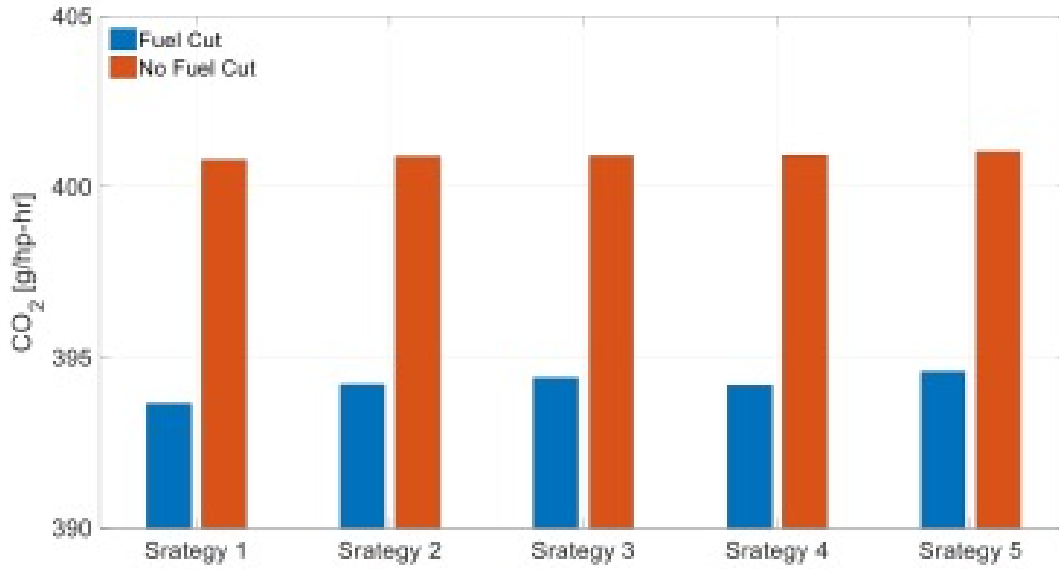


**Figure 2.29.** CO<sub>2</sub> emission during Warm cycle - Fuel cut vs. No Fuel cut.

of cold cycle, while only  $CH_4$  is reluctant in reacting with catalyst for the first 50s of warm cycle. For cold cycle,  $CH_4$  takes around 100s to start reaction and still doesn't perform well enough at 200s. Those are mainly caused by low temperature in the beginning of cycles and

a big amount of time is needed for the catalyst to rise. On top of that,  $CH_4$  requires even higher temperature than  $CO$  and  $NO_x$  to start reaction. Technologies that can help shorten the heating time or improve catalyst capability are needed to solve this problem.

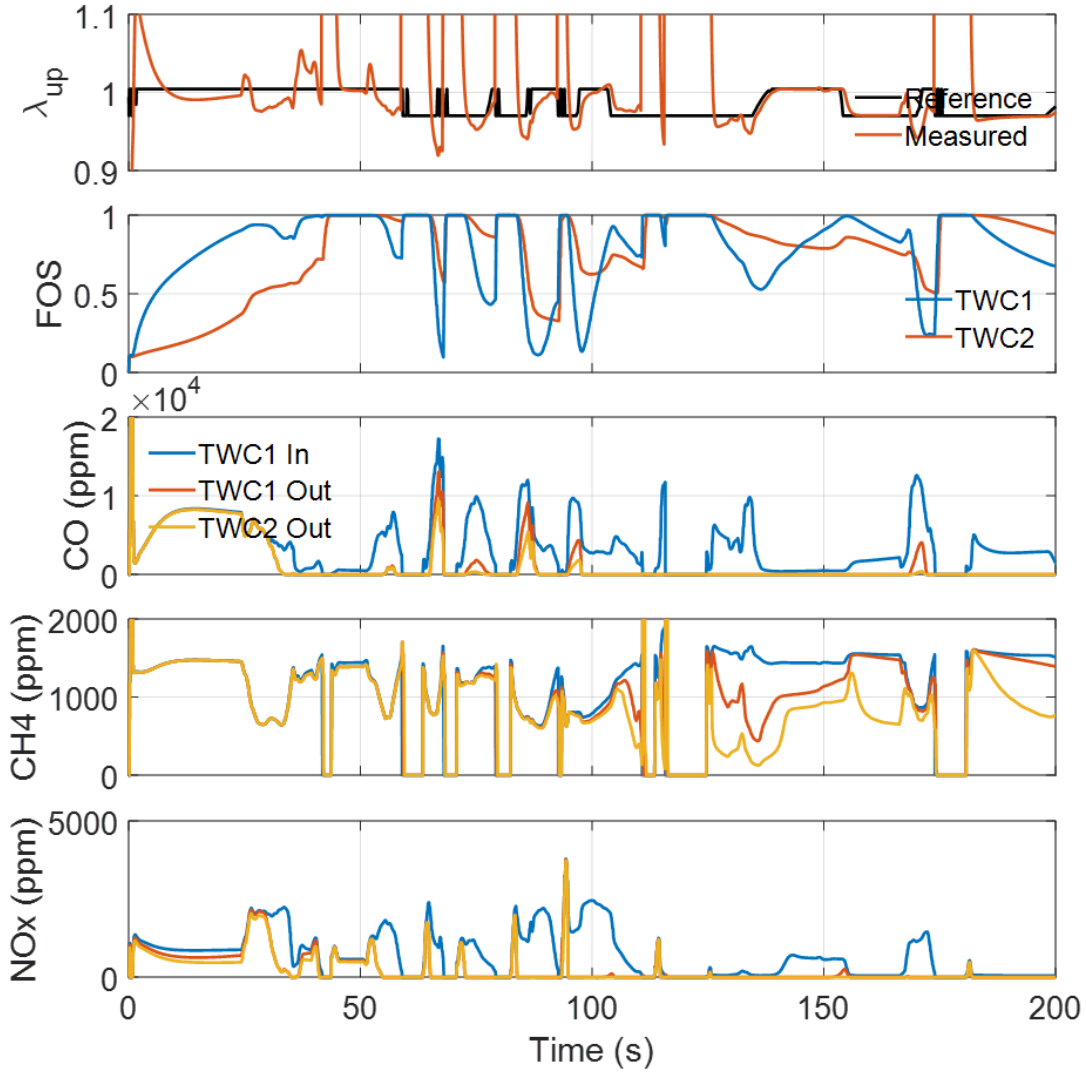


**Figure 2.30.** Strategy 5 - 0s ~200s, Cold cycle, with fuel cut.

## 2.10 Cumulative emission comparison

In this section, emission results from all five control strategies are compared in terms of cumulative tail pipe emissions of  $CO$ ,  $CH_4$  and  $NO_x$ . It is noted that the emission results

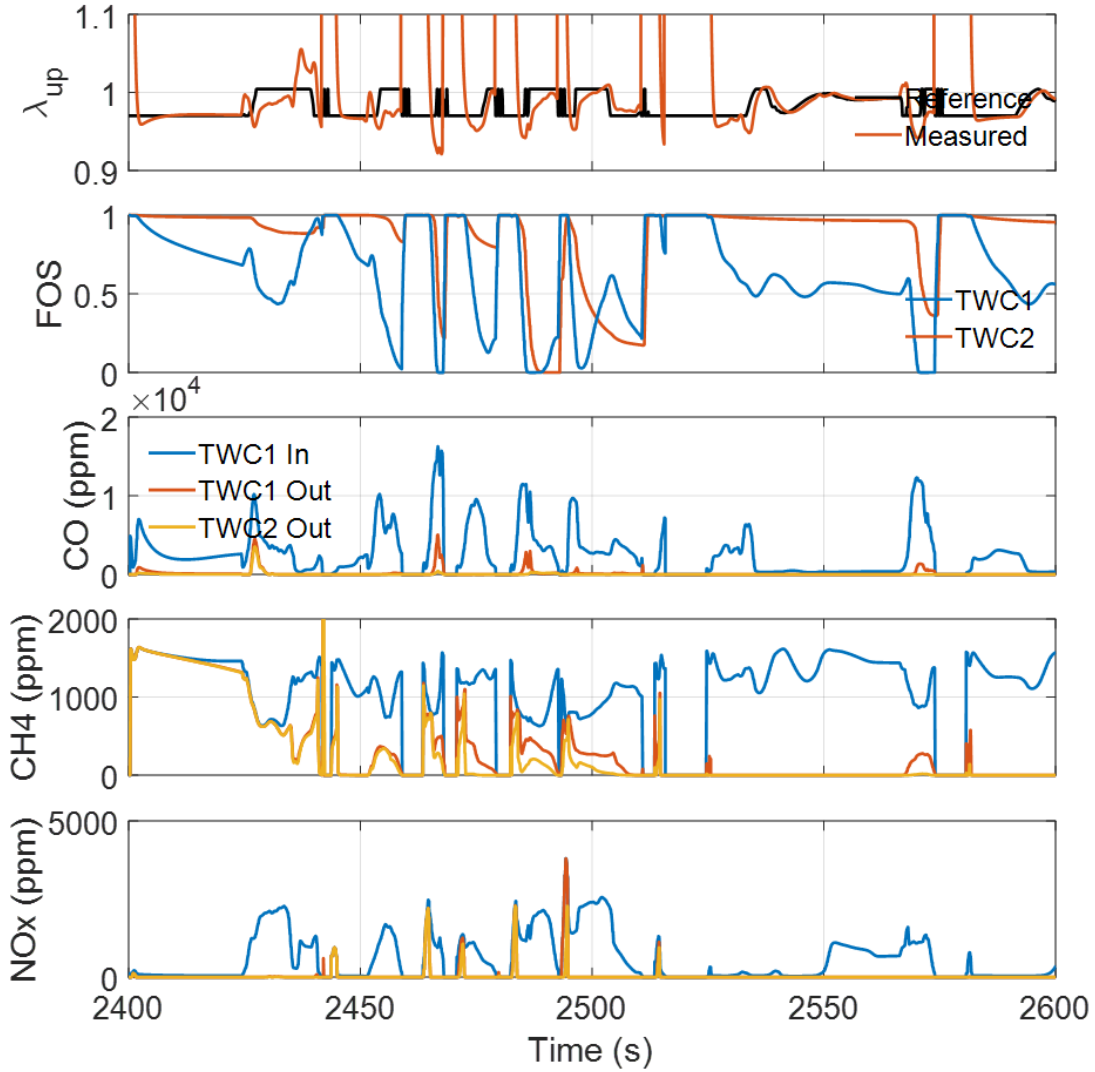


**Figure 2.31.** Strategy 5 - 2400s ~2600s, Warm cycle, with fuel cut.

compared here are what come out of TWC2, while all the outer loop control strategies only include TWC1 in the outer loop. It seems more meaningful to compare what come out of TWC1 since they are the direct output of the two-loop controller. However, it is common practice in industry to always include an auxiliary TWC (i.e. TWC2) as extra buffer considering TWC1's outlet  $\lambda_{dn}$  typically fluctuate in a much smaller range than TWC1 inlet's  $\lambda_{up}$ , thus downstream EGO sensor cannot well indicate whether the system is too rich/lean until the catalyst is already near its full capacity. Therefore, the tail pipe emission results are presented because they are consistent with what will be tested in practice and it is still an

“apple-to-apple” test. In the rest of the section, the emission results of cold cycle and warm cycle will be talked about separately before ending this chapter with the overall weighted emission results.

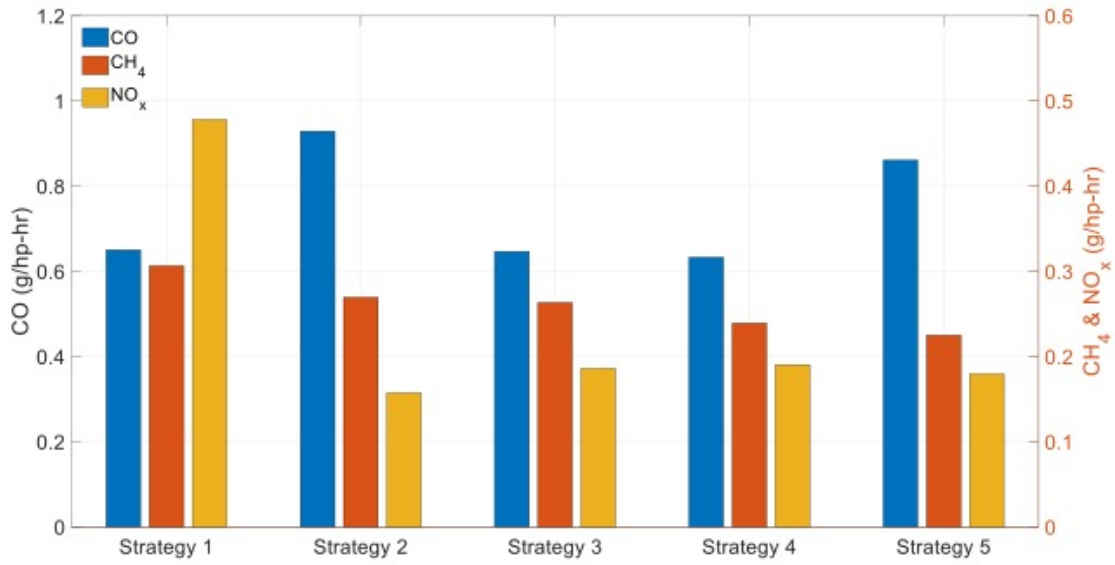
As is illustrated in last section, control strategies are less effective in cold cycles than in warm cycles, because of low temperature at the beginning.  $CH_4$  is affected the most because it requires the highest reaction temperature of the three gases. A comparison of outlet emissions for a cold-start cycle versus a warm-start cycle, for engine with fuel cuts, is shown between Fig. 2.32a and Fig. 2.32b. Both cold cycle and warm cycle shows great  $NO_x$  reduction when comparing outer loop control Strategies 2 ~5 with Strategy 1, by more than 50%. There is also a noticeable  $CH_4$  reduction when outer loop controllers are used, by more than 10%. On the other hand,  $CO$  emission is not reduced with outer-loop implementation. It is probably because  $CO$ 's conversion efficiency is higher in lean condition, thus it shows an opposite tendency than  $NO_x$ ; while  $CH_4$  is slightly better because it's less sensitive to overly rich/ lean condition and is more close to  $\lambda$  window with outer loop controllers. Last but not the least, the warm cycle's outlet emissions are significantly lower for all three gases ( $CO$ ,  $CH_4$  and  $NO_x$ ) as expected.

A comparison of outlet emissions for a cold-start cycle versus a warm-start cycle, for engine with fuel cuts, is shown between Fig. 2.33a and Fig. 2.33b. A generally similar conclusion to the fuel cut cases is drawn here. Outer loop controllers'  $NO_x$  reduction is significantly better by more than 60%, while their  $CH_4$  reduction is better by more than 8%.  $CO$  emissions are sometimes higher and sometimes lower with outer-loop implementation.

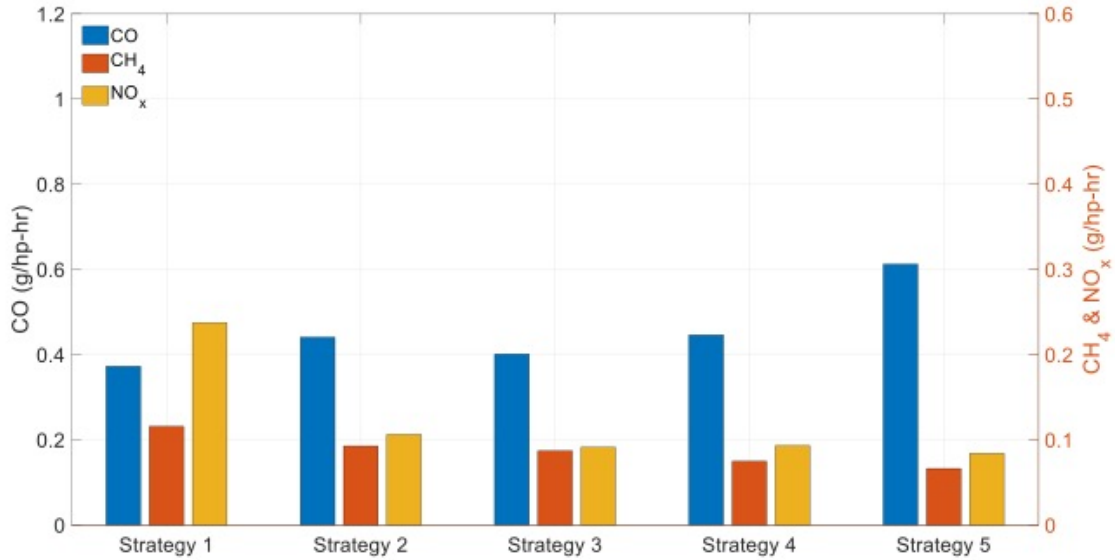
Finally, the weighted emission results of  $CO$ ,  $CH_4$  and  $NO_x$  for fuel-cut and no-fuel-cut are shown in Fig. 2.34 and Fig. 2.35, respectively. Observations from Fig. 2.34 include:

1. Outer loop Strategies 2 ~5 significantly improve  $NO_x$  emission than Strategy 1 by 58%, 61%, 61% and 64%, respectively.
2. Outer loop Strategies 2 ~5 significantly improve  $CH_4$  emission than Strategy 1 by 17%, 21%, 31% and 38%, respectively.
3.  $CO$  emission is not reduced with implementation of outer loop controllers.
4. FOS-based Strategies 4 & 5 gains equal or slightly better  $NO_x$  emission, and noticeably better  $CH_4$  emission than  $\lambda_{dn}$  based controller.





(a) Cold start cycle.

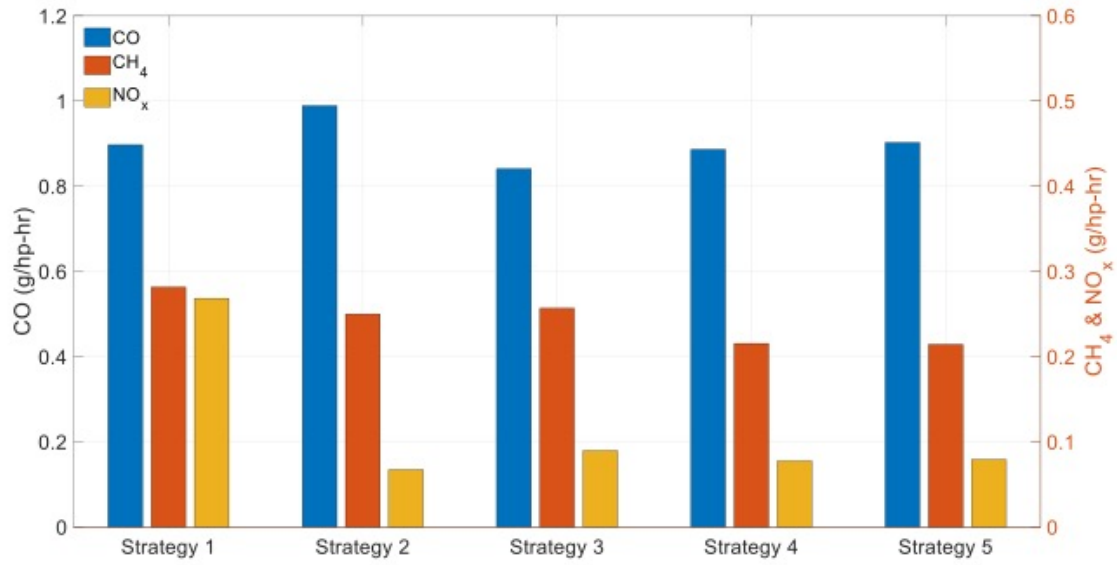


(b) Warm start cycle.

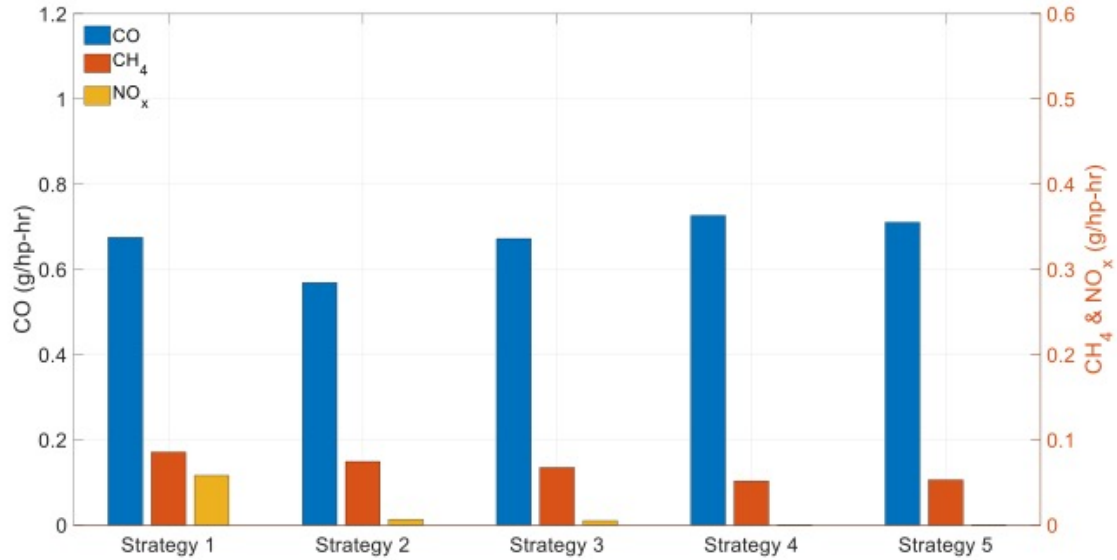
**Figure 2.32.** Emission comparison for engine with fuel cut-off.

5. FOS-based robust controller gains modestly better  $NO_x$  and  $CH_4$  emission than FOS-based PI controller.

6. Although Strategy 3 is the simplest of all outer loop Strategies tested, it works very well in emission reduction.



(a) Cold start cycle.



(b) Warm start cycle.

**Figure 2.33.** Emission comparison for engine without fuel cut-off.

Observations from Fig. 2.35 include:

1. Outer loop Strategies 2 ~5 significantly improve  $NO_x$  emission than Strategy 1 by 82%, 80%, 87% and 87%, respectively.

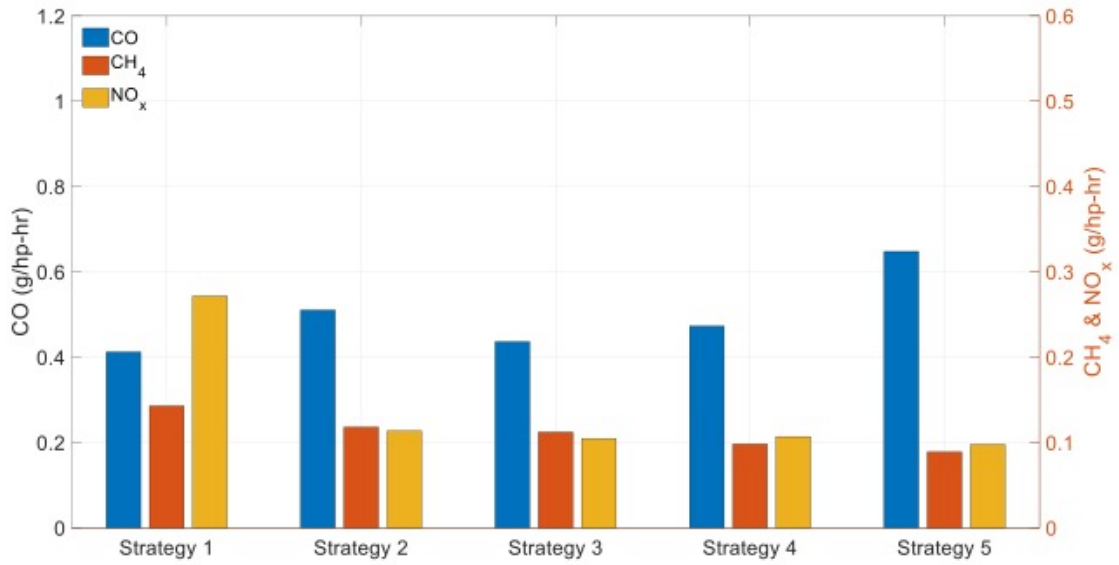


**Figure 2.34.** Weighted Otto-FTP emission for engine with fuel cut-off.

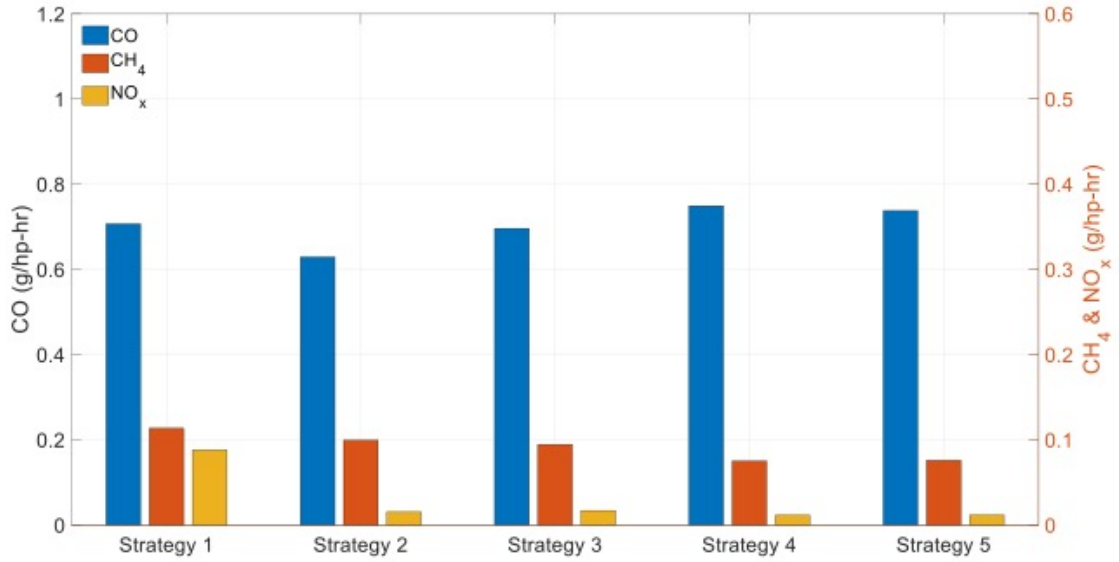


**Figure 2.35.** Weighted Otto-FTP emission for engine without fuel cut-off.

2. Outer loop Strategies 2 ~5 significantly improve  $CH_4$  emission than Strategy 1 by 12%, 16%, 34% and 33%, respectively.

3.  $CO$  emission is slightly reduced with  $\lambda_{dn}$  based controllers, but not FOS-based controllers.

4. FOS-based Strategies 4 & 5 gains noticeably better  $CH_4$  and significantly better  $NO_x$  emission than  $\lambda_{dn}$  based controller.

5. FOS-based robust controller gains equal emission performance to FOS-based PI controller.

6. Strategy 3 still works very well in emission reduction.

7. Control strategies in engine without fuel cut-off gains noticeably better  $CH_4$  and significantly better  $NO_x$  than with fuel cut-off.

In conclusion, outer-loop control is essential for the reduction of  $NO_x$  emissions when fuel cuts are included. However, the reduction of  $NO_x$  achieved by FOS-based strategies is not significant over non-FOS-based strategies. But once fuel cuts are eliminated, FOS-based outer-loop control strategies result in 40-50% lower  $NO_x$  than other outer-loop control strategies. To still keep FOS-based controller's competence while getting good fuel economy, either fuel cut-off is replaced with other possible fuel saving technologies, or the side-effect of fuel cut-offs are reduced/ eliminated for the benefit of TWC after-treatment system.

## 3. NATURAL GAS SI ENGINE MODELLING

### 3.1 Project background

The work is funded by Cummins Inc. under the project of investigation on potential benefits of variable valve actuation (VVA) on a stoichiometric SI natural gas engine.

The goal of the project is to investigate the impact of VVA on the gas exchange process on SI natural gas engines, with purpose of improving the engine performance, especially in reducing engine knock tendency at low-speed/ high-load conditions, minimizing throttling losses at part loads for improved efficiency, and improving transient torque response. With VVA implemented, the project also expects to make environmental impact by reducing greenhouse gas (GHG, e.g., CO<sub>2</sub>) emissions.

In SI engines, engine knocking occurs when combustion of some of the air/fuel mixture in the cylinder does not result from propagation of the flame front ignited by the spark plug, but rather from self-ignition when the pistons are half-way up to the top dead center (TDC). The shock wave creates the characteristic metallic “pinging” sound, and cylinder pressure increases dramatically. This can also create incredible heat that can break the cylinders and pistons shortly.

For a stoichiometric SI engine (e.g., gasoline & natural gas), it operates with a constant air-to-fuel ratio (AFR). A fixed air-to-fuel ratio means as load demand increases, both the fuel flow and air flow needs to be raised. On the other hand, a compression-ignited engine (e.g., diesel) varies air-to-fuel ratio to meet varied torque demand. In SI natural gas engine, a throttle valve is deployed at the intake manifold to control varying loads. The throttle valve restricts the air flow when the engine is operating at low loads, which leads the engines to put more work in pumping gases. The loss that incurs at low loads is called part load throttling loss.

### 3.2 Cummins B6.7N engine

A Cummins B6.7N natural gas powered SI engine (Fig. 3.1) is installed and tested on the ground floor of the Ray W. Herrick Laboratories. This engine is widely used for the school

bus, shuttle, and medium-duty truck markets. The benefit of the B6.7N is that it uses 100% natural gas, featuring spark-ignited stoichiometric combustion with cooled EGR and a three-way catalyst. It integrates a closed crankcase ventilation (CCV) system and on-board diagnostics (OBD) for optimal emission performance. It is certified to CARB optional low  $NO_x$  0.02 g/bhp-hr (90% lower than current EPA standard: 0.2 g/bhp-hr), while exceeding 2017 EPA GHG requirements.



**Figure 3.1.** Cummins B6.7N spark-ignition natural gas engine.

As shown in Fig. 3.2, the engine test cell consists of engine block (cylinders and crankshaft), intake and exhaust manifolds, fuel injection system, turbocharger, charged air cooler (CAC), and exhaust gas re-circulation (EGR). Air and fuel mix before distributed into each cylinder

**Table 3.1.** Cummins B6.7N engine specifications.

Maximum Horsepower	240 HP / 179kW
Peak Torque	560 lb-ft / 759 Nm
Governed Speed	2400 RPM
Type	4-cycle, spark-ignited, in-line 6 cylinder, turbocharged, CAC
Engine Displacement	409 CU IN / 6.7 Liters
Number of Cylinders	6
Operating Cycles	4
Net Weight (Dry)	1,150 lb / 522 KG
Fuel Type	CNG / LNG / Biomethane

through intake manifold; After combustion, the engine exhaust gas exits through exhaust manifold, part of it going through turbocharger and the other part of it going back into the system via exhaust gas re-circulation (EGR).

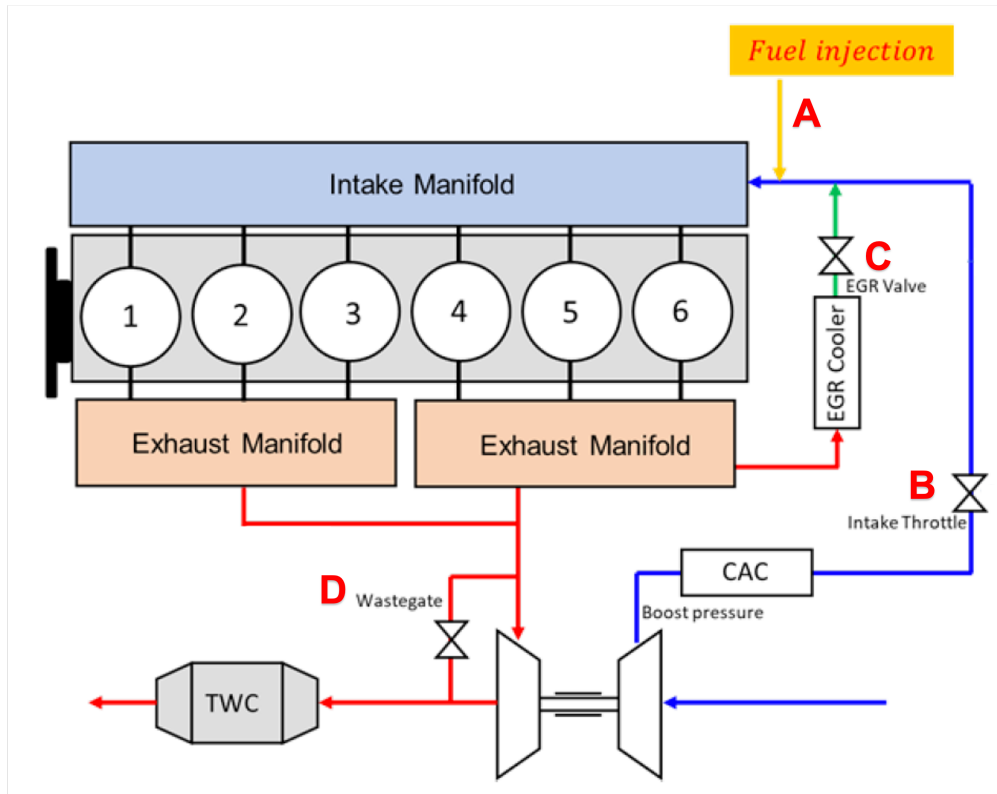


**Figure 3.2.** Engine schematics.

There are four controllers in the engine system, and the locations are indicated in Fig. 3.2:

### 3.2.1 AFR controller

This controller inputs target AFR to fuel injection system upstream of intake manifold, so the fuel injector will decide the fuel rate/ amount based on measured air flow. Typically the target AFR is constant at stoichiometry.

### 3.2.2 Intake throttle controller

The intake throttle valve controls the throttle opening and thus the intake air flow, in order to meet the required torque demand.

### 3.2.3 EGR fraction controller

Exhaust gas re-circulation (EGR) is a  $NO_x$  emission reduction technique used in internal combustion engines. By circulating and cooling small amounts of exhaust gases into the intake manifold to mix with the incoming air/fuel charge, the EGR system dilutes the air/fuel mixture (especially reduces  $O_2$ ), which reduces peak combustion temperatures and pressures, resulting in an overall reduction of  $NO_x$  output [18]. Here, the EGR valve is controlled by target EGR fraction commanded from the engine control module (ECM), so that the desired amount of recirculated exhaust gas is attained.

### 3.2.4 Boost pressure controller

The waste gate valve is controlled by inputting target compressor outlet pressure, and thus determine the turbine performance.

## 3.3 Measurement system

In the test cell, multiple data collection/ control systems are used for different purposes:



### **3.3.1 dSPACE**

dSPACE offers hardware and software platform with I/O functionalities. In the test, the dSPACE ControlDesk is used to read external sensor data such as temperature, pressure, air & fuel flow, and some data from the dynamometer (rpm & torque). It is also used for controlling valve lift profiles of the variable valve actuation system which will be shown later in Chapter 4.

### **3.3.2 Calterm**

Calterm is used for the engine control module (ECM). In the test, it also provides some ECM data that either are measured from the engine's stock sensors, or based on internal calculations.

### **3.3.3 Indicom Indicating software**

IndiCom is a software package in the field of combustion analysis that combines the control of data acquisition with professional data evaluation for clear graphical presentation. In the test, Indicom is used together with in-cylinder pressure sensors and crank angle sensors to calculate the engine performance and efficiency parameters.

### **3.3.4 Power Test Dynamometer**

A dynamometer (dyno) is a device that measures force, torque or power. For chassis or engine applications, a dynamometer is designed to create a load to duplicate various speed (RPM) and torque (N-m or lb-ft) requirements. From this data, power (HP or kW) can be calculated. This in turn provides a snapshot of the chassis or engine performance for comparison with the manufacturer's specifications. Power Test, LLC. is an industry leader in the design, manufacture, and sale of dynamometers.

### 3.4 GT-Power engine modelling

GT-SUITE, which includes the GT-Power Engine library, is the leading engine and vehicle simulation tool used by engine makers and suppliers. It is a single software package for modeling and simulation of systems in automotive and transportation engineering and beyond. It is based on a multi-physics platform, and covers a broad set of applications, including but not limited to engine, exhaust, acoustics, vehicle dynamics, hydraulics and pneumatics, etc.

GT-Power is used for a wide range of activities related to engine design and development, to predict either steady-state conditions or transient behavior of engine systems. The model is based on one-dimensional (1-D) fluid dynamics, representing the flow and heat transfer in the piping and other flow components of an engine system. The outputs can include single-valued quantities (such as averages, maximums, and minimums), or crank-angle or time-resolved quantities. The advantage of 1-D simulations over higher-dimensions is its significant reduction in computational time and power, which is preferable for complicated systems like vehicle engine design and performance testing.

GT-Power models are built by a highly versatile graphical user interface (GUI), from a library of GT-supplied templates or user-defined reusable compound objects. The main GUI of the model representing the B6.7N engine is built as shown in Fig. 3.3.

The blocks shown in the GT model above represent:

- Mixer: In the mixer, intake air, recirculated exhaust gas, and injected fuel are mixed before entering the intake manifold and distributing into all cylinders. Two controllers mentioned previously, intake throttle controller and AFR controller, are located in this block. The cooled intake air from charge air cooler is regulated by intake throttle valve based on desired brake torque demand, before mixing with cooled recirculated exhaust gas from EGR, and compressed natural gas (CNG) from fuel injection system based on AFR command.

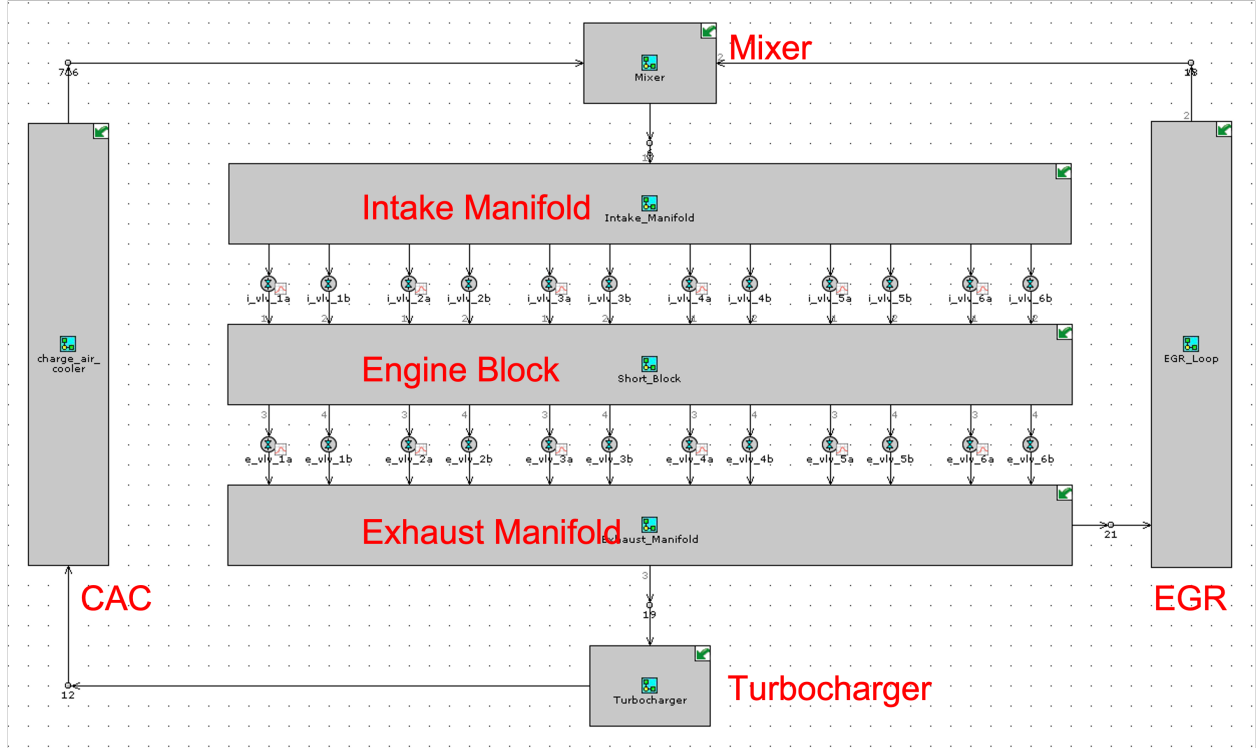


**Figure 3.3.** GT-Power engine model.

- **Intake Manifold:** The mixed gas from Mixer goes into Intake Manifold before being distributed into each cylinder. It is expected to evenly distribute the gas into each cylinder with very slight differences caused from intake manifold geometry.
- **Engine block:** The Engine Block includes the six cylinders and the crank shaft. All the cylinders share the same geometry, and work 120 crank angle degrees apart under the firing order of 1-5-3-6-2-4 (cylinder numbers are counted from left to right). The mixed gas enters engine block for reaction and the reacted gas exit the engine block into Exhaust Manifold. The timings and amount in terms of intaking and exhausting the gases are regulated by valves (two intake valves and two exhaust valves for each cylinder).
- **Exhaust Manifold:** The Exhaust Manifold includes the split exhaust architecture downstream of the Engine Block. It distribute reacted gas from the engine to both the turbine in Turbocharger and EGR module.

- EGR: EGR module takes certain amount of reacted gas through EGR valve based on the targeted EGR fraction controller and also cools down the recirculated exhaust gas by certain level before the gas goes back to the Mixer for another round of engine reaction.
- Turbocharger: The Turbocharger includes a turbine, a compressor, and the previously mentioned wastegate valve (boost pressure controller). The compressor takes in certain amount of pure air and compresses it before it goes to the charge air cooler (CAC). The turbine provides power to the compressor through turboshaft and its performance is controlled by the wastegate valve based on target compressor outlet pressure command.
- CAC: The CAC (charge air cooler) cools the compressed intake air before sending it into Mixer.

All four controllers mentioned in previous section can be setup in the GT-Power model, by inputting the target AFR, target EGR fraction, target brake torque, and target compressor outlet pressure data, from either test cell measurement data or engine fuel map.

To assure the GT-Power model's friction mean effective pressure (FMEP) is close to test cell measurement (calculated) data, the GT-Power model uses Chen-Flynn Engine Friction Model, which is:

$$FMEP = FMEP_{Const} + A \times P_{Cyl,max} + B \times c_{p,m} + C \times c_{p,m}^2 \quad (3.1)$$

where,

$FMEP_{Const}$	Constant part of FMEP
$A$	Peak cylinder pressure factor
$B$	Mean piston speed factor
$B$	Mean piston speed squared factor
$c_{p,m}$	Mean piston speed
$P_{Cyl,max}$	Maximum cylinder pressure

### 3.5 Engine fuel map and Tested operations

The engine fuel map for the Cummins B6.7N natural gas SI engine contains 125 operating points. Before the VVA platform was installed on the engine, the engine was tested at rated operation (2400rpm, 543lb-ft) with set boundary conditions, and run and measured at 8 other baseline operations (9 operating points in total) for GT model and VVA reference, as shown in Fig. 3.4 and Table 3.2 below.

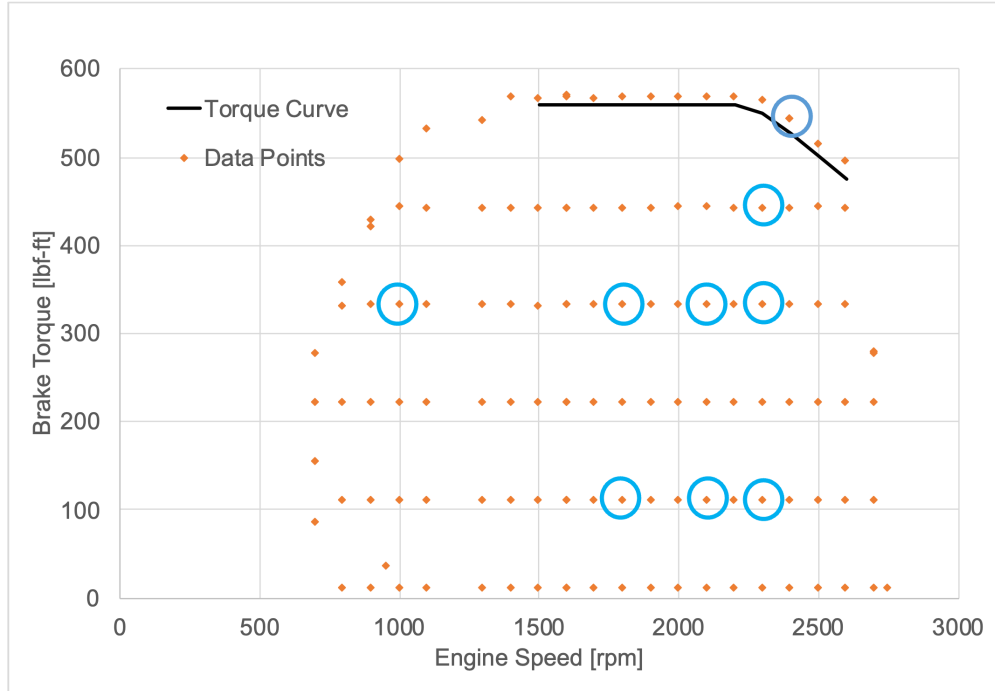


**Figure 3.4.** Engine fuel map and Tested baseline operating points (circled).

**Table 3.2.** Tested baseline operating points.

Case Number	1	2	3	4	5	6	7	8	9
Engine Speed (RPM)	2400	2300	2300	2300	2100	2100	1800	1800	1000
Brake Torque (ft-lbf)	543	442	332	111	332	111	332	111	332

### 3.6 Burn rate calculation from measured cylinder pressures

Burn rate calculation is a “reverse run” simulation in GT-Power. A typical “forward run” in engine combustion simulation uses the burn rate as input to result in the cylinder

pressure. While in this work, the cylinder pressure is used for “reverse running” its burn rate.

Two available approaches to calculate the apparent burn rate from measured cylinder pressure trace were investigated and compared in the work: closed volume analysis (also known as cylinder pressure only analysis, i.e., CPOA) and three pressure analysis (TPA).

### 3.6.1 Closed volume analysis

Closed volume analysis is a stand-alone, single-cylinder calculation with only the measured cylinder pressure. As shown in Fig. 3.5, the model for SI engine only includes the engine’s cylinder and crank train. The analysis requires following primary inputs:

- Measured single cylinder pressure vs. crank angle.
- Cycle averaged variables including volumetric efficiency, trapping ratio, and residual gas fractions.
- Engine’s cylinder and crank geometries.

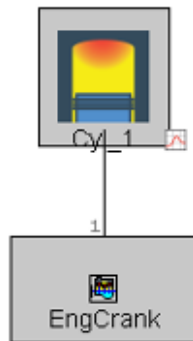


**Figure 3.5.** Closed volume analysis (CPOA) setup.

The benefit of CPOA is that it’s computationally fast and only requires single cylinder pressure measurement due to its simplicity in GT setup. On the other side, because of the presumptions in the model, an inaccurate estimation on the variables, namely the trapping

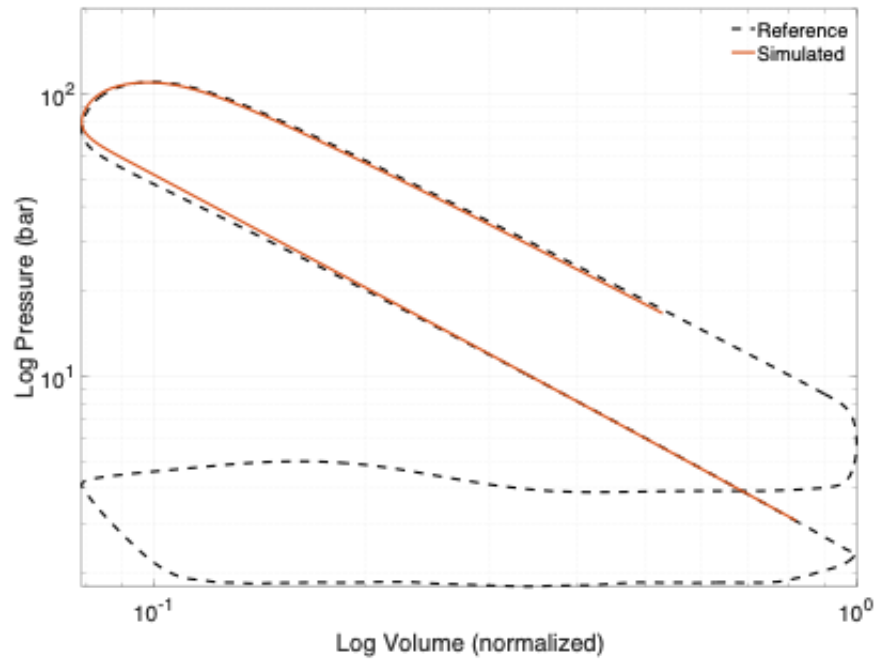
ratio and residual fraction which are difficult to measure in the engine, can have large impact on calculated burn rate profile.

After CPOA simulation, the  $\text{LogP} \sim \text{LogV}$  diagram is shown in Fig. 3.6a and the normalized cumulative burn rate (or mass burn fraction - MBF) is shown in Fig. 3.6b . In Fig. 3.6a, the simulated  $\text{LogP} \sim \text{LogV}$  curve mostly coheres with measured  $\text{LogP} \sim \text{LogV}$  curve at the power loop (i.e., the upper loop in the PV cycle), while it can be observed that CPOA didn't render any pumping loop (i.e., the lower loop in the PV cycle). That is because there was no valve lift inputs to the CPOA method which gives no information about the intake/ exhaust valve opening/ closing and thus didn't closed the PV cycle. However, the combustion in cylinders starts at the end of compression stroke (before the piston reaches cylinder's top dead center - TDC), and ends before the exhaust valves opens (long before the end of power stroke), so CPOA can still calculate the complete transient and cumulative burn profile, and as shown in Fig. 3.6b, the normalized cumulative burn rate starts from 0 (typically before TDC) and raises and converges to 1 (100%) before exhaust valve closing (136 crank angle degree in here).

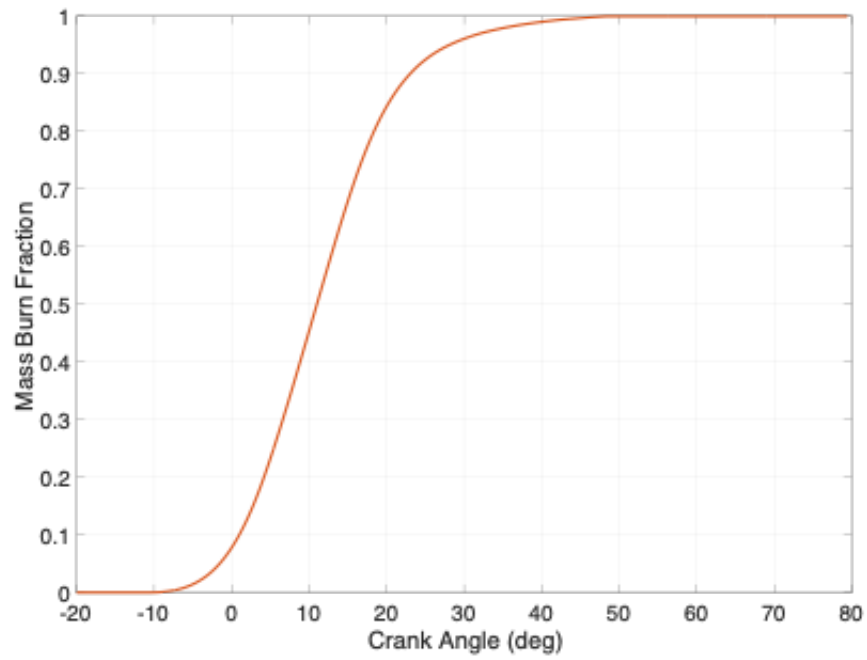
Despite the ease of setup and fast computation, CPOA was not optimal for burn rate calculation because of requirements for accurate parameter estimations (trapping ratio, residual gas fractions, and gas mixture composition for lack of EGR information). However, a research work for in-cylinder laser sensing is being carried out within this project frame on parallel with the engine testing work, with expectation to gain capability of measuring/ calculating cylinders' trapped mass, temperature, and composition, which if proven successful, is very promising to enhance CPOA accuracy and ease the burn rate calculation process.

### 3.6.2 Three pressure analysis

Three pressure analysis (TPA), different from CPOA, uses three different measured pressures, including intake port pressure, in-cylinder pressure(s), and exhaust port pressure. Therefore, a TPA setup requires an engine model including valves (which are not required in CPOA) and ports at a minimum.



(a) LogP~LogV diagram: Simulated vs. Measured.



(b) Mass burn fraction.

**Figure 3.6.** CPOA at rated (2400rpm, 543 ft-lbf) - Cylinder #1.



The approach is to take measurements at steady-state operating condition – whereby measurement data is either ensemble averaged or only of a single cycle – to analyze the pressure measurements, in order to obtain a single combustion burn rate for each operating condition.

The benefit of TPA is that all the cylinder trapped quantities are predicted from the simulation, including cylinder trapping ratio and residual fraction (which need to be estimated/ presumed for CPOA to work). While the downside of TPA is that it requires more measured pressure data which raises experiment cost and also requires a longer computation time than CPOA due to its complexity.

The analysis requires following primary inputs:

- Measured cylinder pressure trace (or traces, for multi-cylinders).
- Measured intake port/ manifold pressure trace.
- Measured exhaust port/ manifold pressure trace.
- EGR fraction, Fresh charge mass composition, and boundary temperatures.
- Intake and exhaust valve lift profiles.
- Engine’s cylinder and crank geometry.

Two different TPA setup strategies were investigated: one covers only one cylinder, and the other covers multiple cylinders (all 6 cylinders in this work).

### **Single cylinder setup**

The first setup, similar to CPOA, is to look at only one cylinder and its intake and exhaust ports. Difficulties that arise from this type of setup include the requirement of higher resolution data capture in the intake and exhaust ports. However, if such data is attainable, this method is believed to provide a more accurate calculated burn rate than the previously discussed method (CPOA). In the test cell, considering the space constraint and limit on time and budget as well, it is not practical to install the intake and exhaust

pressure sensors too close to the cylinder. Thus the real measurement locations in the test engine are at the intake manifold split pipe for the intake side and before the turbine inlet for the exhaust side. By doing so, it introduces some complexities especially on the exhaust side, so such a setup may not be as accurate as expected. The detailed TPA setup for single cylinder, with some modification on the exhaust side (by taking out split pipes connecting other cylinders), is shown in Fig. 3.7.

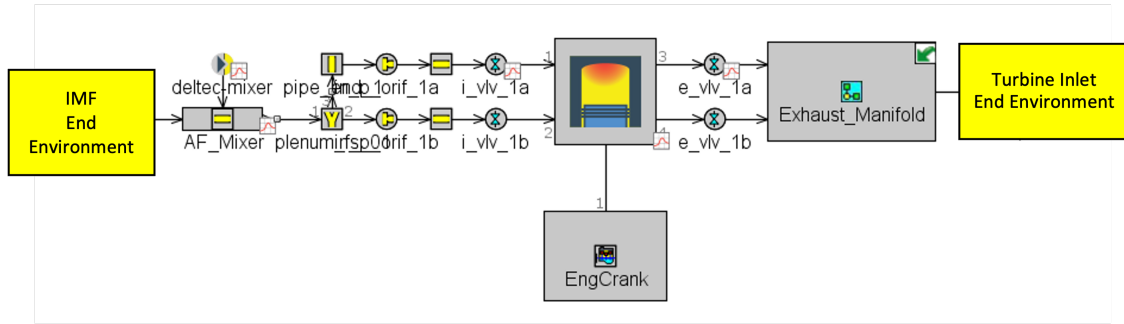
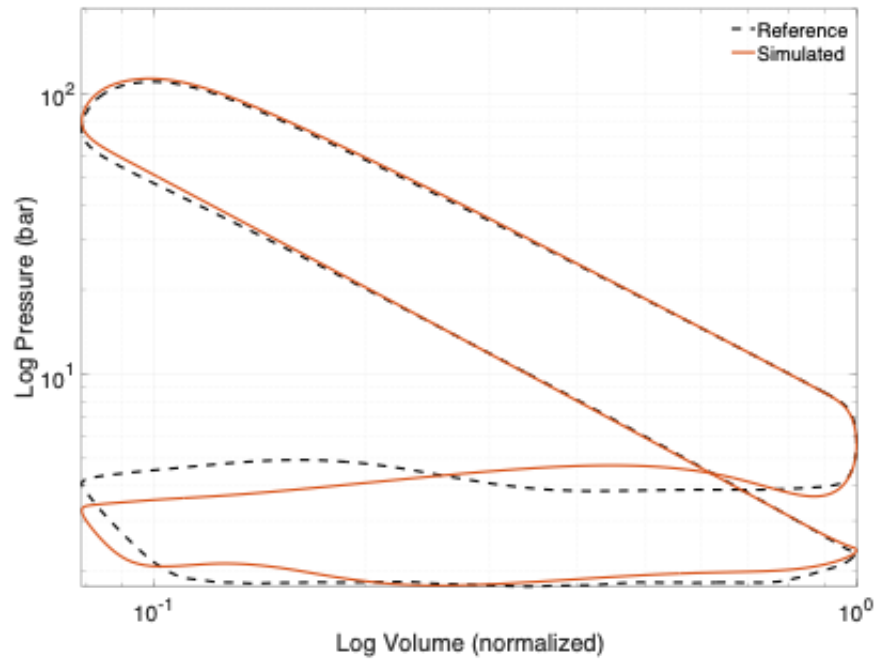
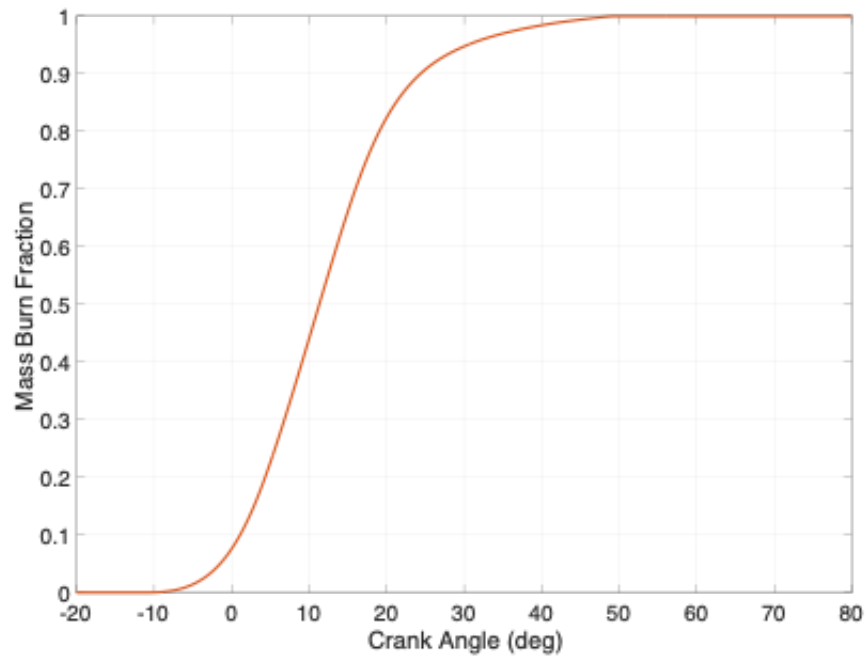


**Figure 3.7.** Three pressure analysis (TPA), Single cylinder setup.

After running simulation under this single cylinder TPA setup, the  $\text{LogP} \sim \text{LogV}$  diagram is shown in Fig. 3.8a and the normalized cumulative burn rate (or mass burn fraction - MBF) is shown in Fig. 3.8b. In Fig. 3.8a, the first noticed difference from CPOA's result is that the simulated  $\text{LogP} \sim \text{LogV}$  curve now completes a full cycle, instead of only the upper combustion part. The compression and power strokes (upper part, or the power loop) mostly coheres with measured  $\text{LogP} \sim \text{LogV}$  curve. However, the lower loop's  $\text{LogP} \sim \text{LogV}$  estimation is still not coherent with the test cell data. This is partly because the TPA setup doesn't (and also doesn't need to) include the turbocharger for burn rate calculation since the combustion only happens within the power loop. So the discrepancy at the pumping loop of  $\text{LogP} \sim \text{LogV}$  diagram can be ignored for this step. The simulated  $\text{LogP} \sim \text{LogV}$  diagram from TPA-single-cylinder and CPOA look very similar except that the TPA-single-cylinder follows along the reference longer than the CPOA.



(a) LogP~LogV diagram: Simulated vs. Measured.



(b) Mass burn fraction.

**Figure 3.8.** TPA single cylinder at rated (2400rpm, 543 ft-lbf) - Cylinder #1.

## Multiple cylinder setup

In this setup, instead of looking at a single cylinder and its intake and exhaust ports, it takes the entire intake manifold, engine block, and exhaust manifold into consideration, and sets boundary conditions outside of intake and exhaust manifolds, as shown in Fig. 3.9.

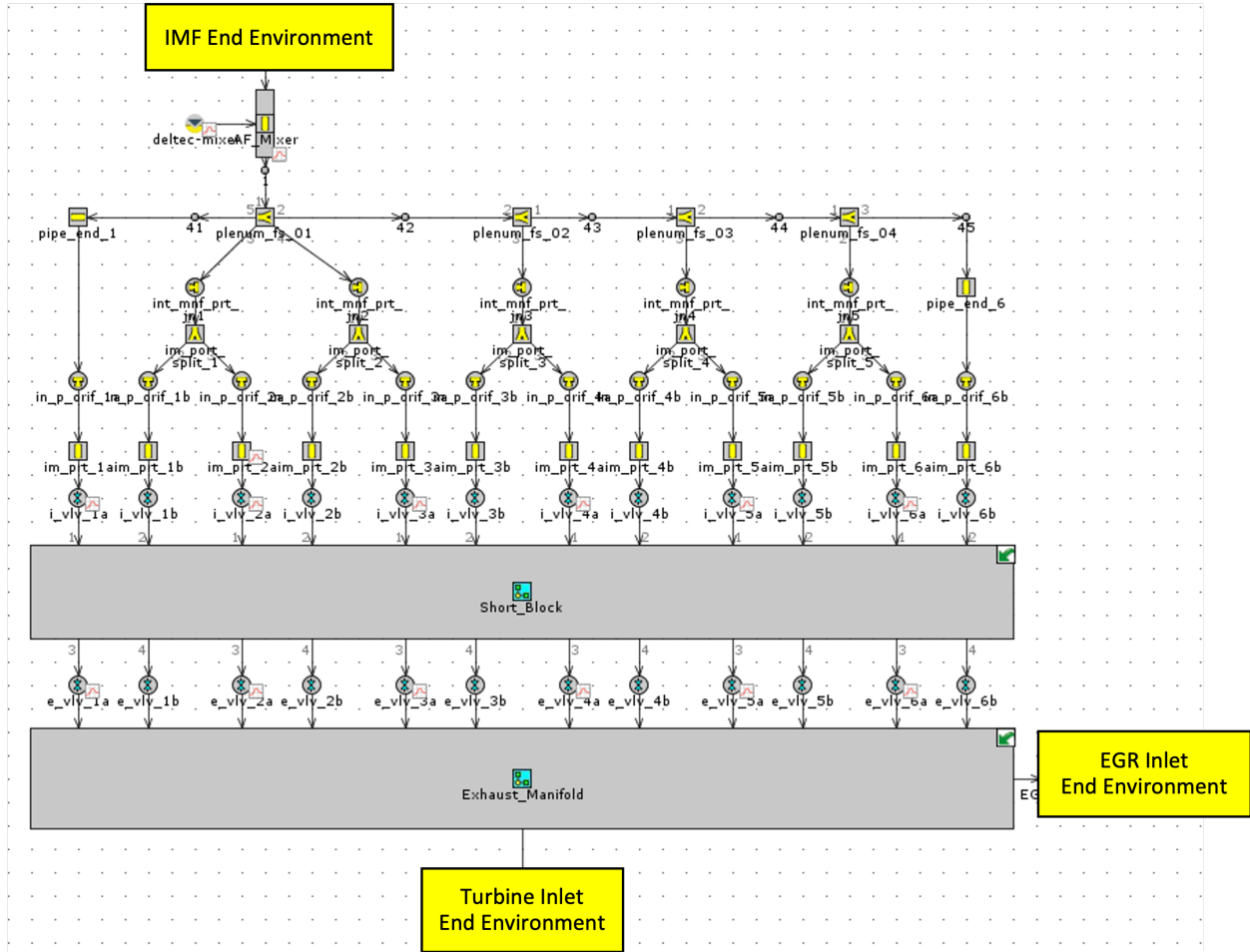


**Figure 3.9.** Three pressure analysis (TPA), Multi-cylinder setup.

Similar to the the single cylinder TPA setup, because its intake & exhaust pressure measurements are also far from engine cylinders, which inevitably brings more complexity into the analysis and relies more on the model accuracy for the inclusion of entire intake and exhaust manifolds. However, the upside of this setup method over the others is that fewer structural changes are needed from the GT-power model than single cylinder setups where several parts need to be modified for accommodating from six cylinders to only one cylinder;

With multi-cylinder setup, each cylinder can also associate with its corresponding pressure curve independently, generating its own burn rate profile.

After running simulation under this multiple cylinder TPA setup, the LogP~LogV diagram is shown in Fig. 3.10a and the normalized cumulative burn rate (or mass burn fraction - MBF) is shown in Fig. 3.10b. Similar to TPA-single-cylinder setup, the simulated LogP~LogV diagram complete a full cycle, with good match at the power loop and poor match at the pumping loop.

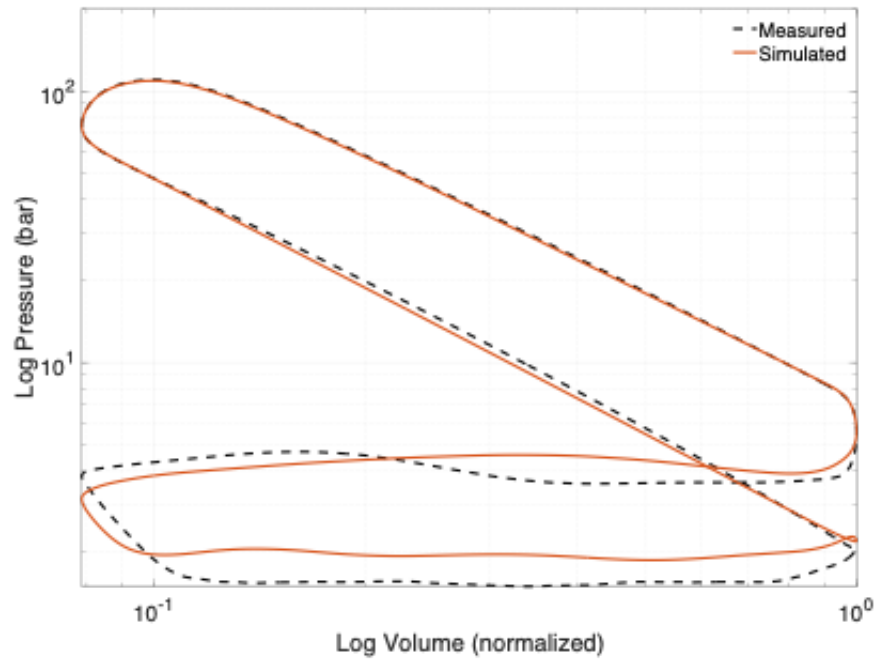
Fig. 3.11 includes the LogP~LogV diagram of each cylinder. As was illustrated previously, this multi cylinder setup can input each cylinder's own pressure curve and thus calculate each of its own burn profile.

### 3.6.3 Comparison of different pressure analysis methods

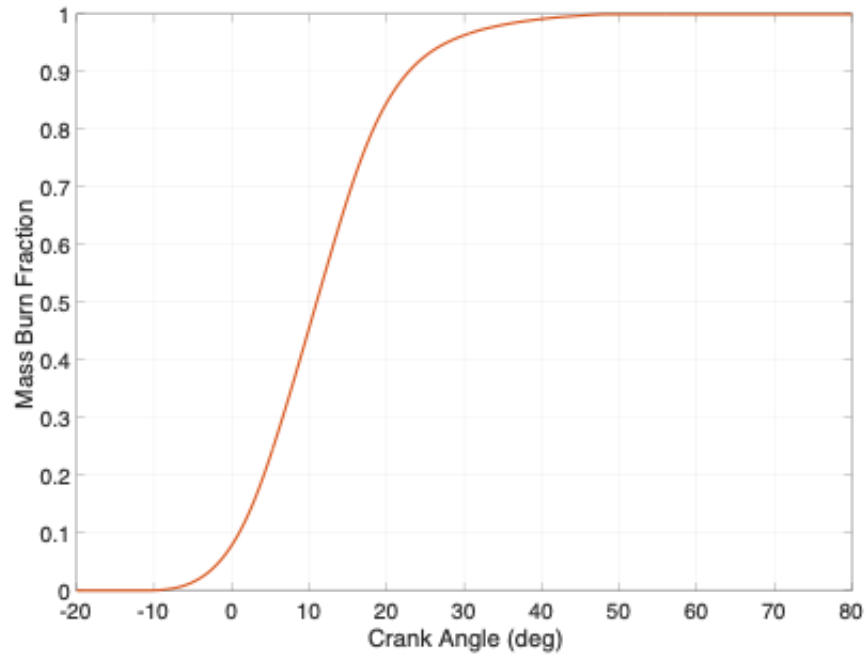
In Fig. 3.12, all three setup methods (CPOA, TPA-single-cylinder, and TPA-multi-cylinder) are compared in terms of simulated LogP~LogV and cumulative burn fraction, at rated operating condition (2400 rpm, 543 ft-lbf). It is observed that, over the area where three methods all have simulated PV curve, the CPOA method and TPA-single-cylinder method are similar to each other, while the TPA-multi-cylinder method has a noticeably lower compression stroke than the others. Part of the reason is that since all the cylinders are simulated at the same time, they are inter-connected and thus inter-affected. Any discrepancies between the GT model and Test cell, especially the pipe geometries (affecting gas distribution) and test cell measurement uncertainties, will affect the estimation results for all of the cylinders. The calculated burn rate, however, is not very similar for all three methods at rated operating condition, with TPA-single-cylinder setup method slightly slower than the rest two methods.

As has been discussed, each method has its advantages and shortcomings:

- CPOA method, being the simplest setup, requires the least effort and budget, but need many presumptions to begin with, which, if unknown or inaccurate, can affect the estimation results very badly.

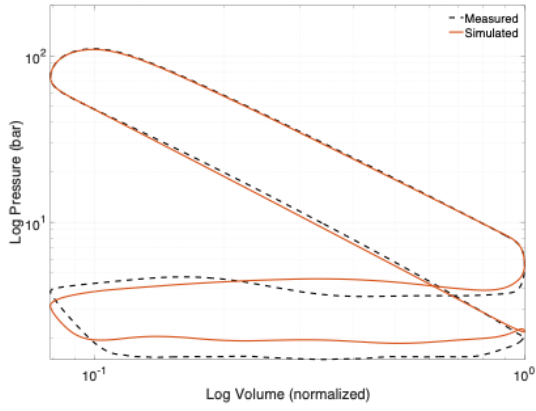


(a) LogP~LogV diagram: Simulated vs. Measured.

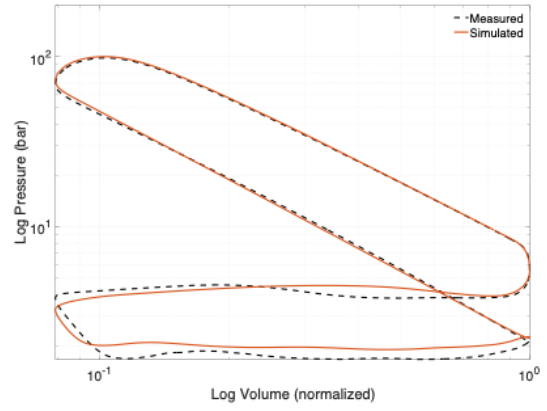


(b) Mass burn fraction.

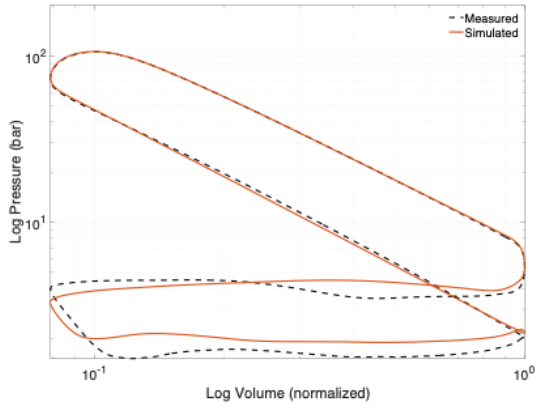
**Figure 3.10.** TPA multi cylinder at rated (2400rpm, 543 ft-lbf) - Cylinder #1.



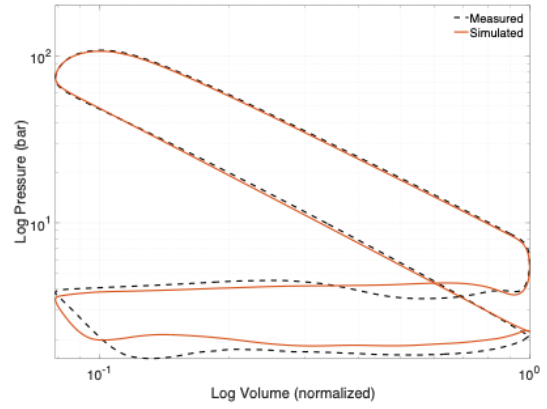
(a) Cylinder #1.



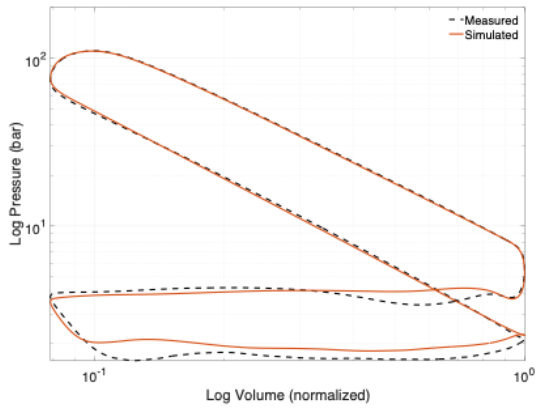
(b) Cylinder #2.



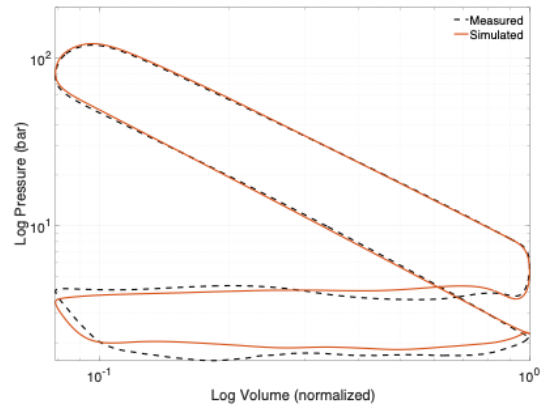
(c) Cylinder #3.



(d) Cylinder #4.



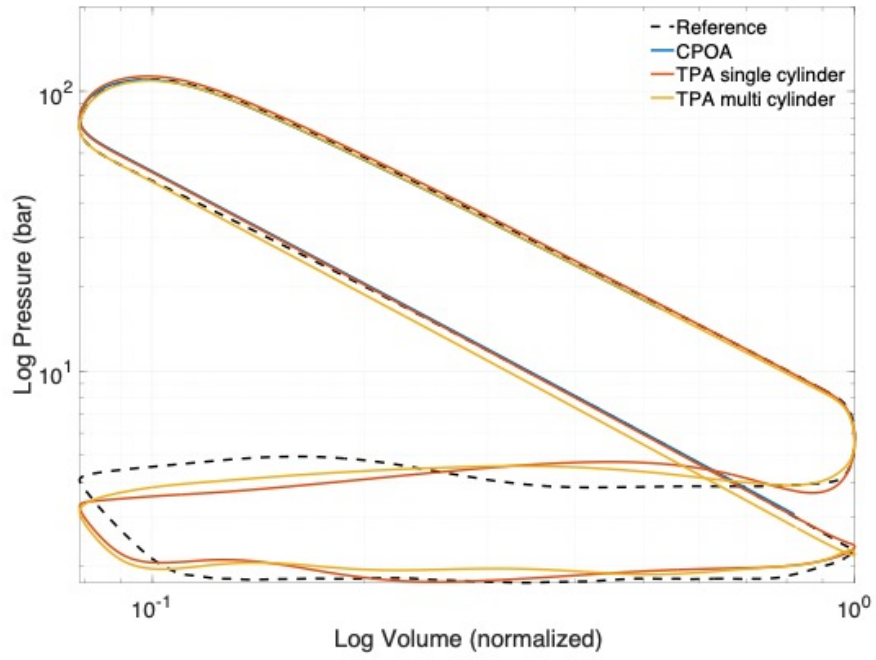
(e) Cylinder #5.



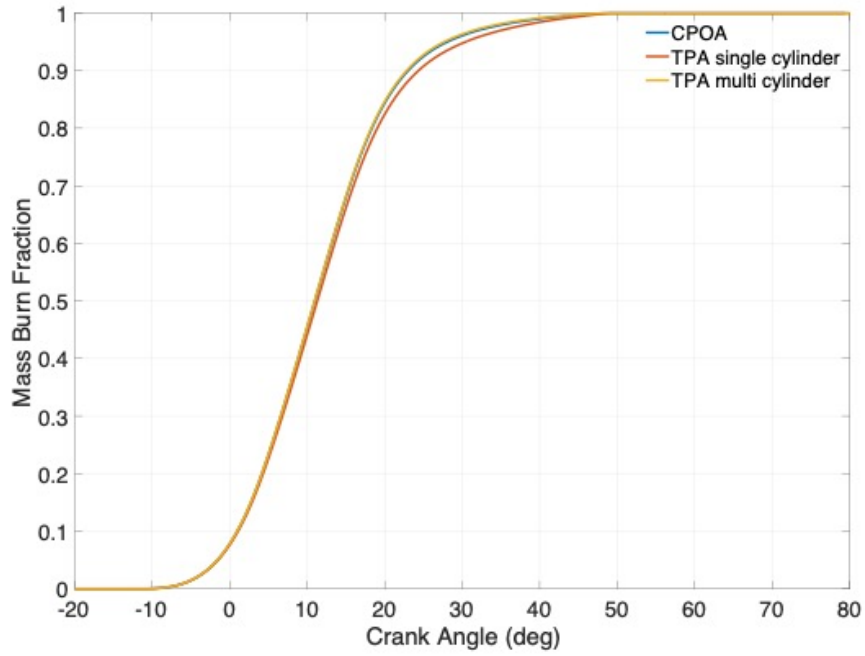
(f) Cylinder #6.

**Figure 3.11.** TPA multi cylinder at rated (2400rpm, 543 ft-lbf) - All cylinders.

- TPA-single-cylinder method, is simpler than TPA-multi-cylinder method and preferable if cylinder-to-cylinder difference is unnoticeable or not the priority. It needs more



(a) LogP~LogV diagrams.



(b) Mass burn fractions.

**Figure 3.12.** Comparison of different pressure analysis methods at rated (2400rpm, 543 ft-lbf) - Cylinder #1.



sensor implementations and operation information than CPOA but don't need as many presumptions. If the pressure measurement locations and pipe configuration are sorted through, it can render a very close estimation result.

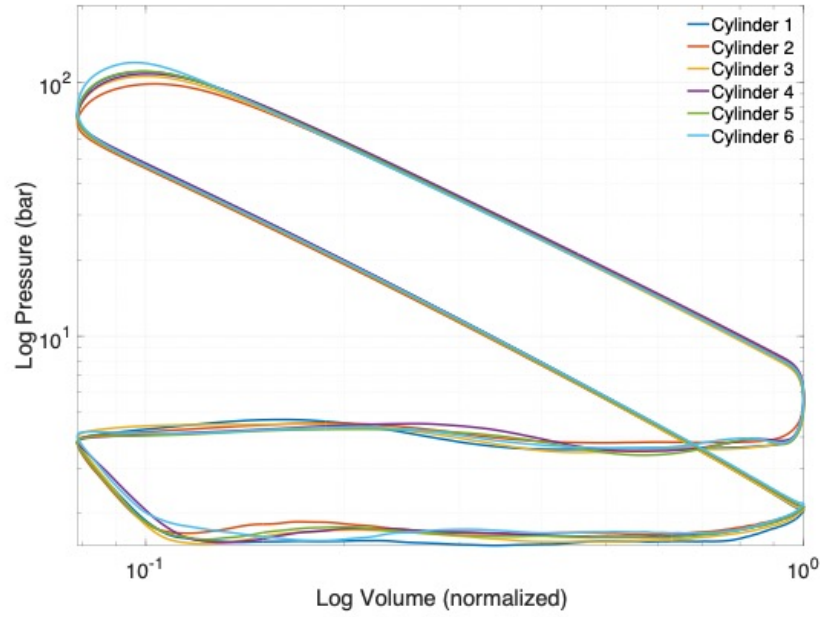
- TPA-multi-cylinder method, is the bulkiest and most expensive option of the three. However, if the GT model is already available and the need for pressure analysis is to update burn rate or develop predictive combustion model, it may not need structure/geometry modifications as with TPA-single-cylinder since it will keep the entire exhaust manifold unchanged. This setup is beneficial to calculate each cylinder's own burn rate, but the accuracy can be highly dependant on the model's accuracy, especially the pipe geometries.

#### 3.6.4 TPA multi-cylinder setup: Additional observations

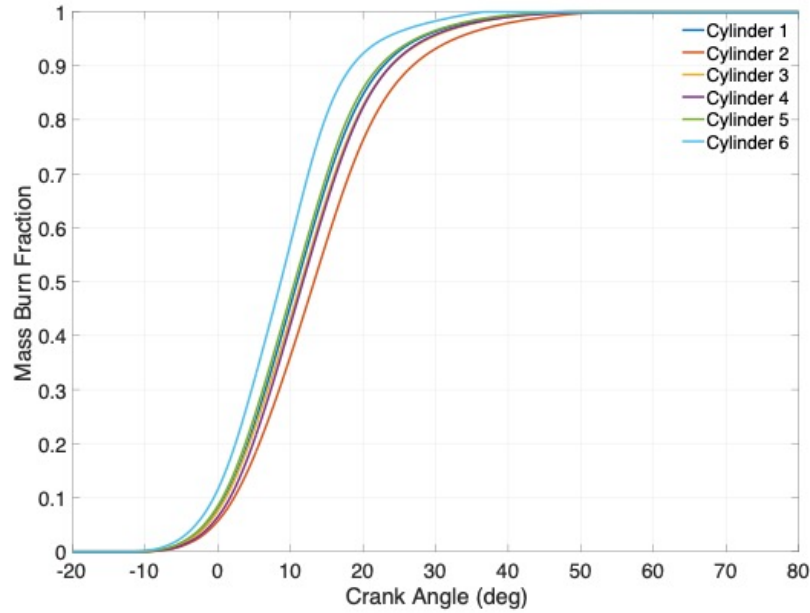
In this section, the TPA-multi-cylinder method is adopted to investigate and discuss some cylinder-to-cylinder and case-to-case comparisons. Fig. 3.13 presents the LogP~LogV diagrams and cumulative burn rates of all 6 cylinders at rated operation. To clarify, Fig. 3.13a only includes reference LogP~LogV diagrams for all six cylinders. The simulated LogP~LogV diagrams are not too different from each of its own reference diagram and is not relevant to the purpose of discussion in this section.

It is observed that all six cylinders' LogP~LogV diagram are different. Each cylinder's peak cylinder pressure, which is at the upper left of the curve, is also different cylinder-to-cylinder. In consequence, the calculated cumulative burn rate is also different cylinder-to-cylinder. Cylinders with higher peak cylinder pressure have a faster burn rate, such as cylinder #6 here.

Fig. 3.14 presents the LogP~LogV diagrams and cumulative burn rates of all 9 operating conditions (cases) of Cylinder #1. Each operating condition has its unique pressure curve, as is shown in Fig. 3.14a; while each operating condition also has its own burn rate profile, each differing from each other. The differences mainly come from two aspects - a higher engine load typically requires more and/or faster combustion, but a lower engine load may sometimes fully react even faster because of its small amount.



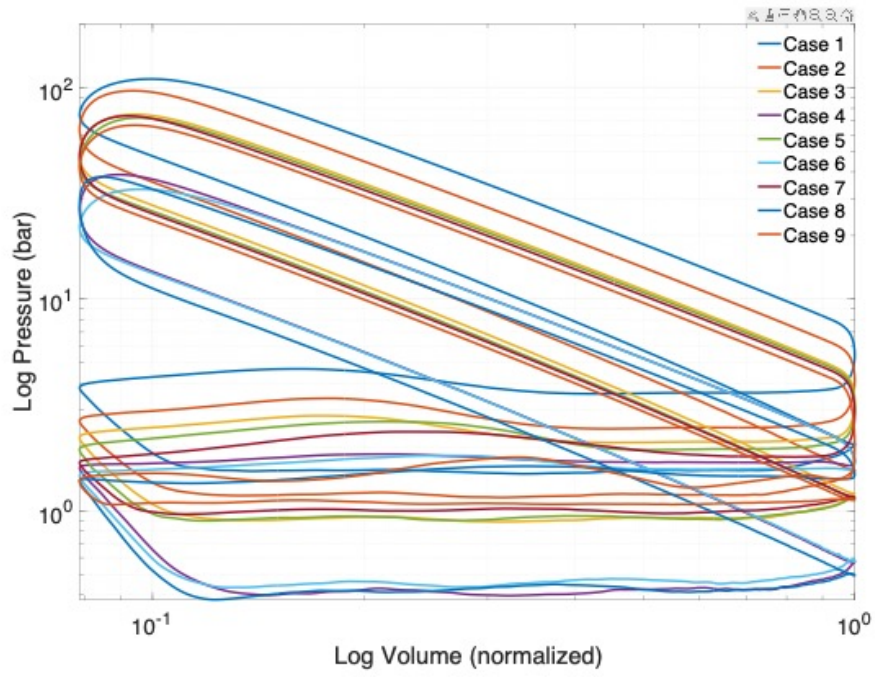
(a) LogP~LogV diagrams - Reference measurement.



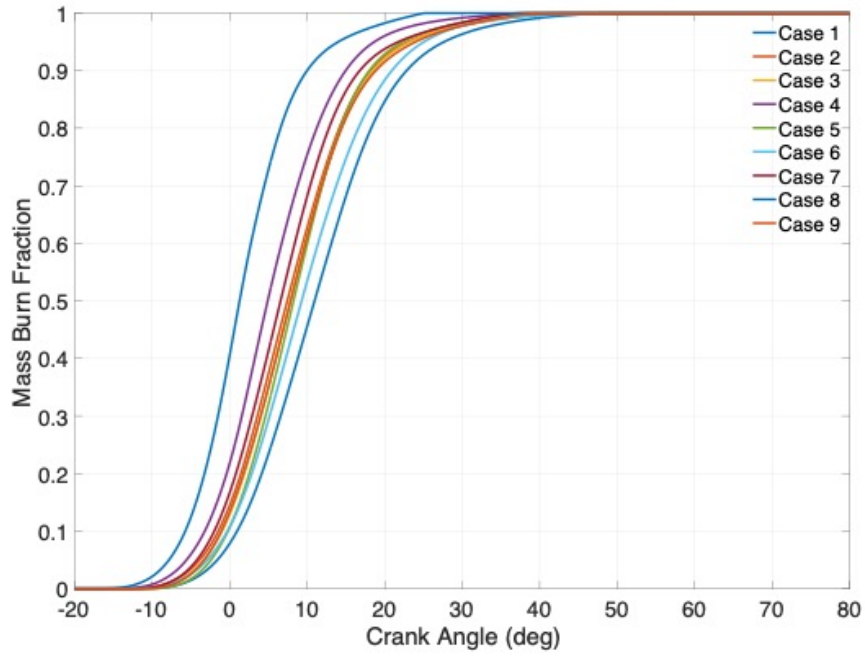
(b) Mass burn fractions.

**Figure 3.13.** Comparison of different cylinders using TPA multi cylinder method at rated (2400rpm, 543 ft-lbf).

Therefore, burn rate profile do vary cylinder-to-cylinder and operation-to-operation. To make the combustion model work for a larger range of loads, a fixed burn rate model may help in the preliminary research phase, but a predictive combustion model is more preferable.



(a) LogP~LogV diagrams - Reference measurement.



(b) Mass burn fractions.

**Figure 3.14.** Comparison using TPA multi cylinder method at different operations - Cylinder #1.

### 3.7 GT model calibration and comparison with test cell engine

After updating the burn profiles into the GT-Power model, a detailed checklist was used to calibrate and check the properties of the model against Cummins fuel map and test engine measurements, as is shown in Table 3.3. Some of the comparison results between GT model's and test cell's data will be presented and discussed in later sections.

**Table 3.3.** GT-Power model checklist.

Parameters	Descriptions
Engine Speed	Engine Crankshaft input, rpm
Brake Torque	Intake throttle valve control target, ft-lbf
Brake Power	kW
BSFC	Brake Specific Fuel Consumption, g/kW-hr
BMEP	Brake Mean Effective Pressure, bar
FMEP	Friction Mean Effective Pressure, bar
NIMEP	Net Indicated Mean Effective Pressure, bar
GIMEP	Gross Indicated Mean Effective Pressure, bar
PMEP	Pumping Mean Effective Pressure, bar
PCP	Average of Maximum Cylinder Pressures, bar
Mass Air Flow Rate	kg/hr
Mass Fuel Flow Rate	kg/hr
AFR	Air-Fuel Ratio, Fuel Injector control target
EGR Fraction	EGR valve control target
Intake Manifold Pressure	bar
Compressor Inlet Pressure	Boundary condition, bar
Compressor Outlet Pressure	Wastegate Valve control target, bar
Turbine Inlet Pressure	bar
Turbine Outlet Pressure	Boundary condition, bar
Intake Manifold Temperature	deg K
Compressor Inlet Temperature	Boundary condition, deg K
Compressor Outlet Temperature	deg K
Turbine Inlet Temperature	deg K
Turbine Outlet Temperature	Boundary condition, deg K
Vol. Eff	Volumetric Efficiency
OCE	Open Cycle Efficiency
CCE	Closed Cycle Efficiency
ME	Mechanical Efficiency
BTE	Brake Thermal Efficiency

### 3.7.1 Operating condition, pressures, and temperatures

Each time before the GT model is run, there are some parameters that need being setup, including:

- The Engine Speed Target to the engine crankshaft.
- The Brake Torque Target to the intake throttle valve.
- EGR Fraction Target to the EGR valve.
- Compressor Outlet Pressure Target to the turbine wastegate valve.
- AFR Target to the fuel injector.
- Turbine Outlet Pressure & Temperature boundary condition.
- Compressor Inlet Pressure & Temperature boundary condition.

The GT-Power model was calibrated and compared with Test cell data at all the nine operating points in Table 3.2. Fig. 3.15 and Fig. 3.16 show the operating condition comparison, i.e., Engine Speed and Brake Torque. It is coherently setup in the following figures that, the X axis refers to the parameter value from Test cell measurement/ calculation, either from dSPACE, Calterm, or Indicom system; While the Y axis refers to the parameter value taken or calculated from GT-Power. Three reference lines - one to one reference line, +5% error line, and -5% error line - are included for clearer comparison between the GT-Power simulation result with respect to Test cell captured data. Both the Speed and Torque data are well within the  $\pm 5\%$  error lines. It also indicates a matching Brake Mean Effective Pressure (BMEP) between GT model and Test cell since the BMEP is directly related to Brake Torque.

Fig. 3.17 and Fig. 3.18 show the gas flow rate comparisons. Most fuel flow rates are within the  $\pm 5\%$  lines, while most air flow rates are past -5% error line and within -10% error line. It is worth noting that the current setup includes two sets of air and fuel flow rate, both from dSPACE system and Calterm system. The Calterm system, as mentioned before,

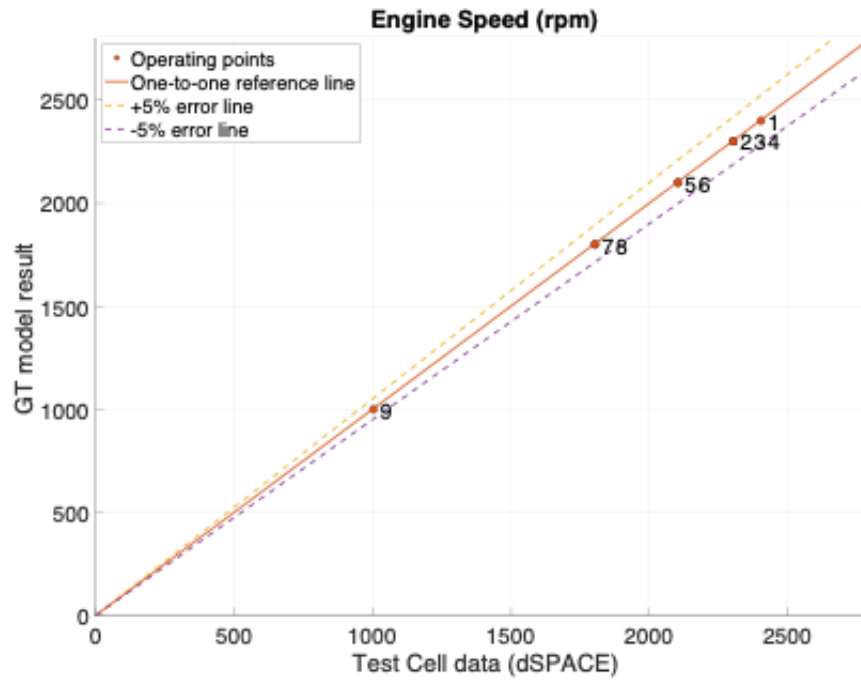


**Figure 3.15.** Engine speed: GT Model vs. Test Cell.

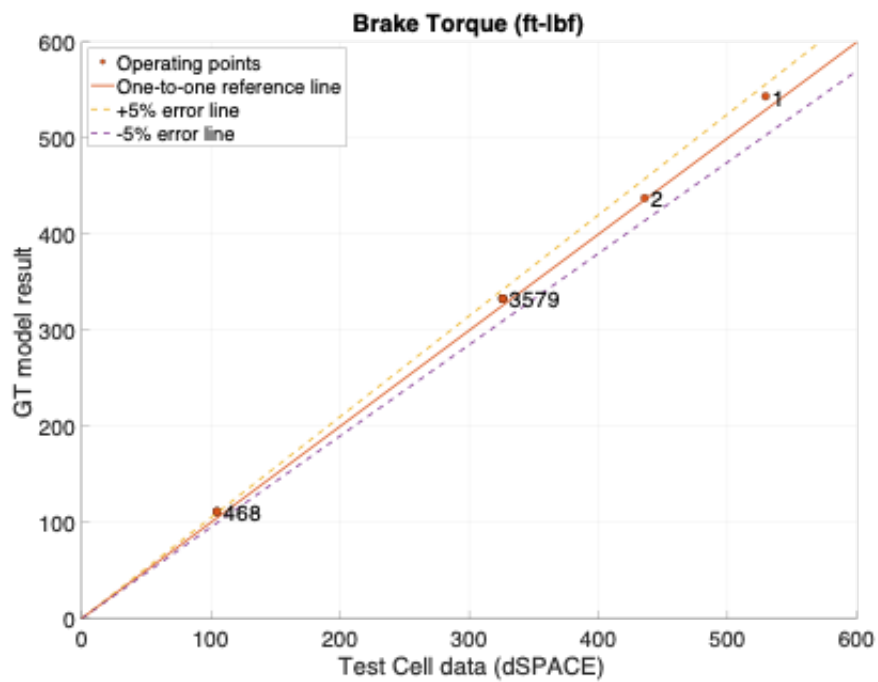


**Figure 3.16.** Brake torque: GT Model vs. Test Cell.

drives the engine control module to send commands to cylinders, while the dSPACE system integrates most of the measurement devices post-installed in Test cell. The flow rate data from dSPACE comes from a more accurate sensor set, but the Calterm system is inside the engine control loop and thus affects the engine performance. Therefore, even though the boundary conditions have been checked and fixed based on Cummins fuel map, the flow rate measurement from test cell is slightly different from fuel map's data. However, the overall engine performance was not as affected since the amount of fuel put into the system was very close (thus similar level of power resource), and the engine delivered the commanded Engine Speed and Brake Torque within acceptable error range.

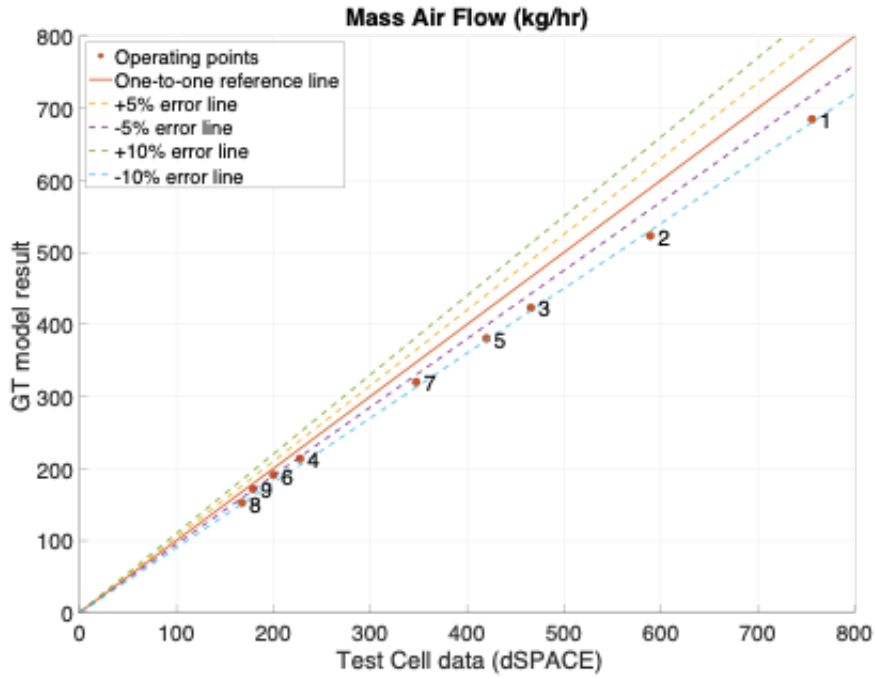


**Figure 3.17.** Mass air flow: GT Model vs. Test Cell.

Brake Specific Fuel Consumption (BSFC) is a measure of the fuel efficiency of the engine at producing power to the crankshaft. It is the rate of fuel consumption divided by the generated brake power. It is expressed as:

$$BSFC = \frac{\dot{m}_{Fuel}}{P_{brake}} \quad (3.2)$$

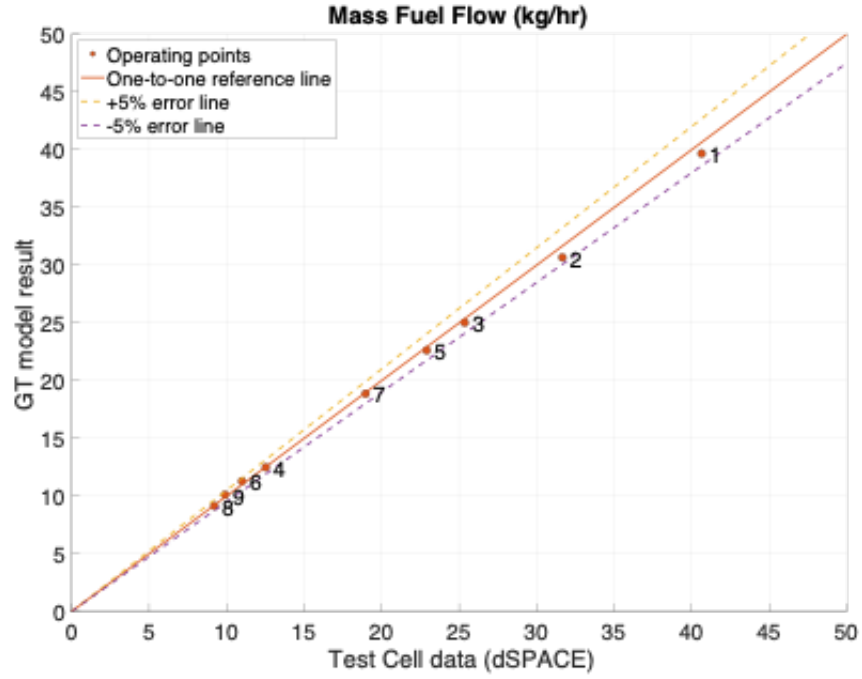


**Figure 3.18.** Mass fuel flow: GT Model vs. Test Cell.

Where  $\dot{m}_{Fuel}$  is the mass fuel flow rate, and  $P_{brake}$  is the output brake power. The BSFC is shown in Fig. 3.19. It is directly related to the brake torque, engine speed, and mass fuel flow rate, and is thus also mostly within the  $\pm 5\%$  error lines.

The pressures and temperatures of various locations were also checked for GT model calibration. Most of the exchanges between the engine system to the outside happen within the turbocharger module - the compressor takes in fresh air from environment, and the turbine expels a (large) portion of exhaust gas to the after-treatment system. The boundary condition at compressor outlet is set at atmosphere. As for the turbine outlet, since the investigated GT-Power model doesn't include an after-treatment module (neither does the test cell), boundary pressure and temperature was set for each operating point based on Cummins fuel map.

The gas properties entering and exiting the engine block include intake manifold pressure & temperature, cylinder pressures, as well as exhaust manifold pressure & temperature. Intake manifold measurement is taken right before the intake pipe splits to 6 cylinders. From



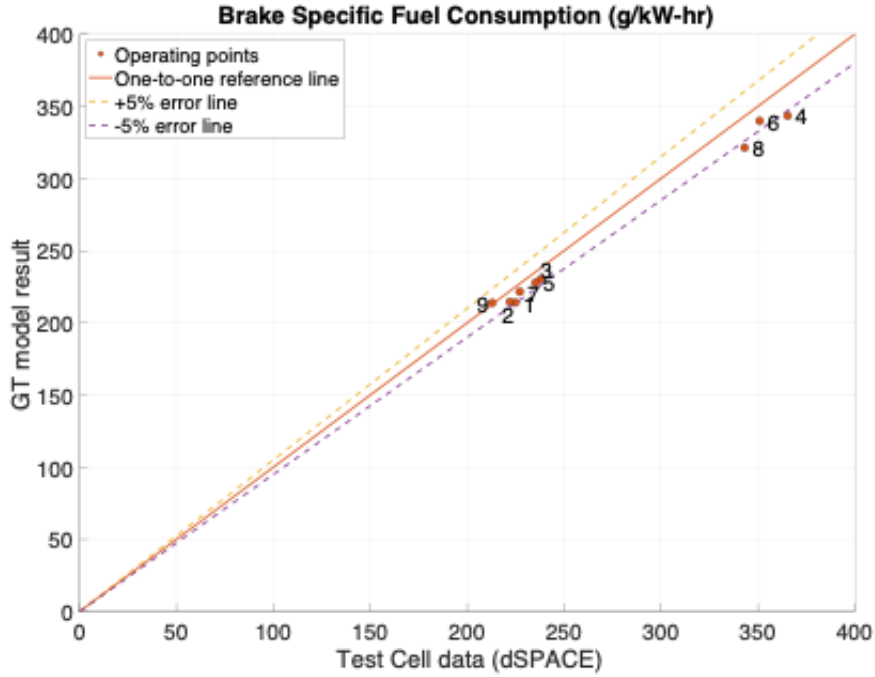


**Figure 3.19.** Brake specific fuel consumption: GT Model vs. Test Cell.

Fig. 3.20 and Fig. 3.21, both the intake manifold pressures and intake manifold temperatures are mostly within the  $\pm 5\%$  error lines.

As was mentioned in previous, every cylinder pressure was measured independently in Test cell and available in Indicom system. Fig. 3.22 shows the comparison plot for the average of the peak cylinder pressures for all 6 cylinders. The data points are mostly below  $+5\%$  error line with a few exceptions slightly beyond  $+5\%$  error range. This could be caused by a slightly more aggressive combustion than real test cell.

Due to the complexity inside the exhaust manifold (splitting gases to turbine and EGR) more practical (and common) approach is adopted to check the pressure and temperature near the turbine inlet. From Fig. 3.23 and Fig. 3.24, the turbine inlet (exhaust manifold) pressures are mostly within the  $\pm 5\%$  error lines, while some of the turbine inlet temperatures falls within  $5\% \sim 10\%$  error range. All the temperatures are higher than measured turbine temperature, which could be due to some heat transfer discrepancy between the GT model and Test cell.

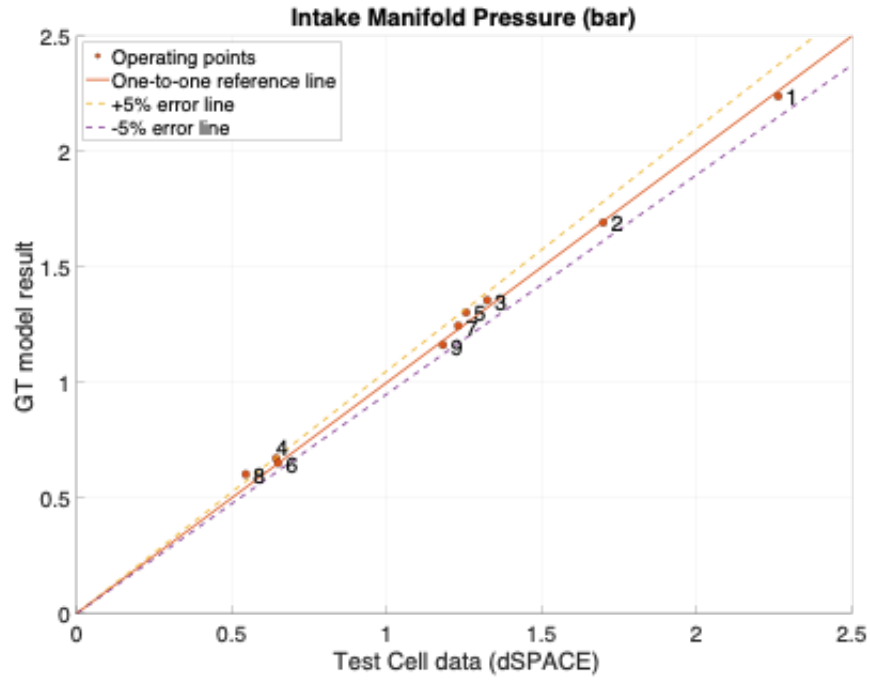


Figure 3.20. Intake manifold pressure: GT Model vs. Test Cell.

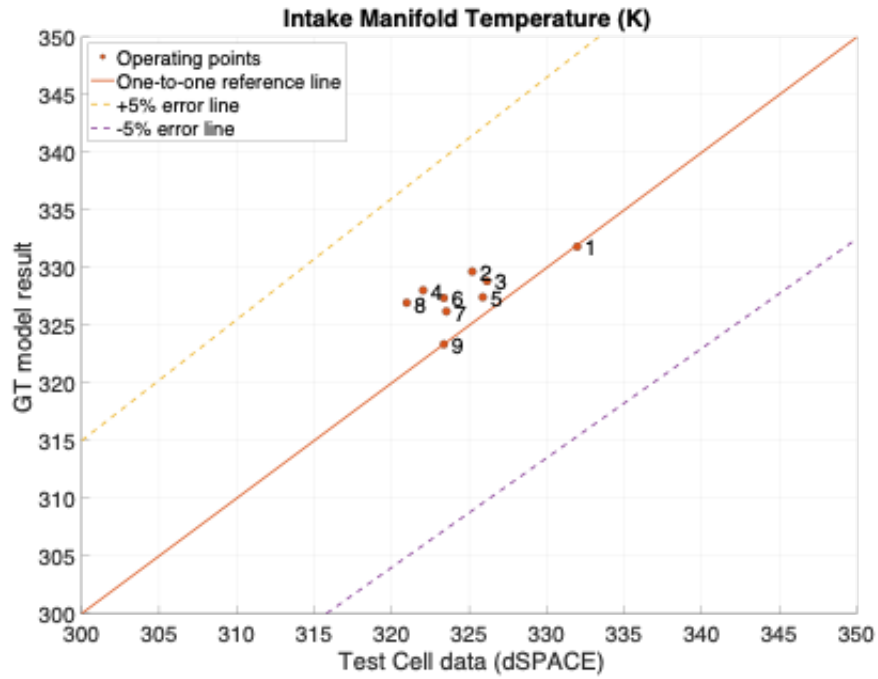


Figure 3.21. Intake manifold temperature: GT Model vs. Test Cell.

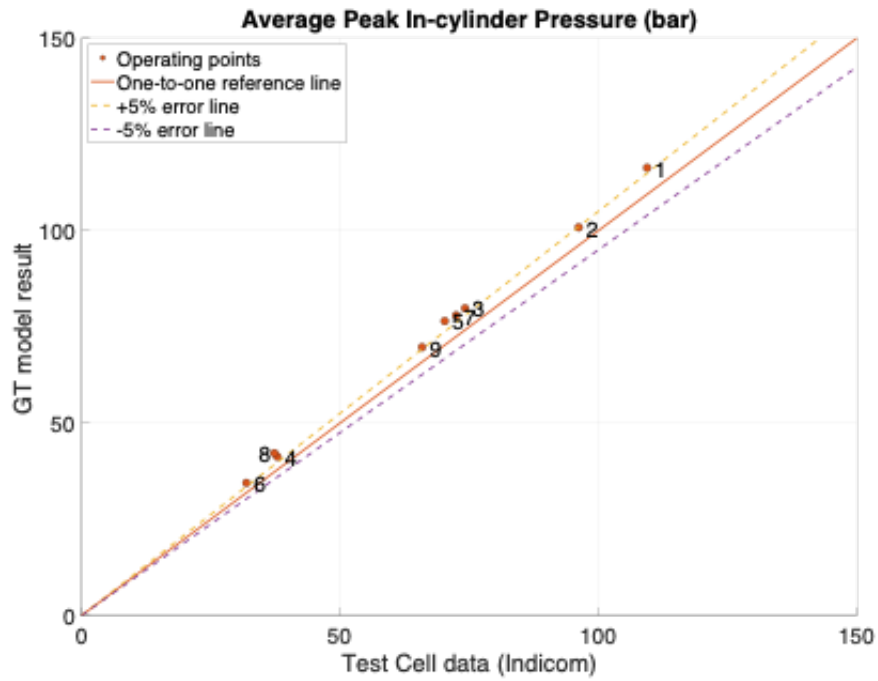


Figure 3.22. Average peak in-cylinder pressure: GT Model vs. Test Cell.

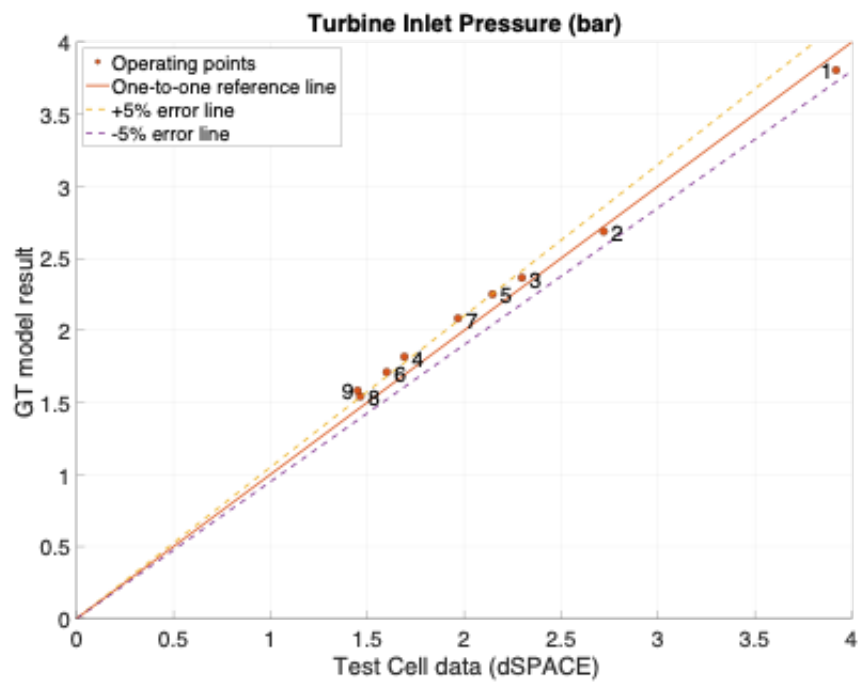
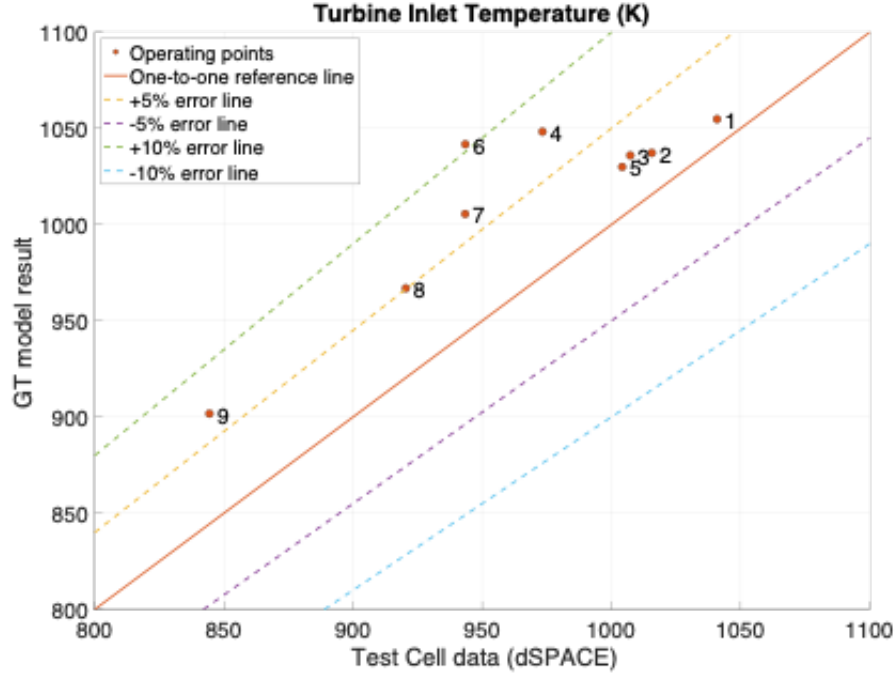


Figure 3.23. Turbine inlet pressure: GT Model vs. Test Cell.



**Figure 3.24.** Turbine inlet temperature: GT Model vs. Test Cell.

### 3.7.2 Engine efficiencies and mean effective pressures

Engine efficiencies are important factors in four stroke internal combustion engine evaluation, and has been researched and developed in decades for improvements. Most of the energy generated from engine combustion is not converted into useful work to the crankshaft, but lost (dissipated) instead, mostly through heat transfer, gas pumping and friction. For a typical engine, only a third of the combustion power (at full load) ends up as brake power, and the situation can be worse at part load, where overall engine efficiency drop to the range of 20%. The overall efficiency is commonly called the brake thermal efficiency (BTE) of the engine, with equation below.

$$\eta_{thermal} = \frac{P_{brake}}{\dot{m}_{Fuel} \times Q_{lhv}} \quad (3.3)$$

Where  $Q_{lhv}$  is the lower heating value of the fuel. The BTE can also be expressed as:

$$\eta_{thermal} = \eta_{open} \times \eta_{closed} \times \eta_{mechanical} \quad (3.4)$$

where  $\eta_{closed}$ ,  $\eta_{open}$ , and  $\eta_{mechanical}$  are the closed cycle efficiency (CCE), open cycle efficiency (OCE), and mechanical efficiency (ME), respectively. In Fig. 3.25, a LogP~LogV diagram from one cylinder in the GT model is used to demonstrate for a four stroke SI engine combustion cycle.

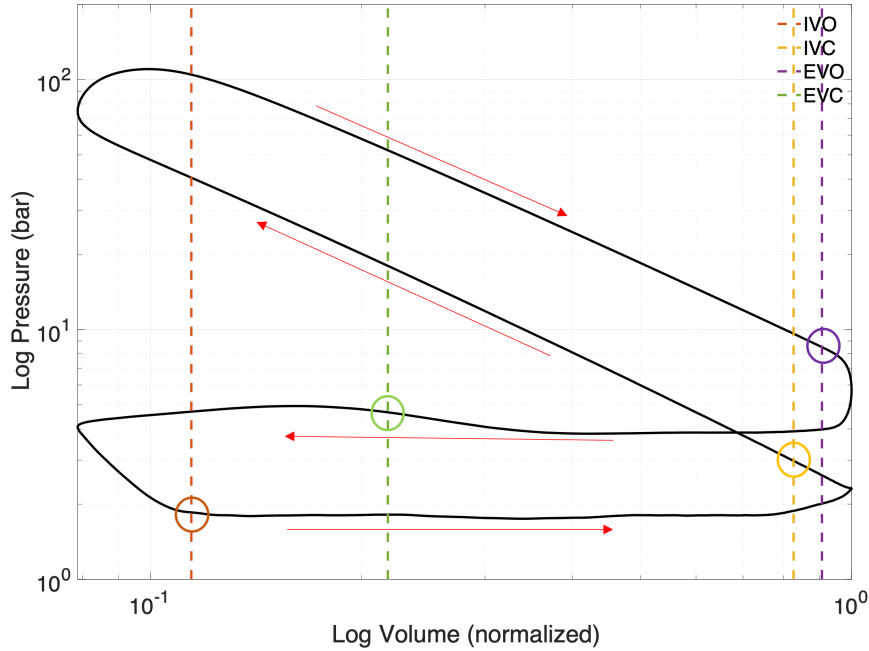


**Figure 3.25.** LogP ~LogV diagram demonstration.

Closed cycle efficiency is a measure of combustion efficiency of the engine, with "closed cycle" referring to the time period when both intake and exhaust valves are closed. It is the ratio of (gross) generated combustion power to the entire power resources throughout the cycle (most of which, as mentioned previously, were dissipated through heat transfer). The gross power refers to the work done in the upper loop of PV cycle, which can also be called power loop. It is expressed as

$$\eta_{closed} = \frac{P_{gross}}{\dot{m}_{Fuel} \times Q_{lhv}} \quad (3.5)$$

Fig. 3.26 shows the closed cycle efficiency comparison. All GT model's closed cycle efficiency are higher than test cell data but still within +5% error line, which means GT

model has a slightly better power generation. It could be due to multiple factors, including fuel property, inter-cylinder burn rate discrepancy, fuel flow rate, etc.

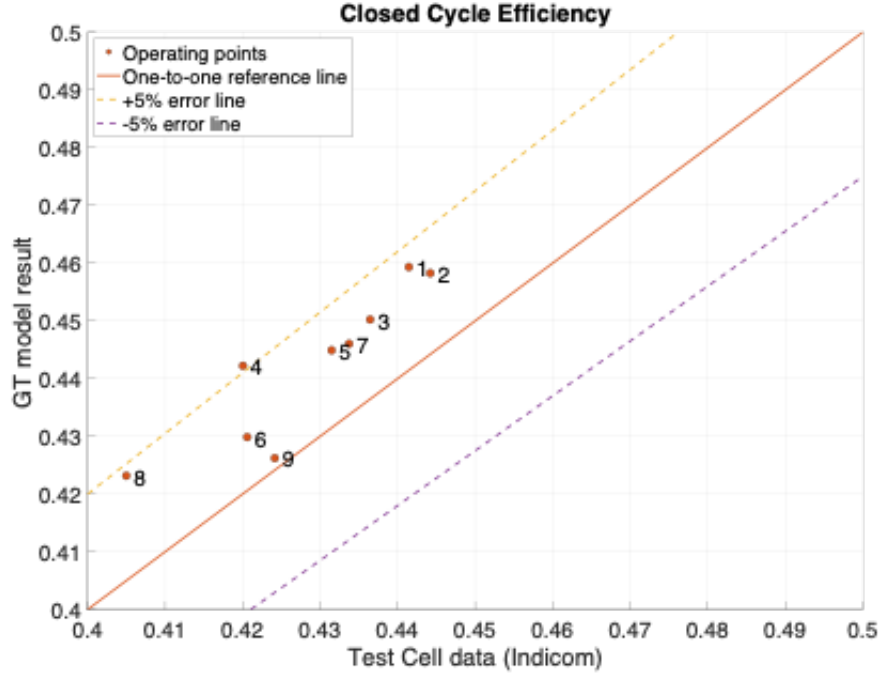


**Figure 3.26.** Closed cycle efficiency: GT Model vs. Test Cell.

For each cycle of combustion, a certain amount of power is required for the pumping of gases in and out of the cylinder. Therefore, the net power output consists of two parts, (gross) combustion power output and pumping work (typically negative because exhaust pressure is higher than intake pressure). The relation is expressed as:

$$P_{net} = P_{gross} + P_{pumping} \quad (3.6)$$

Where the pumping power refers to the work done in the lower loop of PV cycle, which can also be called pumping loop, and the work is typically negative. The open cycle efficiency thus measures the ability of pumping gases, with "open cycle" meaning the time period where both intake and exhaust valves are open.

$$\eta_{open} = \frac{P_{net}}{P_{gross}} \quad (3.7)$$

Fig. 3.27 shows the open cycle efficiency comparison. The GT model and test cell are highly similar to each other. Since open cycle efficiency is directly related to the pumping loop and power loop work, it also indicates that the GT model's PV cycle is in general matching the test cell.

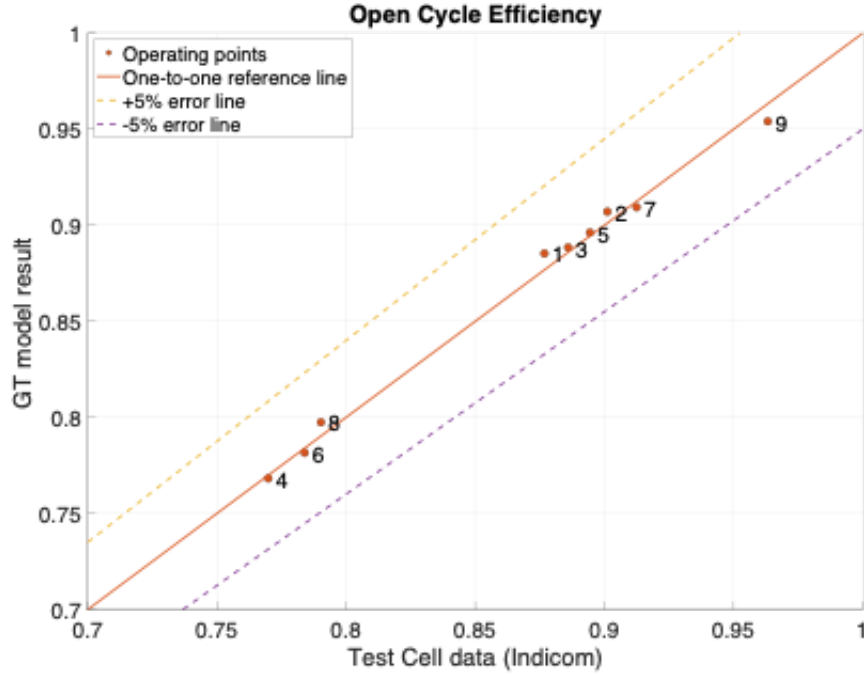


**Figure 3.27.** Open cycle efficiency: GT Model vs. Test Cell

During the combustion process, a portion of (net) power is used to overcome the friction of bearings, pistons, and other mechanical components of the engine, and to drive essential engine accessories. In other words, the net power output consists of two parts, the brake (useful) power and the friction power, i.e.,

$$P_{net} = P_{brake} + P_{friction} \quad (3.8)$$

The ratio of the brake power delivered by the engine to the net indicated power is called mechanical efficiency, which is expressed as

$$\eta_{mechanical} = \frac{P_{brake}}{P_{net}} \quad (3.9)$$

Fig. 3.27 shows the mechanical efficiency comparison., and the GT model and test cell are highly similar to each other at mechanical efficiency too. The engine friction model is interpolated from Cummins fuel map which leads to a close estimated friction power, and the brake power is also proven coherent with test cell previously. Therefore, the net power (in the denominator) is also coherent.

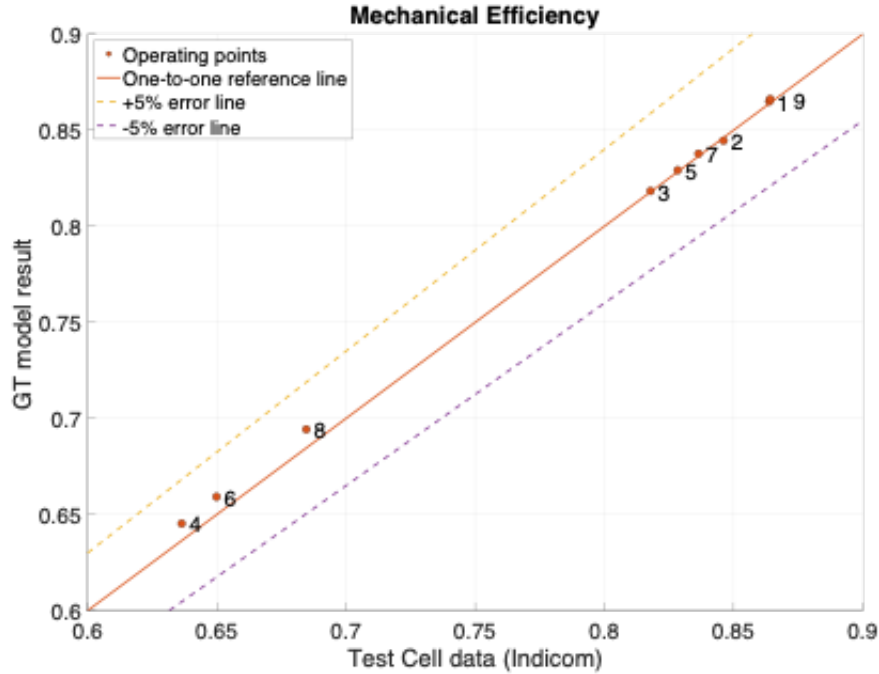


**Figure 3.28.** Mechanical efficiency: GT Model vs. Test Cell.

With all three efficiencies available, the brake thermal efficiency is then compared in Fig. 3.29. Most of the cases are within  $\pm 5\%$  error lines, and most of the errors came from closed cycle efficiencies, i.e., fuel thermal discrepancies.

While brake torque is one of the most direct measures of an engine's ability to do work, its actual effect also depends on engine size. Therefore, some useful relative engine performance measures are used and obtained by dividing the work per cycle by the cylinder volume displaced per cycle, i.e., the mean effective pressures.

- Brake mean effective pressure, BMEP, is the mean effective pressure of the brake power output.



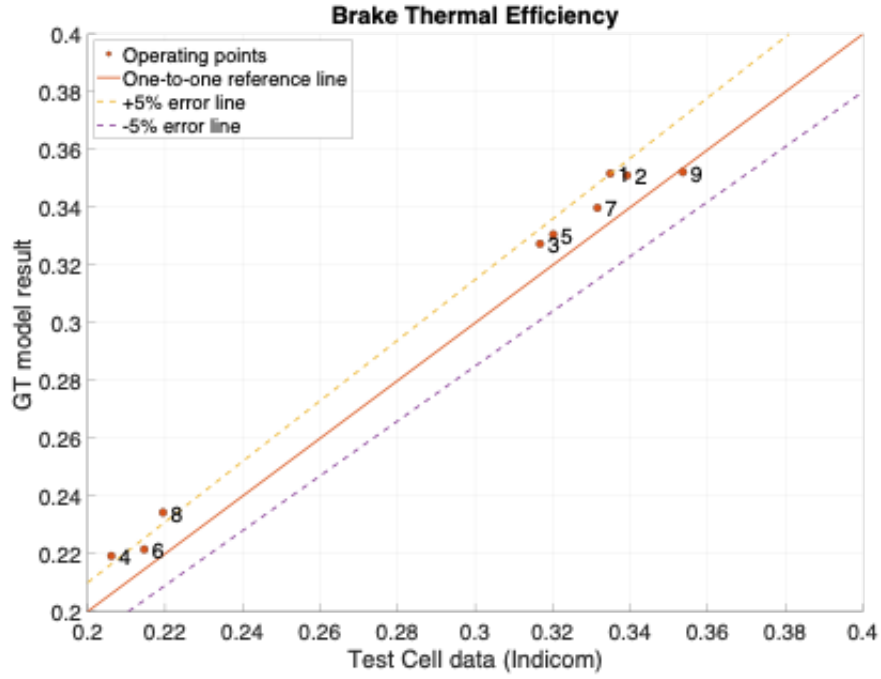


**Figure 3.29.** Brake thermal efficiency: GT Model vs. Test Cell.

- Friction mean effective pressure, FMEP, is the mean effective pressure due to friction losses (friction power).
- Net indicated mean effective pressure, NIMEP, is the mean effective pressure of the cycle net power output.
- Gross indicated mean effective pressure, GIMEP, is the mean effective pressure of the gross combustion power output, i.e., the power loop.
- Pumping mean effective pressure, PMEP, is the mean effective pressure of the pumping losses, i.e., the pumping loop.

Based on the PV cycle (Fig. 3.25), the mean effective pressures can be expressed as:

$$\begin{aligned}
 GIMEP &= \frac{Area_{ClosedLoop}}{V_d} \\
 PMEP &= \frac{Area_{OpenLoop}}{V_d} \\
 NIMEP &= GIMEP + PMEP
 \end{aligned} \tag{3.10}$$

Where,  $V_d$  is the engine volumetric displacement. Brake mean effective pressure is close related to the engine brake torque, and the comparison follows the same trend as the brake torque comparison.

$$BMEP = \frac{2\pi \times n_{RevolutionsPerCycle} \times Torque}{V_d} \quad (3.11)$$

And the friction mean effective pressure can be calculated by:

$$FMEP = NIMEP - BMEP \quad (3.12)$$

Figures below (Fig. 3.32, 3.31, 4.10c, 3.30) shows the comparisons on the gross indicated mean effective pressure, the absolute pumping mean effective pressure, the net indicated mean effective pressure, and the friction mean effective pressure. All four mean effective pressures from GT model agree with test cell's Indicom calculation, being within  $\pm 5\%$  error range.

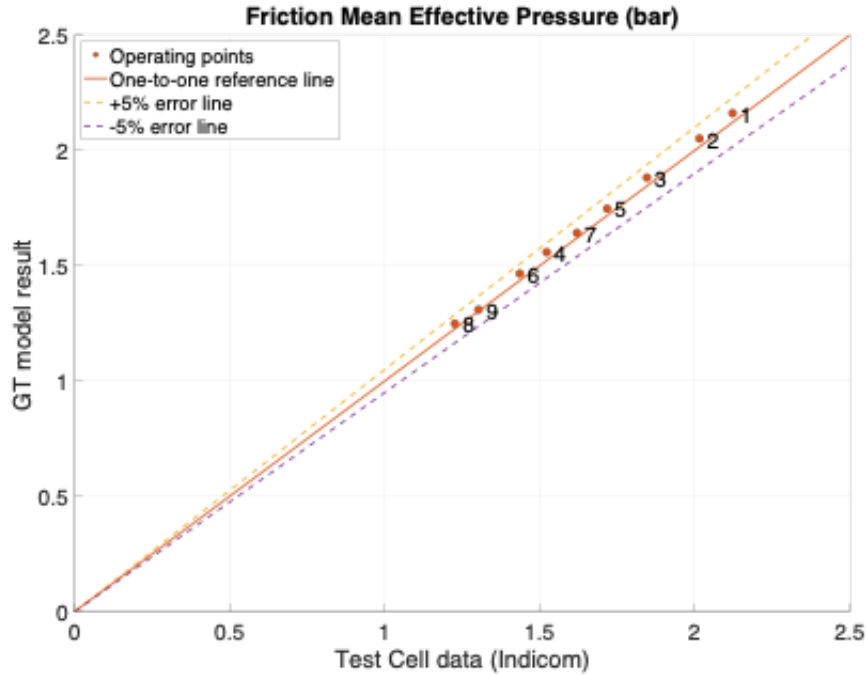


**Figure 3.30.** Friction mean effective pressure: GT Model vs. Test Cell.

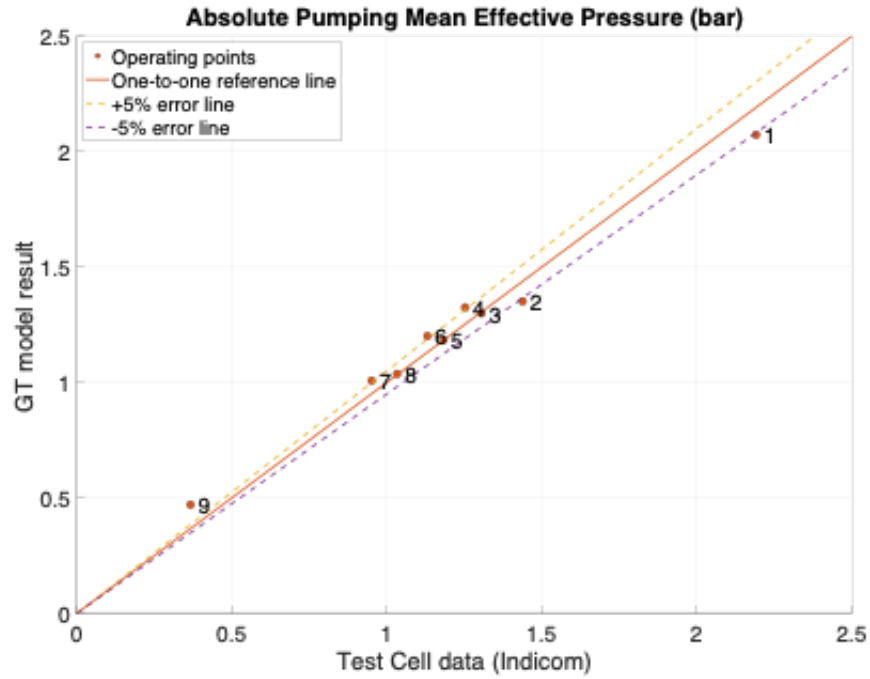


**Figure 3.31.** Absolute pumping mean effective pressure: GT Model vs. Test Cell.

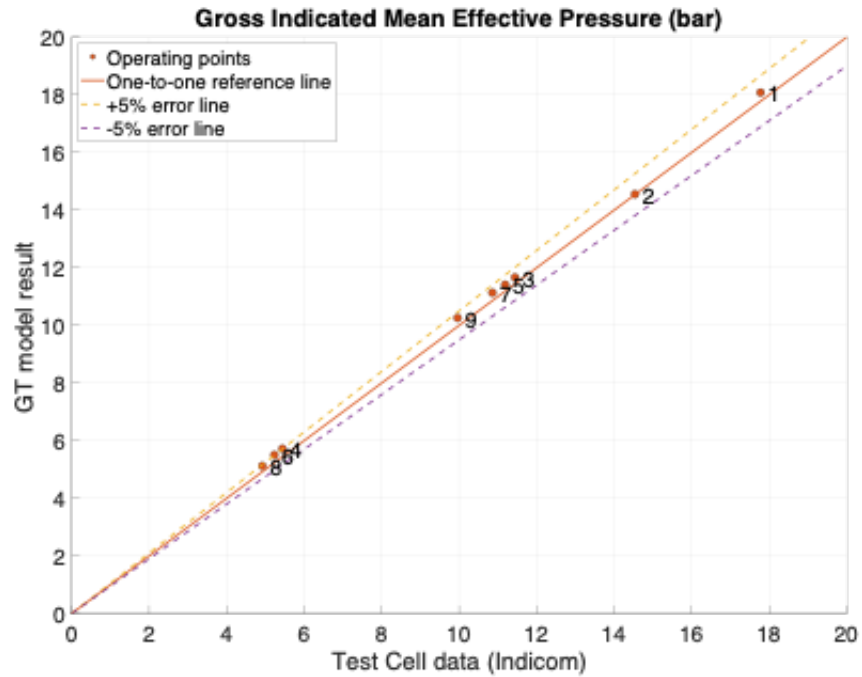


**Figure 3.32.** Gross indicated mean effective pressure: GT Model vs. Test Cell.

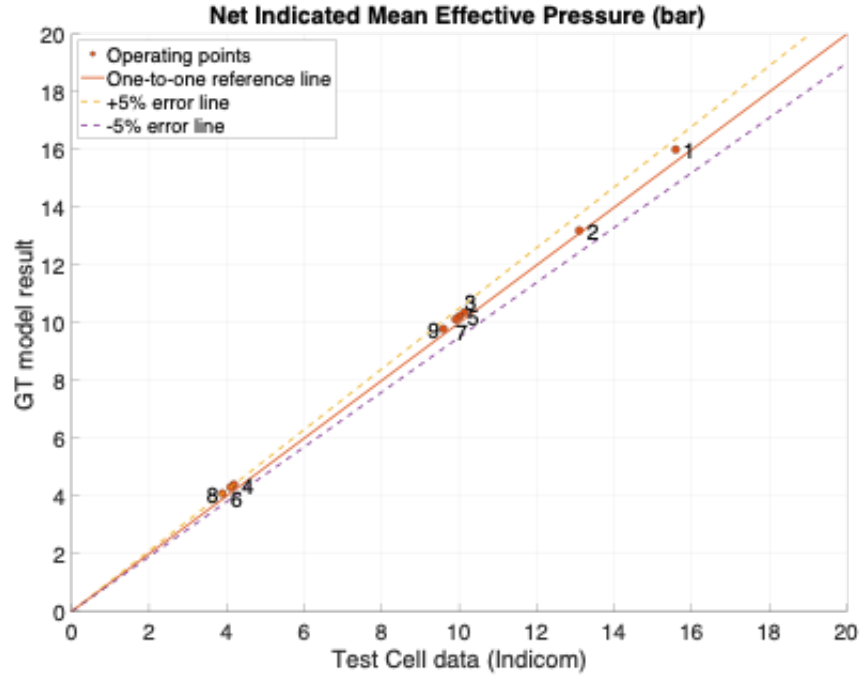


**Figure 3.33.** Net indicated mean effective pressure: GT Model vs. Test Cell.

It is also worth noting that the engine efficiencies and mean effective pressures are so correlated that the engine efficiencies can also be calculated from mean effective pressures as follows:

$$\begin{aligned}
 \eta_{closed} &= \frac{GIMEP \times V_d}{\dot{m}_{Fuel} \times Q_{lhv}} \\
 \eta_{open} &= \frac{NIMEP}{GIMEP} = 1 + \frac{PMEP}{GIMEP} \\
 \eta_{mechanical} &= \frac{BMEP}{NIMEP} = \frac{PMEP}{NIMEP + FMEP}
 \end{aligned} \tag{3.13}$$

## 4. NATURAL GAS VARIABLE VALVE ACTUATION

### 4.1 Variable Valve Actuation Technology

Variable valve actuation (VVA), is a general term that can be used to describe a range of technologies which are used to add flexibility to the engine's valve train by enabling variable valve event timing, duration and/or lift. This includes but is not limited to late/early opening/ closing of cylinder valves as well as cylinder deactivation (CDA). It has been broadly studied for internal combustion engine development [19] [20] and has plenty of potential for improvement and with alternative fuel types.

A VVA standalone system is available in the test cell, as is shown in Fig. 4.1. The system consists of 12 full flexible cam-less valve actuator which allows full control of valve events for the engine experiment. Each of the actuators connects to 2 valves, either the intake pair or the exhaust pair, and drives the linear electro-hydraulic servo valve for the vertical lifting of the valve pair. The VVA system was used for researches on Cummins Diesel 6.7L engine. It was modified with spark plugs due to the engine change from compression ignition to spark ignition, and tested and tuned for valve lifting controls.

After the Cummins stock engine was tested and compared with Cummins fuel map at rated operation, the engine head was taken out and the VVA system was then mounted. The completed installation is shown in Fig. 4.2. The upper light-colored part came from the VVA standalone system (Fig. 4.1).

### 4.2 Intake Valve Closure Modulation

The stock engine (without VVA modification) adopts the same valve lift profiles for all intake valves and all exhaust valves, respectively. In Fig. 4.3, the blue curve represents the exhaust valve lift profile, and the red curve represents the intake valve lift profile. The dashed black line represents the distance between the piston head's flat surface and the engine's top dead center. Neither the blue line nor the red line can cross the dashed black line, otherwise the piston head can collide with the valves during the crossing. Therefore, there are six possible variations on the valve lift profile - early exhaust valve opening, late exhaust valve



**Figure 4.1.** VVA standalone system in test cell.

opening, early exhaust valve closing, late intake valve opening, early intake valve closing, and late intake valve closing.

In spark-ignited engines, the pumping losses are higher at low engine speeds due to the presence of intake throttle valve. Intake valve closure (IVC) modulation can be helpful in addressing the pumping losses at part loads. Change on IVC can change the volumetric efficiency, and a lower volumetric efficiency can allow the engine to operate with higher intake manifold pressures while maintaining stoichiometry, which reduces the pumping work by bringing the pressures in the intake and exhaust manifold closer together. A demonstration plot of IVC modulation is shown in Fig. 4.4, where the purple dashed line is Early IVC and the green dashed line is Late IVC.

Intake valve closure happens between the end of intake stroke and start of combustion. An early intake valve closure can result in more stable combustion, longer flame development



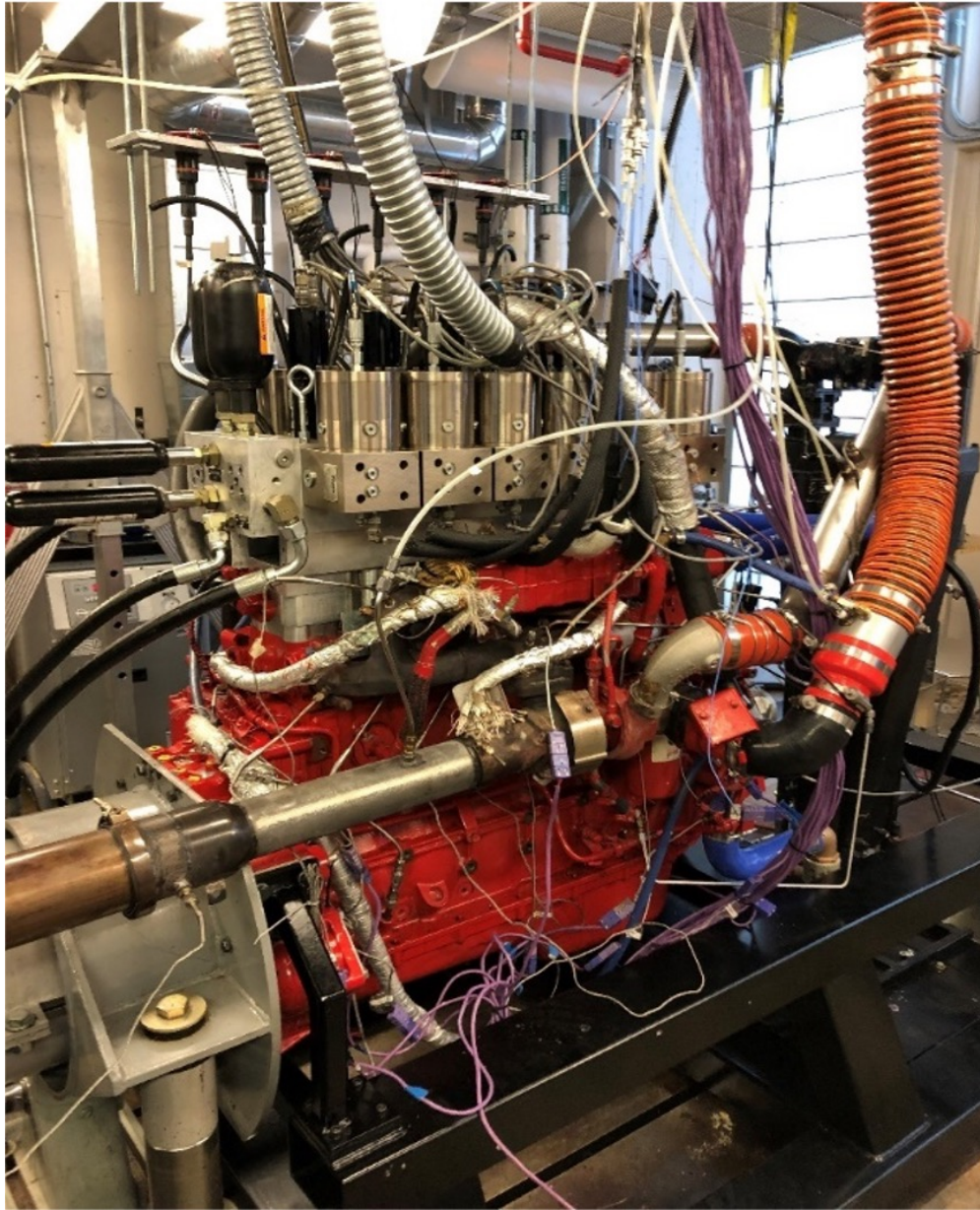


**Figure 4.2.** VVA installation on engine in test cell.

period, while a late intake valve closure helps in significant reduction in pumping losses at partial load. Five operating points at low torque range were run under IVC modulation.

800rpm, 111ft-lbf    1000rpm, 111ft-lbf    1300rpm, 111ft-lbf  
1600rpm, 111ft-lbf    1800rpm, 111ft-lbf

The IVC modulation timings include:

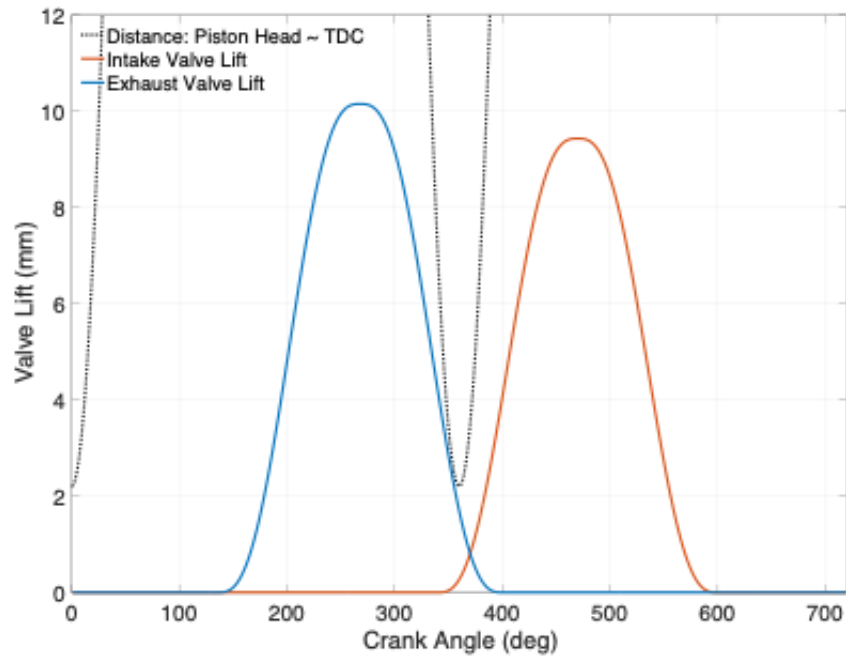


**Figure 4.3.** Intake & Exhaust valve lift profiles.

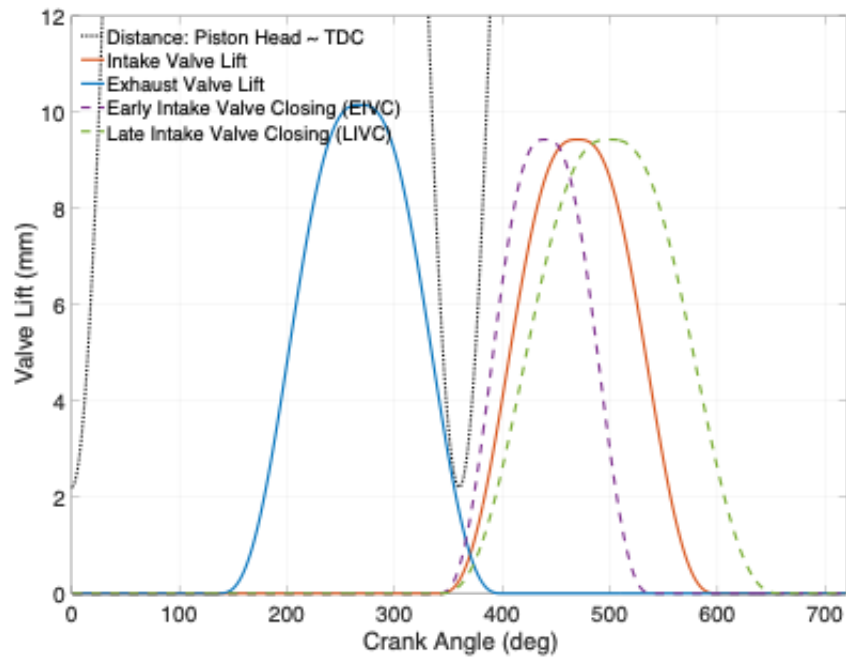
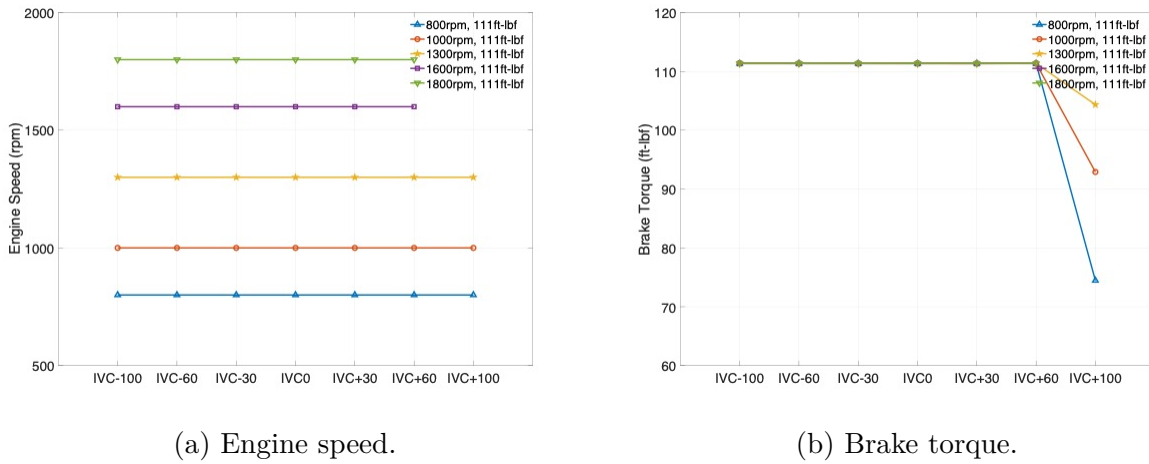


**Figure 4.4.** Early & Late intake valve closure (IVC).



IVC-100CAD   IVC-60CAD   IVC-30CAD   Stock IVC  
 IVC+30CAD   IVC+60CAD   IVC+100CAD

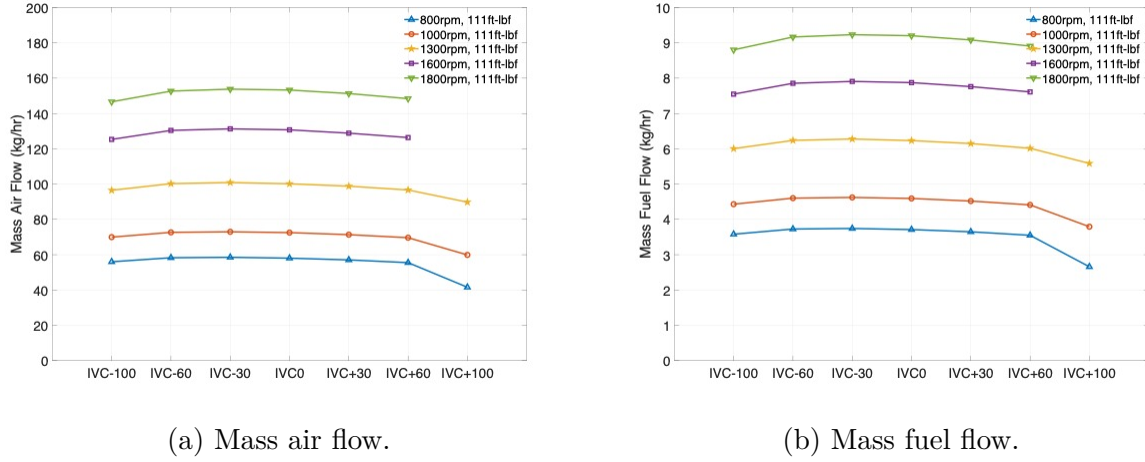
The engine operating conditions (speeds and torques) under IVC modulation is shown in Fig. 4.5a and Fig. 4.5b. It is coherently setup in the following figures that, the X axis refers to different IVC timings while the Y axis refers to the parameter value. All the IVC modulations of each operating point are in different markers connected by solid lines, in order to show the trend of the IVC modulation's effect on the parameters. All the IVC modulations achieves the desired engine speed. However, the engine failed in generating desired brake torque at late IVC of +100CAD (crank angle degree). By further looking into the time plots of the controllers from the simulation, the intake throttle valve in the Mixer module, which is controlled by target brake torque input, isn't able to achieve steady target torque even with full throttle (valve fully open at 90 deg). The throttle valve even diverges/ oscillates at 1600rpm and 1800rpm with IVC+100CAD. Therefore, the engine can't function properly at extreme late IVC modulation at least without other modifications, and the data points for IVC+100CAD are treated as outliers and do not help in analyzing the effect of IVC modulation.



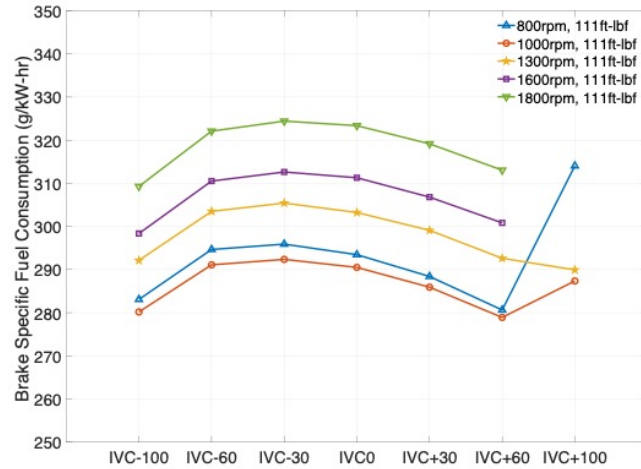
**Figure 4.5.** Operating condition - IVC modulation.

Fig. 4.6a and Fig. 4.6b show the gas flow rates under IVC modulation. It's observed that both air and fuel flow form hill shape, and the fuel consumption is smaller than stock

IVC at IVC-100CAD and IVC+60CAD. The observation can also be justified in Fig. 4.7, where the fuel consumption per power output is significantly smaller at IVC-100CAD and IVC+60CAD, with the biggest value at IVC-30CAD.



**Figure 4.6.** Air & Fuel flows - IVC modulation.



**Figure 4.7.** Brake specific fuel consumption - IVC modulation.

The Volumetric efficiency is shown in Fig. 4.8. Volumetric efficiency is the ratio of the volume of air charge drawn into the cylinders during the suction stroke to the total cylinder displacements at the atmospheric pressure, i.e., it denotes the engine's ability to carry out the work efficiently. The highest volumetric efficiency happens at IVC-30CAD.

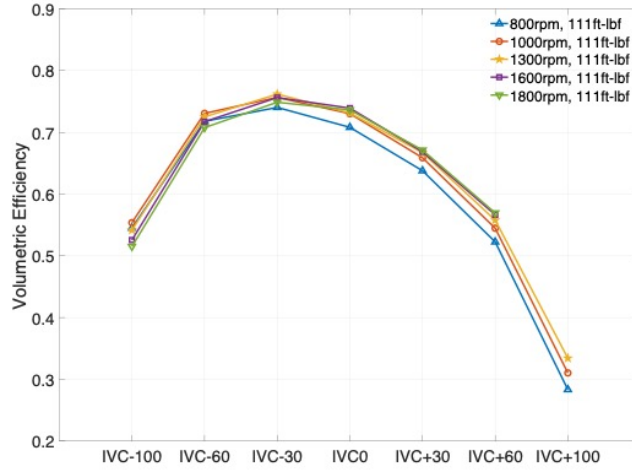
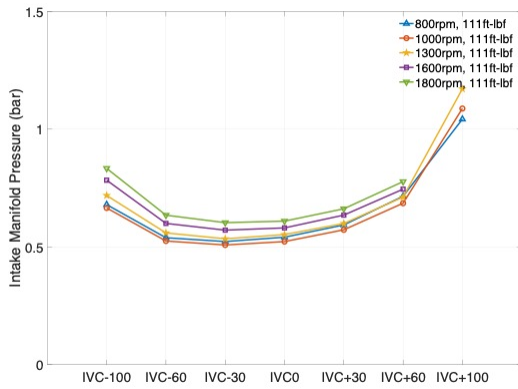


**Figure 4.8.** Volumetric efficiency - IVC modulation.

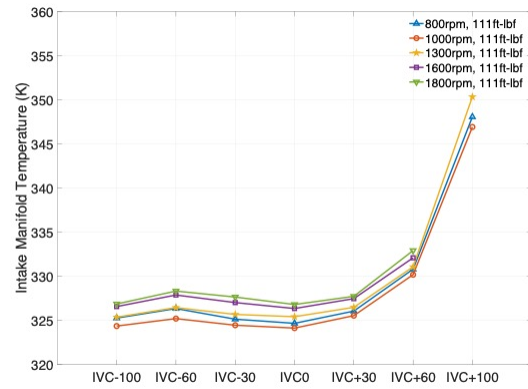
The pressures and/or temperatures of The intake, cylinder and exhaust side were also analyzed under IVC modulation. Fig. 4.9 shows the intake manifold pressure & temperature, as well as turbine inlet pressure & temperature. The intake manifold pressure (Fig. 4.9a) follows the inverse trend of air and fuel flows, while on the exhaust side, especially the turbine inlet pressure is almost unchanged under IVC modulation. The average of peak cylinder pressure follows the trend of air and fuel flows.

The mean effective pressures are shown in Fig. 4.10d. The gross indicated mean effective pressure (GIMEP) is proportional to the power loop outlet and thus follows the peak cylinder pressure curves & fuel flows. The net indicated mean effective pressure is almost identical under the IVC modulation, and the absolute pumping mean effective pressure gets smaller at extreme IVC modulations, where the pumping loop seemed getting smaller. Therefore, the LogP~LogV diagram is also presented in Fig. 4.11 for verification.

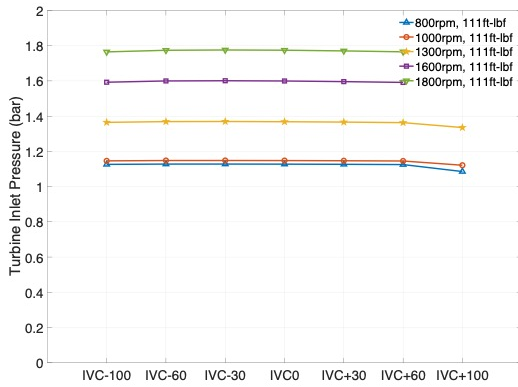
The LogP~LogV are presented sequentially in terms of the amount of IVC timing changes from stock timing, so that the curves can be seen more clearly. In Fig. 4.11a, the IVC-30CAD generates a larger power loop, while the IVC+30CAD generates smaller pumping and power loops. Moving on to Fig. 4.11a, the IVC-60CAD doesn't present significant differences, while the IVC+60CAD keeps shrinking both the pumping and power loops. When the valve closure timing change comes to  $\pm 100$ CAD, the IVC-100CAD noticeably shrinks in both the



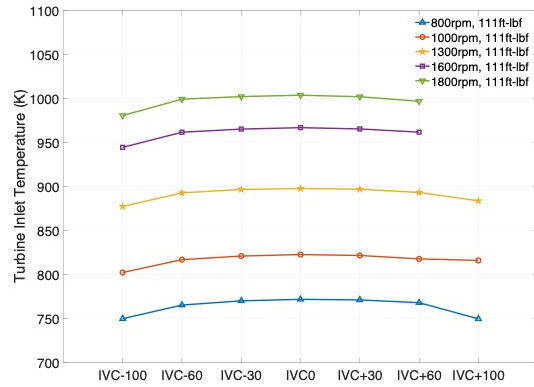
(a) Intake manifold pressure.



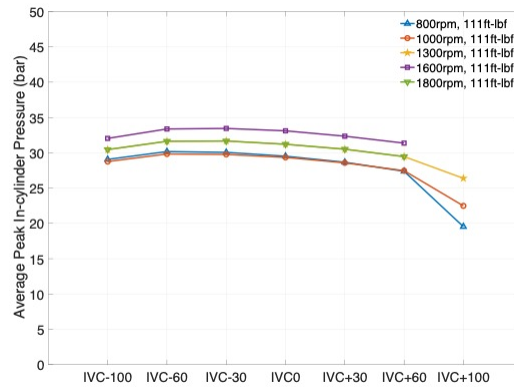
(b) Intake manifold temperature.



(c) Turbine inlet (exhaust manifold) pressure.



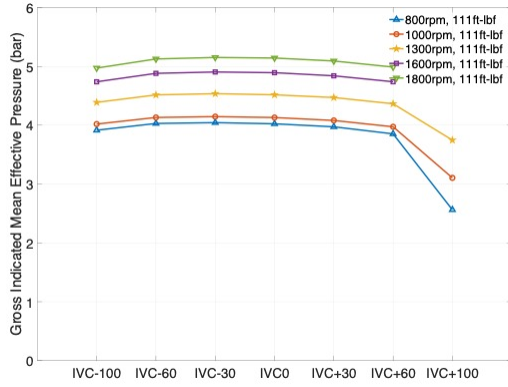
(d) Turbine inlet temperature.



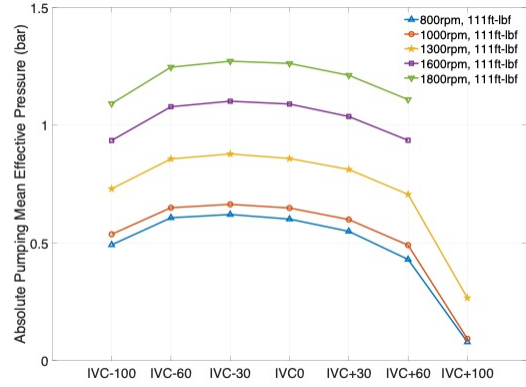
(e) Average peak in-cylinder pressure.

**Figure 4.9.** Pressures and temperatures - IVC modulation.

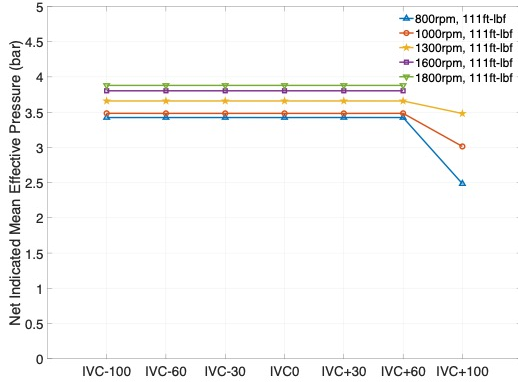
pumping and power loops; however, the IVC+100CAD has changed/ shrunk too much, to



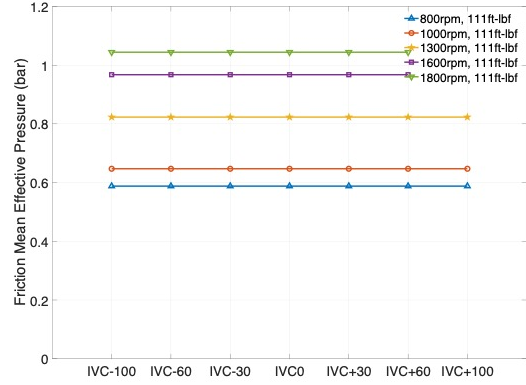
(a) Gross indicated mean effective pressure.



(b) Absolute pumping mean effective pressure.



(c) Net indicated mean effective pressure.



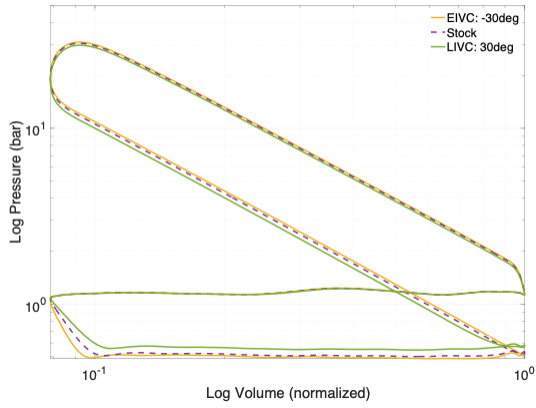
(d) Friction mean effective pressure.

**Figure 4.10.** Mean effective pressures - IVC modulation.

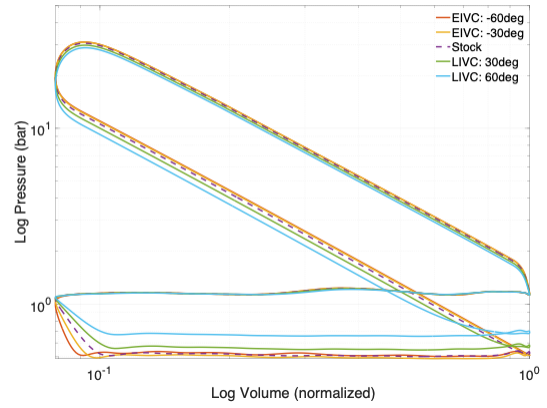
the extent that it is not capable of generating the desired powers (as seen in the brake torque curves in Fig. 4.5b).

The engine efficiencies are also shown in Fig. 4.8 for observation and discussion.

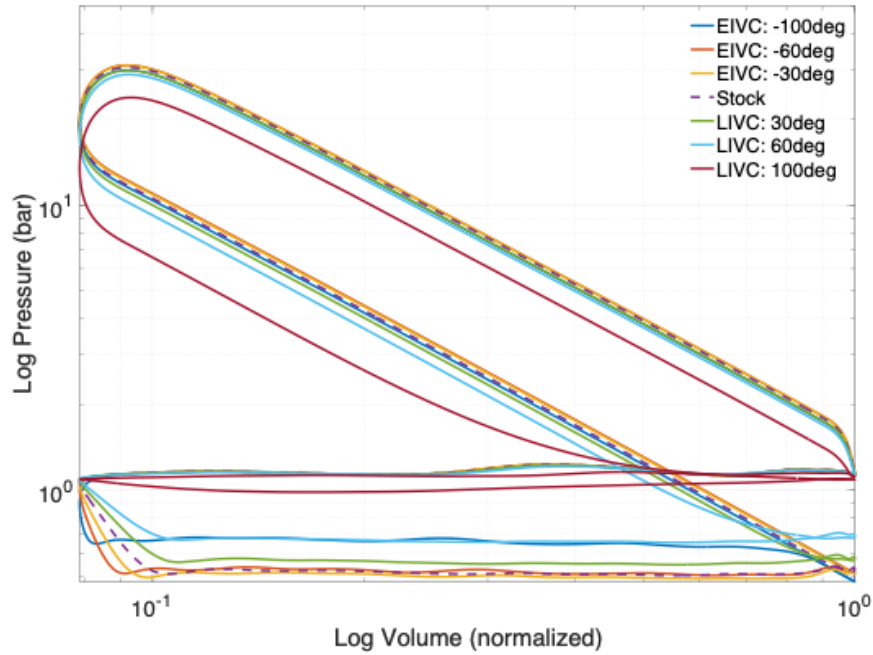
- The closed cycle efficiency (CCE) is both proportional to GIMEP (hill shape) and reciprocal to fuel flow rate (hill shape), so its overall trend is not obvious.
- The open cycle efficiency is proportional to NIMEP (almost flat) and reciprocal to GIMEP (hill shape), so its overall trend is bowl shape
- the mechanical efficiency is related to BMEP and NIMEP which are both insignificant.



(a) Stock & IVC $\pm$ 30CAD



(b) Stock & IVC $\pm$ 30CAD & IVC $\pm$ 60CAD

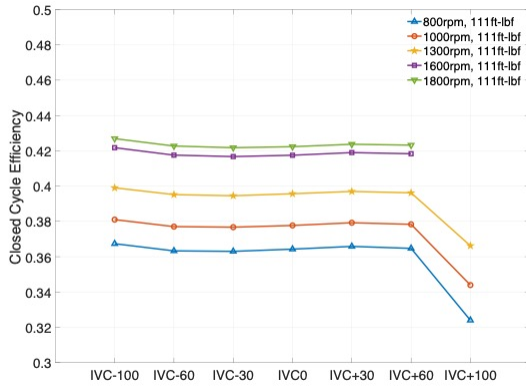


(c) Stock & IVC $\pm$ 30CAD & IVC $\pm$ 60CAD & IVC $\pm$ 100CAD

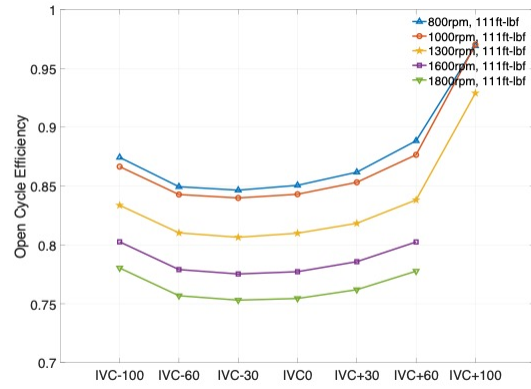
**Figure 4.11.** LogP~LogV at 1300rpm, 111ft-lbf - IVC modulation.

- The brake thermal efficiency, being the product of all three previous efficiencies, is also in bowl shape.

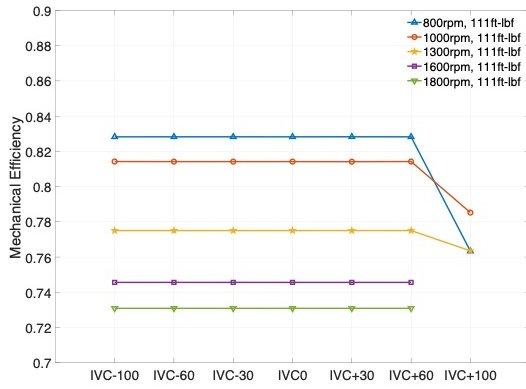
Therefore, some conclusions can be drawn:



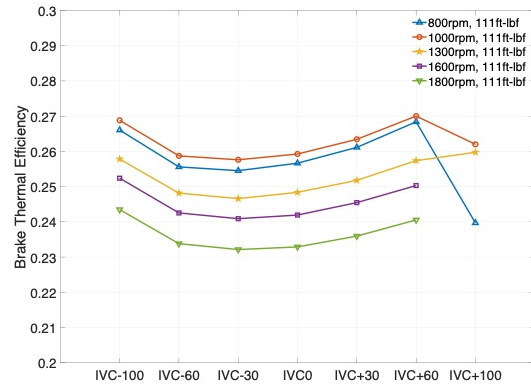
(a) Closed cycle efficiency.



(b) Open cycle efficiency.



(c) Mechanical efficiency.



(d) Brake thermal efficiency.

**Figure 4.12.** Engine efficiencies - IVC modulation.

- IVC modulation can affect some parameters. The system performance reaches its local maximum/ minimum at IVC-30CAD, and can be pushed to the opposite direction by continuing moving the timing ahead (Early IVC).
- Late IVC can be helpful in reducing pumping loss. However, it can only be modified within a small range before the system fails to converge.
- The IVC modulation's effect follows a similar trend among different operating points selected here. It is worth pushing investigation to a larger region and verify if the trend is still unchanged.

### 4.3 Cylinder de-Activation

Cylinder de-activation (CDA), also one of the VVA technologies, is an approach in multi-cylinder engines where a combination of cylinders are systematically disabled, to effectively reduce the engine's effective displacement, improving overall engine efficiency and fuel economy. CDA is implemented by suspending fueling and valve events for the deactivated cylinder(s). To maintain torque, the fueling of the active firing cylinders is increased, thus increase individual active cylinder combustion and also increase the exhaust temperature [21].

CDA can be implemented on multiple cylinders of an engine providing variations of active cylinder displacement, as are shown in Fig. 4.13. Fig. 4.13a represents the stock working condition, where all 6 cylinders work under the stock intake & exhaust valve profiles in the regulated firing order; Fig. 4.13b represents the condition where cylinders 1's and 6's intake and exhaust valves are closed which de-activates the two cylinders, and it's named here as 2CDA meaning "2 cylinders de-activated"; Fig. 4.13c represents the condition where cylinders 4, 5 & 6 (or 1, 2 & 3, or inter-switched periodically) are de-activated, named here as 3CDA (3 cylinders de-activated); and lastly, Fig. 4.13d represents the condition where cylinders 1, 2, 5 & 6 are de-activated, named here as 4CDA (4 cylinders de-activated). As the number of the de-activated cylinders increases, the cylinders that still remain active will need to individually generate more power to match the desired torque command, thus the each active cylinder's mass flow and combustion will show noticeable increase.

As the demanded torque increases, the mass flow and pressure in each cylinder increases. Therefore, CDA is not as effective nor preferred in high torque regions because the remaining active cylinders could work under a higher pressure than rated, which can negatively affect the components' durability. Depending on the desired torque, the number of cylinders to be deactivated can vary. The following results are simulated under 1300rpm and under various torques, including 25, 50, 75, 100, 125, 150, 200, 250, 300, 350, 400 ft-lbf, to demonstrate the CDA effects.

Fig. 4.14 shows the air & fuel mass flow rate under various torques at 1300 rpm. It is coherently setup in the following figures that, the X axis refers to different actuated torques while the Y axis refers to the parameter value. All the operating points of each CDA



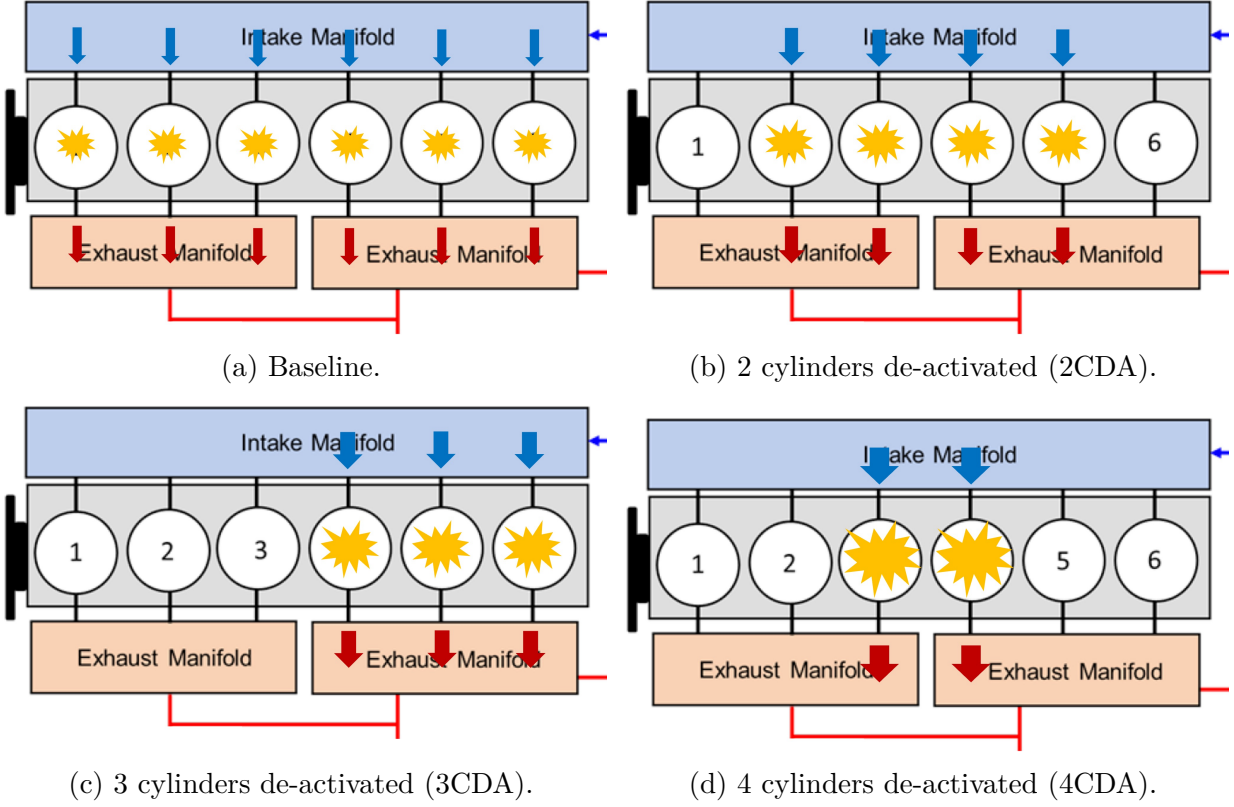


**Figure 4.13.** Cylinder de-activation modes.

modulations (baseline, 2CDA, 3CDA, and 4CDA) are in different markers connected by solid lines, in order to show the trend of the CDA modulation's effect on the parameters. However, in this simulation, the 2CDA setup renders stable torque output up to 350 ft-lbf, the 3CDA setup renders stable torque output up to 200 ft-lbf, while the 4CDA setup only renders stable torque output for 25 & 50 ft-lbf. As was also mentioned previously, it is because the more cylinders de-activated, the more difficult it will be to reach the desired torque with the remaining active cylinders. Therefore, the plot only includes the cases where the engine renders stable speed and torque output. Since the desired Air-Fuel Ratio in the test remains the same for different CDA modulations at the same operating point, the air flow and fuel flow shows identical trend. When the number of de-activated cylinders increases for a single operating point, the fuel (and air) consumption decreases significantly, as shown in Table 4.1. At 1300 rpm and 25 ft-lbf, the fuel flow rate decrease by 13.6% for 2CDA, 21.5% for 3CDA and 27.5% for 4CDA; As the torque increases, the percentage of fuel rate decrease by CDA

becomes smaller but it's still a significant amount, at more than 5% reduction for 1300 rpm and 300 ft-lbf.

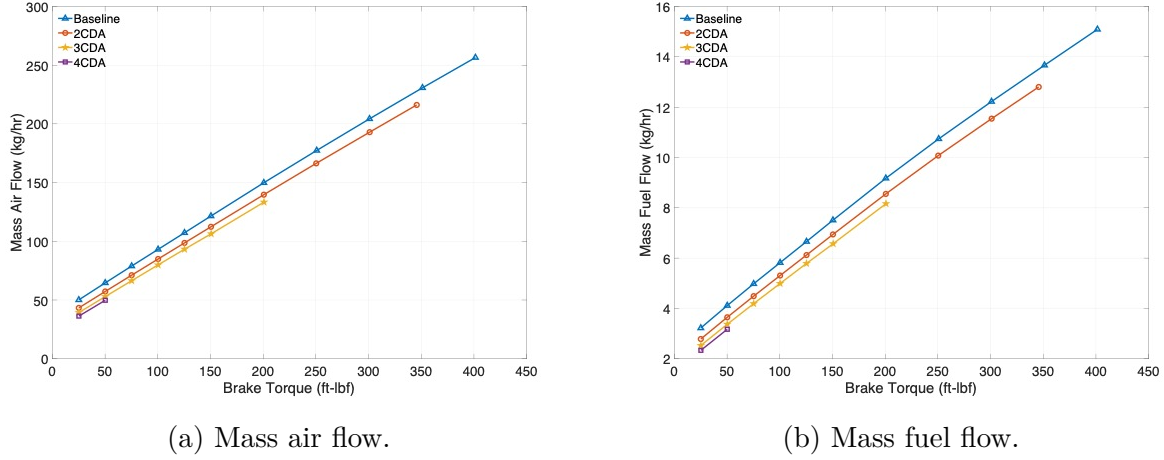


**Figure 4.14.** Air & Fuel flows - CDA modulation, at 1300rpm.

**Table 4.1.** Fuel consumption reduction - CDA modulation, at 1300rpm.

Cases	25 ft-lbf	50 ft-lbf	100 ft-lbf	150 ft-lbf	200 ft-lbf	300 ft-lbf
2CDA	-13.6%	-11.3%	-8.8%	-7.6%	-6.8%	-5.6%
3CDA	-21.5%	-18.1%	-14.2%	-12.5%	-11.0%	
4CDA	-27.5%	-22.9%				

When focusing on torque range smaller than 150 ft-lbf, where CDA effect is more significant across the speed range, the fuel consumption decrease for two other operating points are also shown in Table 4.2 for 1000 rpm and Table 4.3 for 1600 rpm. The fuel consumption is consistently able to be reduced by more than 15% at below 50 ft-lbf, and more than 10% at below 100 ft-lbf, and more than 5% at below 150 ft-lbf.

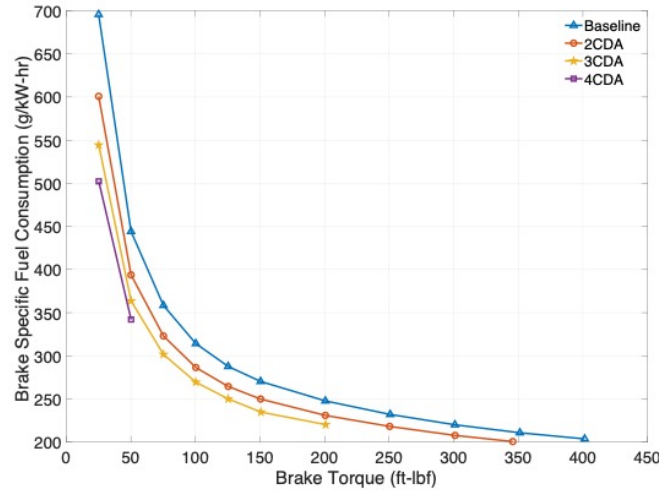
**Table 4.2.** Fuel consumption reduction - CDA modulation, at 1000rpm.

Cases	25 ft-lbf	50 ft-lbf	100 ft-lbf	150 ft-lbf
2CDA	-11.2%	-9.4%	-8.1%	-6.9%
3CDA	-18.0%	-15.1%	-13.1%	
4CDA	-22.8%			

**Table 4.3.** Fuel consumption reduction - CDA modulation, at 1600rpm.

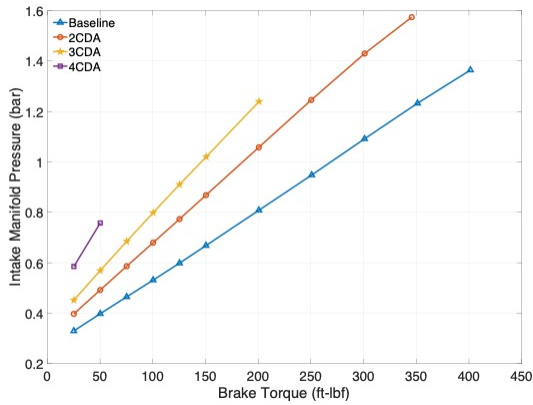
Cases	25 ft-lbf	50 ft-lbf	100 ft-lbf	150 ft-lbf
2CDA	-13.7%	-11.8%	-9.6%	-8.3%
3CDA	-21.7%	-18.7%	-15.3%	-13.4%
4CDA	-27.5%	-23.6%		

Brake specific fuel consumption (BSFC) is also a measure of the engine's fuel economy at a certain operating point. In Fig. 4.15, at the same speed (1300 rpm), the engine consumes larger fuel amount at lower torque than higher torque for the same amount of power output. The implementation of CDA helps significantly lower the fuel consumption per unit power output. It is undeniable that CDA is very promising in improving fuel economy for an existing engine at low load condition, e.g., urban driving and light towing work.

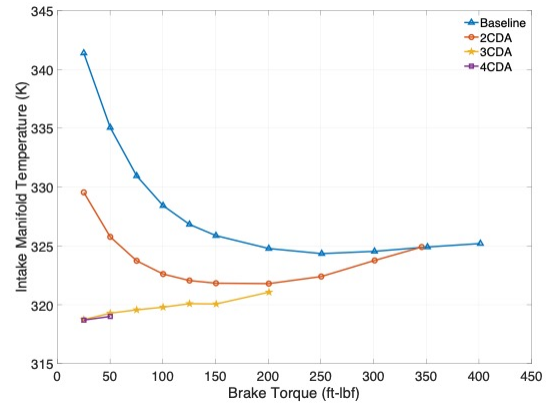
**Figure 4.15.** Brake specific fuel consumption - CDA modulation.

The following plots in Fig. 4.16 shows the changes from intake and exhaust sides of the engine caused by CDA modulation. It's noted that the turbine outlet is one of the boundaries in the GT model and can possibly vary because of the different pressure and temperature range in active cylinders, but the results in this section were set with the same turbine outlet boundary condition for all CDA modes, which is expected to be updated once there is more experimental result in test cell as baseline. However, the pressures and temperatures here still shows the CDA's effect to some extent and is worth investigation. The intake

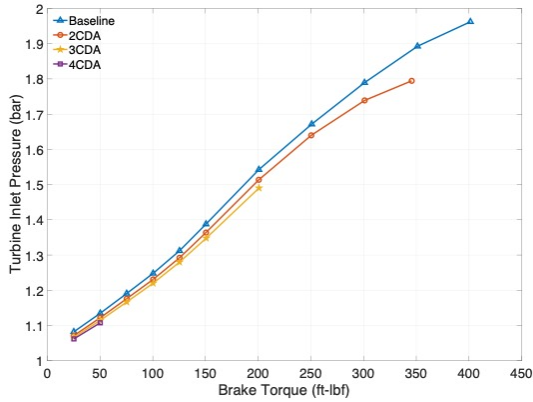
manifold pressure increases with decrease in active cylinder number, because the area where the mixed gas flows through the engine decreases which needs a higher throttling effort per unit gas weight. The intake manifold temperature, on the contrary, decreases with fewer active cylinders. On the exhaust side, it is not as significant as the intake side, but the exhaust pressure decreases with fewer active cylinders, possibly because of a smaller amount of exhaust gas flow. The trend of CDA effect on exhaust temperature is not as clear, where the 3CDA setup has the highest exhaust temperature at below 150 ft-lbf.



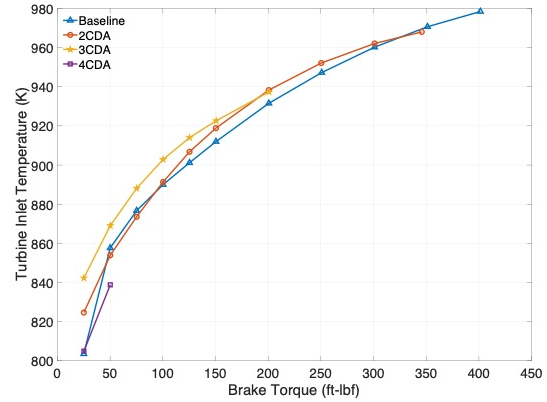
(a) Intake manifold pressure.



(b) Intake manifold temperature.



(c) Turbine inlet (exhaust manifold) pressure.



(d) Turbine inlet temperature.

**Figure 4.16.** Pressures and temperatures - CDA modulation.

A comparison of the LogPLogV diagram with different CDA modes is shown in Fig. 4.17, for 1300 rpm and 50 ft-lbf. The curves all come from the 4th cylinder because it's the cylinder that's open under all CDA modes. The exhaust stroke for all CDA modes are

similar, as is seen with the turbine outlet pressure shown previously, while the intake stroke increases with fewer active cylinders. Therefore, the fewer cylinders active, the significantly less pumping loss (corresponding to the pumping loop) and the significantly more gross power output (corresponding to the power loop).

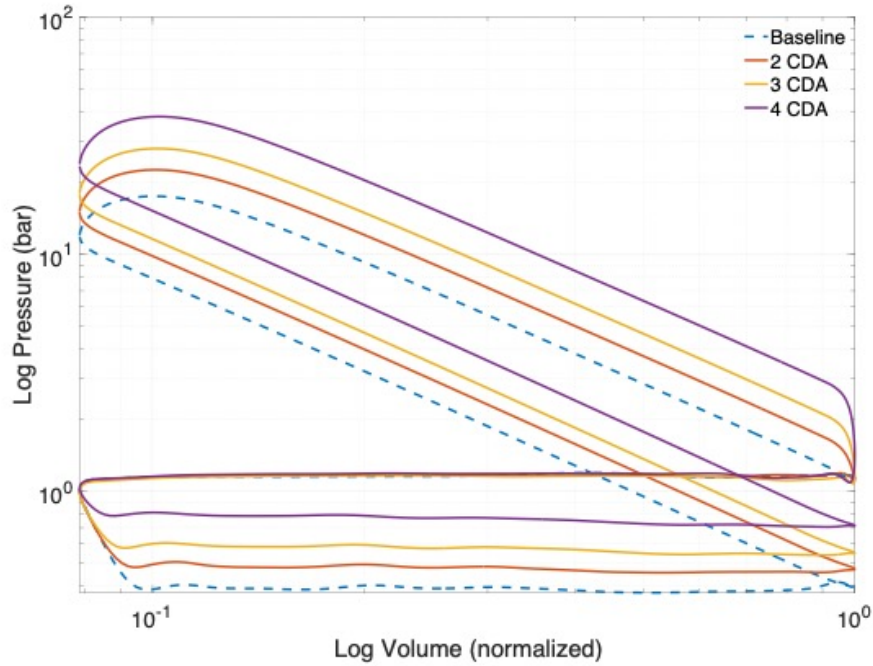
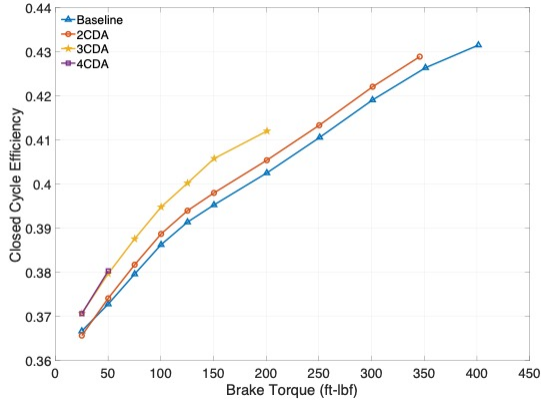


**Figure 4.17.** LogP~LogV at 1300rpm, 50ft-lbf - CDA modulation.

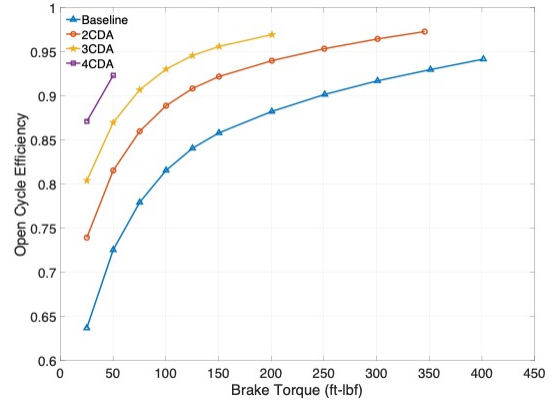
The plots in Fig. 4.18 are the engine efficiencies. As mentioned previously, the closed cycle efficiency (CCE) is the efficiency of the gross engine power over the total power generated. There is tendency in improved closed cycle efficiency with fewer active cylinders, possibly due to the decrease in heat transfer losses across the engine.

The open cycle efficiency (OCE) is directly related with the pumping loss, and is readily available from the PV diagram. The less the pumping loss with respect to the gross power output, the better the OCE. Therefore, as shown in Fig. 4.18b, OCE increases with fewer active cylinders.

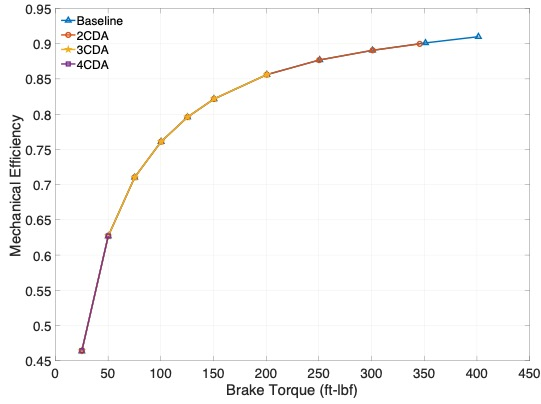
The mechanical efficiency is directly related with brake power and friction loss. Since neither of the two powers are affected by the CDA modulation, the mechanical efficiency remains unaffected.



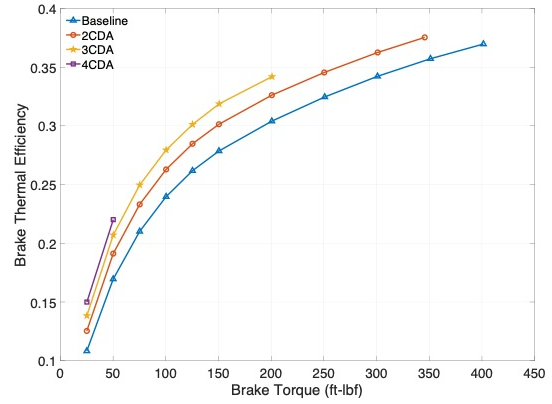
(a) Closed cycle efficiency.



(b) Open cycle efficiency.



(c) Mechanical efficiency.



(d) Brake thermal efficiency.

**Figure 4.18.** Engine efficiencies - CDA modulation.

The brake thermal efficiency, being the product of the three efficiencies above, is proportional to both the CCE trend and the OCE trend, and thus increases with fewer active cylinders. Therefore, CDA is beneficial for improving the overall engine efficiency, as it's inversely proportional to the BSFC trend.

#### 4.4 CDA on TWC emission control

In previous section, CDA has shown its benefit for fuel economy in the low torque region. With multiple cylinders deactivated, the active cylinders can work at a higher pressure and temperature condition which can lead to a more complete chemical reaction. Due to its reduction in gas flow, it can be beneficial for conquering the over-oxidation issue coming

from fuel-cut events in TWC emission study from Chapter 2, by reducing the amount of engine exhaust gas going into the TWC during low load and fuel cut events, without losing too much temperature in the catalyst (which also helps  $CH_4$  reduction). In this section, CDA's effect on TWC emission outer loop control is investigated.

The fuel economy shown previously in Table 4.1 was with EGR. Although EGR is also potentially beneficial to emission reduction because it reduces the amount of exhaust pollutant species by recirculating portion of the exhaust gas back to intake port for another round of reaction, it is not the purpose of the work here and can possibly interfere with CDA's effect on the overall performance. Thus, to re-evaluate CDA's effect on the engine fuel economy, the GT model with fully closed EGR valve at 1300 rpm is re-run and the fuel mass reduction is shown in Table 4.4. The result here is actually very close to the result in Table 4.1, partly because EGR is not heavily used in low torque condition, with only around 2% EGR fraction at 200 ft-lbf. Therefore, the CDA effect discussed in previous section still applies here.

**Table 4.4.** Fuel consumption reduction - CDA modulation, at 1300rpm.

Cases	25 ft-lbf	50 ft-lbf	100 ft-lbf	150 ft-lbf	200 ft-lbf
2CDA	-13.6%	-11.3%	-8.8%	-7.6%	-6.8%
3CDA	-21.6%	-18.1%	-14.2%	-12.3%	-11.1%
4CDA	-27.5%	-22.9%			

#### 4.4.1 CDA on TWC's FOS variation

For the purpose of facilitating environmental setup and data post-processing, expanding the possibility of implementing advanced control strategies, and coupling with other software-based models, a coupled simulation environment of Simulink, GT-Suite s-function, and AVL Boost s-function is built. The co-simulation is setup so that it inputs desired engine speed, brake torque, air-fuel ratio, as well as the intake & exhaust valve profiles from MATLAB/Simulink environment to the GT Power model, and outputs real-time actual engine speed, brake torque, and air & fuel flow rate from GT model to the Simulink for VVA technology investigation purpose. The data that are used for GT model coupling mainly consists of

the parameters mentioned previously, but the coupled simulation environment has a broad possibility in terms of taking what's useful from the GT model and analyzing in the Simulink environment.

CDA's effect on TWC's oxidation / reduction process is first investigated. As shown in Fig. 4.19, A constant desired speed and torque combination (at 1300 rpm and 50 ft-lbf) is the input to the engine and after-treatment system. The system is first run under stoichiometry for 600s because the TWC's initial temperature is low and need time to rise to a relatively steady warm temperature, where the catalytic reaction is better and more stable. After the TWC temperature almost stabilizes at 600s (in the second figure of Fig. 4.19), the engine runs under lean condition to fully oxidize the TWC before it runs under a round of lean-to-rich and rich-to-lean to investigate the entire TWC reduction and oxidation processes. Then the engine switches to other CDA modes at lean condition (2CDA, 3CDA, and 4CDA, sequentially) and run each CDA modes under a round of lean-to-rich and rich-to-lean for TWC reactions. It's seen in the first figure of Fig. 4.19 that the real-time speed and torque remains achievable and constant except for the torque stabilization when  $\lambda$  and CDA mode changes. The TWC temperature stays identical at 4 CDA modes; The real-time Engine out  $\lambda$  follows along the desired  $\lambda$ ; the air flow rate keeps dropping with CDA mode change because of fewer and fewer active cylinders; and the TWC1 and TWC2 complete full oxidation / reduction at each lean / rich switch.

In Fig. 4.20,  $CO$ ,  $CH_4$ , and  $NO_x$ 's instant emission at TWC1 inlet (blue), TWC1 outlet (red) and TWC2 outlet (orange) are shown in ppm. For  $CO$ , the density of  $CO$  flowing into the TWC remains similar, while the density of  $CO$  leaving the TWC decreases as the CDA modulation goes more aggressive (i.e., de-activating more cylinders). The density of  $CH_4$ , similar to  $CO$ , is decreased more as more cylinders are de-activated. The density of  $NO_x$ , which is most sensitive to the engine's lean-rich condition, doesn't decrease more at steady state when more cylinders are de-activated; However, the  $NO_x$  density leaving the TWC raises slower to the peak when the engine transitions from rich to lean. It is also worth noting that the mass flow is also reduced with fewer active cylinders. Therefore, CDA modulation can be beneficial to emission reduction by both reducing the harmful gas density and the mass gas flow.



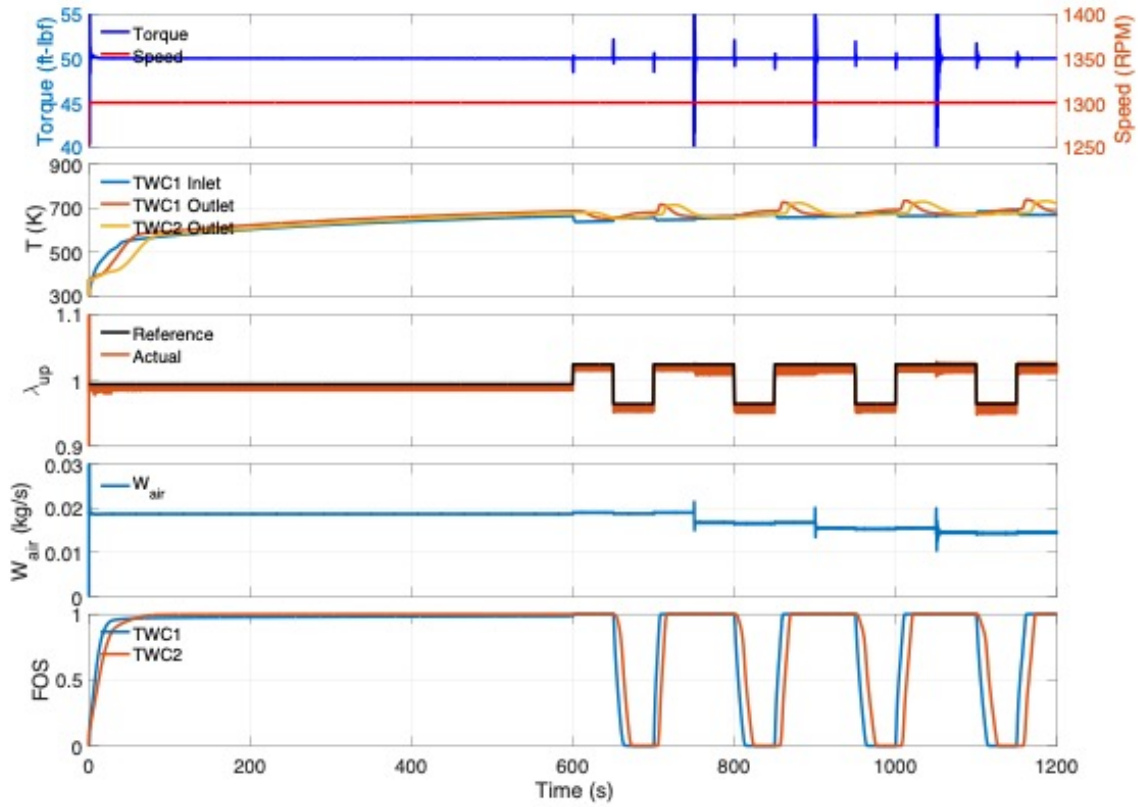


**Figure 4.19.** Parameter variations with CDA modulation, under 1300 rpm and 50 ft-lbf.

More detailed mode-by-mode comparison of 4 CDA modes are shown in Fig. 4.21. Fig. 4.21a shows the Actual Torque, Engine  $\lambda$ ,  $W_{air}$ , and TWC1's and TWC2's FOS when command  $\lambda$  input changes from lean to rich, while Fig. 4.21b shows the changes when command  $\lambda$  input changes from rich to lean. Blue curves represent baseline, red curves represent 2CDA, orange curves represent 3CDA, and purple curves represent 4CDA.

In Fig. 4.21a, when a step signal of rich reference  $\lambda$  incites the engine, the engine reacts to the input change and stabilizes, which shows in the Torque response in the first sub-figure. The fewer active cylinders there are, the slower the engine stabilizes, which is because it requires a higher effort with a more restricted active cylinder number. There is a slight fluctuation observed in the mass flow rate before stabilization in the third sub-figure, while the engine  $\lambda$  shares almost identical response across the CDA modes. It is significant in both TWC1 and TWC2 that fewer active cylinders reduces the TWC slower.

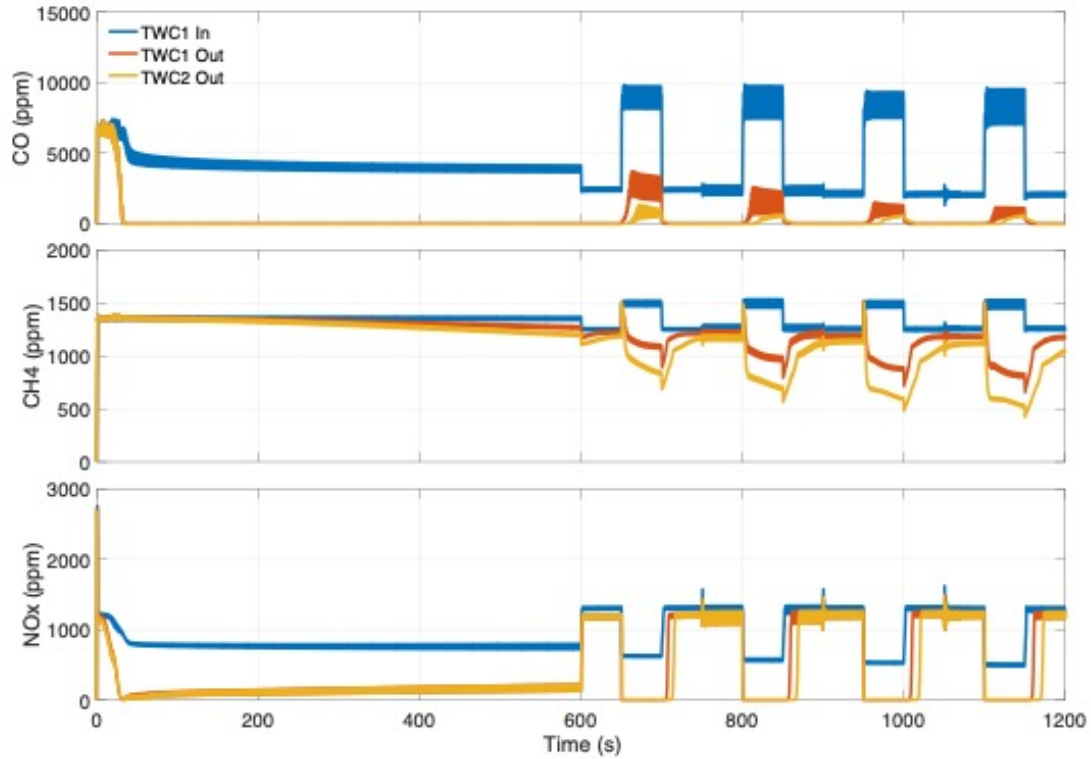
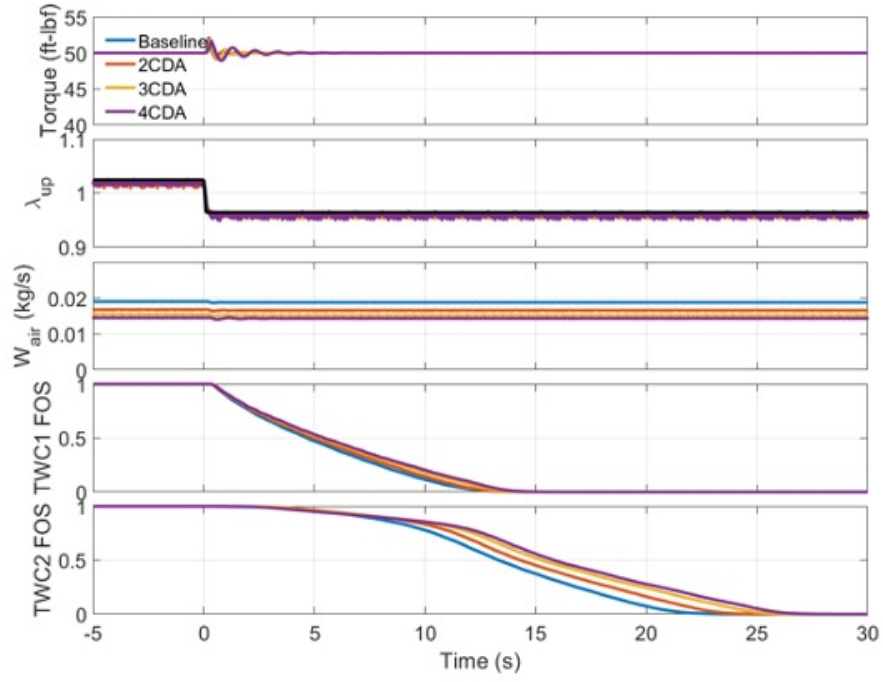


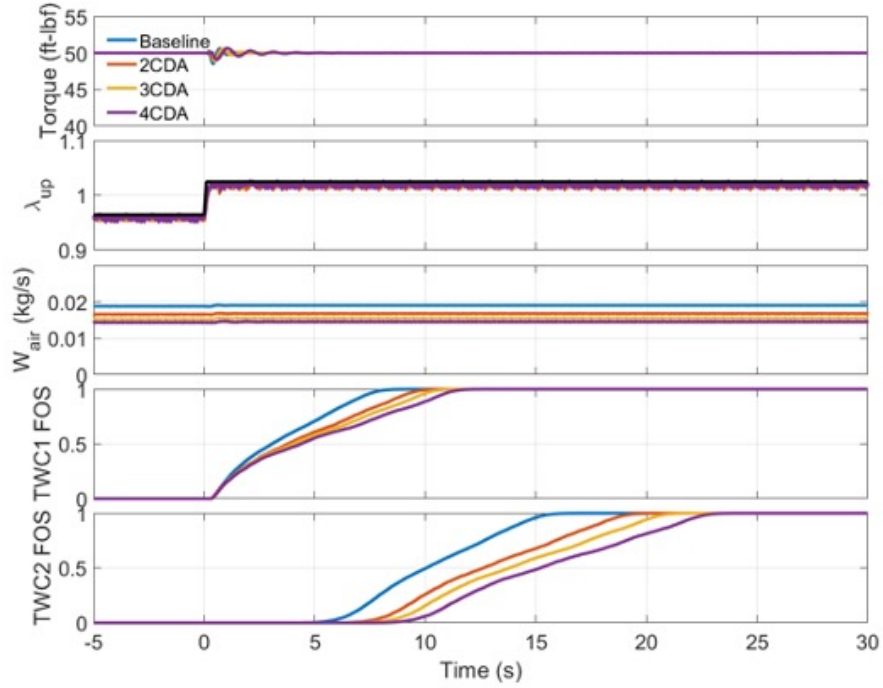
**Figure 4.20.** Instantaneous emissions with CDA modulation, under 1300 rpm and 50 ft-lbf.

On the other hand, in Fig. 4.21a, when a step signal of lean reference  $\lambda$  incites the engine, the trend of CDA effect remains similar. The fewer active cylinders there are, the slower the torque stabilizes. The mass flow rate also slightly fluctuates during input change before stabilization, and the engine  $\lambda$  shares almost identical response across the CDA modes. The fewer active cylinders there are, both the TWC1 and TWC2 reduce slower.

Therefore, CDA modulation helps slow down TWC from both oxidation and reduction, reduces the mass flow across the system, and thus leaves more buffer to the TWC and keeps the oxidation level (i.e., FOS) longer within effective working range so it can reduce the harmful gases more effectively.



(a) TWC reduction under lean-to-rich condition.



(b) TWC oxidation under rich-to-lean condition.

**Figure 4.21.** Parameter variations with CDA modulation, under 1300 rpm and 50 ft-lbf.

#### 4.4.2 CDA on emissions during fuel-cut events

To implement the CDA together with the TWC outer loop emission controller in Chapter 2, the engine's dynamics after CDA modulation needs to be added into the Simulink environment. Because the B6.7N engine in the GT modeling / VVA research work is different from the engine in the TWC emission control research work in terms of the working range, i.e., the speed and torque ranges (the B6.7N engine's fuel map covers from 700 rpm to 2750 rpm, while the other engine covers from 800 rpm to 3500 rpm), the B6.7N engine can't run the Otto-FTP drive cycle which was used in Chapter 2. To overcome this issue and still demonstrate the CDA effect on an apple-to-apple comparison basis, a simplification to the engine CDA modulation is made by implementing the flow reduction by CDA at low torque range to the original engine instead of fully coupling the B6.7N engine GT model. Although this simplified implementation doesn't cover all the engine dynamics / characteristics, it is believed to still be able to demonstrate the trend of CDA's effect and serve as a guidance for future test cell after-treatment experiment.

To demonstrate CDA's effect on emissions, the work consists of three parts:

- For engine with fuel cut-off feature, only apply CDA during fuel-cut events and see the changes in tail-pipe emissions and fuel economy.
- For engine with fuel cut-off feature, fully apply CDA, i.e., during low torque conditions (also including fuel-cut events).
- For engine without fuel cut-off feature, fully apply CDA, i.e., during low torque conditions.

The first part is the easiest to apply in practice because the CDA modulation is only applied to zero or negative torque condition and doesn't require a calibrated CDA engine mapping for implementation. It aims directly at fuel-cut's negative effect on TWC over-oxidation and is expected to improve the emission performance by reducing the flow during the fuel-cut events.

As shown in previous section for the B6.7N engine, the CDA can reduce the fuel flow (and also the air flow because of constant AFR) by more than 20% at extreme low torque

condition (at 25 ft-lbf), and still by more than 5% at 150 ft-lbf at multiple engine speeds. In the first part, the mass flow rate during fuel-cut events is assumed reduced by 20% (i.e., 80% mass flow).

The 5 control strategies in Chapter 2 are simulated with the updated setup, and the comparison on overall fuel consumption is shown in Fig. 4.22. There is not much fuel consumption changes for any of the strategies. This is mostly because, firstly and for most, there is already zero new fuel injected to the system during fuel-cut events, thus flow reduction doesn't further reduce fuel input during the events; and secondly, even though the TWC status after each fuel-cut event is different between before and after adding the CDA which affect the outer controller performance, the engine  $\lambda$  is within a small range around stoichiometry and the flow is almost the same because it mainly depends on transient torque and speed, thus no noticeable fuel change occurs either.

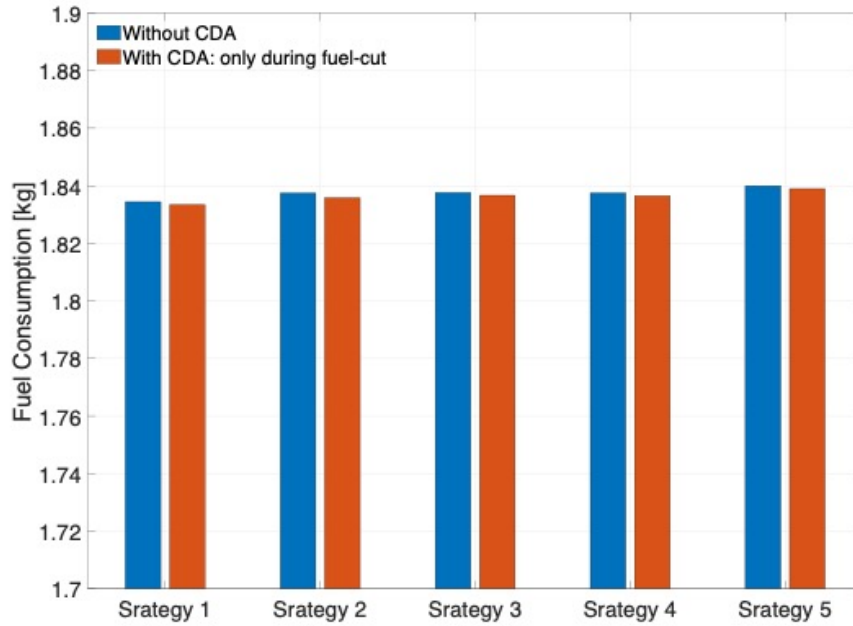


**Figure 4.22.** Fuel consumption under Otto-FTP cycle, without CDA vs. with CDA of 80% flow during fuel-cut events.

The overall emission control performance improvement under Otto-FTP cycle is shown in Fig. 4.23. The left figure is emission result of all 5 strategies with fuel cut-off, previously

shown in Fig. 2.34 from Chapter 2, the right figure is the updated emission result of all 5 strategies with fuel cut-off, after the CDA implementation on fuel-cut events only. By looking at Fig. 4.23b alone and in comparison with Fig. 4.23a, the trends and differences among the 5 strategies still remains similar to what was before the CDA implementation, i.e., an outer-loop controller is essential for the reduction of  $NO_x$  emissions AND the reduction of  $NO_x$  achieved by FOS-based strategies can be better than non-FOS-based strategies even with engine fuel cut-offs.

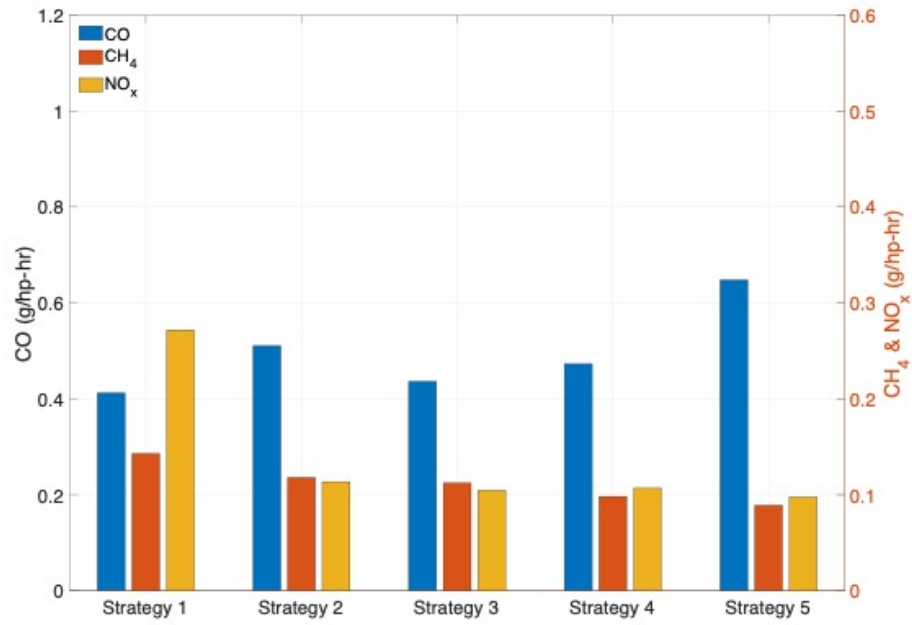
When it comes to each strategy's own emission comparison of before vs. after CDA implementation, it is great to see that all strategies'  $CH_4$  and  $NO_x$  emissions are more or less decreased with CDA implementation. The  $CO$  emission is not all decreased, but not all are changed significantly except for Strategy 3 which is with the binary outer loop controller.

Because of the observed improvement on  $CH_4$  and  $NO_x$  emission reductions with 20% flow reduction during fuel-cut events, further flow reductions are simulated for comparison. As mentioned before, the engine CDA implementation was assumed with 20% reduction because the B6.7N engine's CDA can reduce more than 20% flow at extreme low torque condition. Since there's no new fuel input and thus no new combustion during fuel-cut events, the flow reduction can be even more aggressive with flow regulation and valve control. Therefore, a 70% mass flow and a 60% mass flow are simulated.

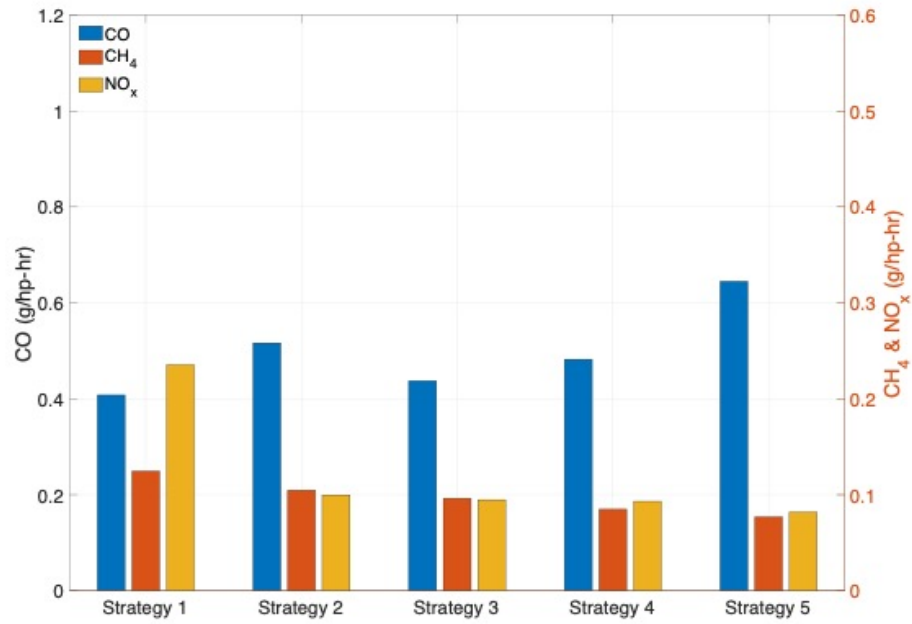
The comparisons on overall fuel consumption is shown in Fig. 4.24. A more reduced flow rate doesn't reduce the fuel consumption further for any of the strategies. This is due to the same reason as stated previously, that the CDA implementation doesn't further decrease fuel consumption during or around the fuel-cut events. A detailed table of the percentage change of fuel consumption with various CDA flow reductions is shown in Table 4.5. All strategies' fuel consumption are 0.1% smaller than before implementing CDA, which is negligible.

**Table 4.5.** Changes on the fuel consumption under Otto-FTP cycle, after CDA implementation compared to before CDA, during fuel-cut events only.

Cases	Strategy 1	Strategy 2	Strategy 3	Strategy 4	Strategy 5
With CDA: 80% flow	-0.1%	-0.1%	-0.1%	-0.1%	-0.1%
With CDA: 70% flow	-0.1%	-0.1%	-0.1%	-0.1%	-0.1%
With CDA: 60% flow	-0.1%	-0.1%	-0.1%	-0.1%	-0.1%



(a) Without CDA implementation.



(b) With CDA implementation of 80% flow during fuel-cut events.

**Figure 4.23.** Tailpipe emissions under Otto-FTP cycle, without CDA vs. with CDA during fuel-cut events.

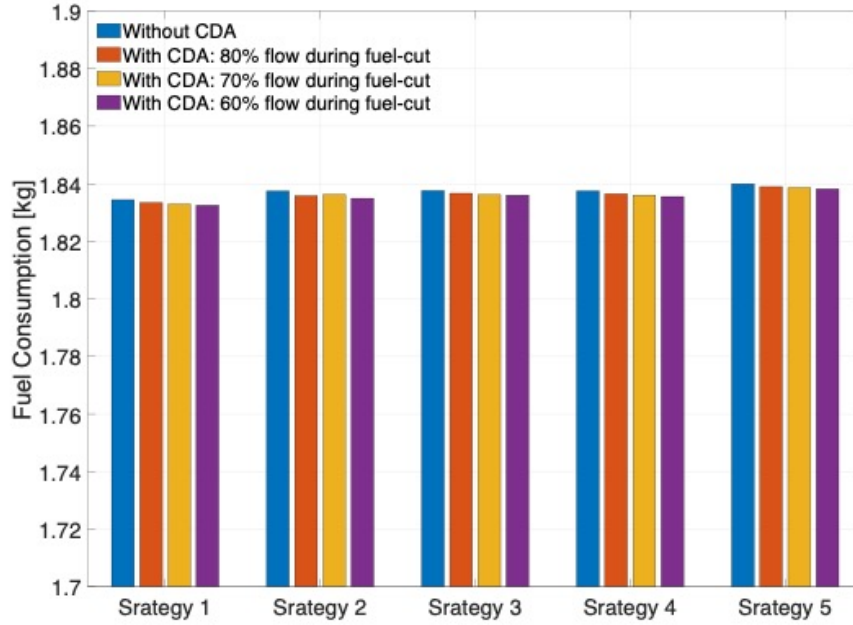


**Figure 4.24.** Fuel consumption under Otto-FTP cycle, without CDA vs. with various CDA during fuel-cut events.

The comparisons on overall  $CO_2$  emission is shown in Fig. 4.25. A detailed table of the  $CO_2$  percentage change is shown in Table 4.6. Similar to the fuel consumption, the reduced flow rate during fuel-cut events doesn't reduce the  $CO_2$  further for any of the strategies. All strategies'  $CO_2$  emissions are about 0.1% smaller than before implementing CDA, which is negligible.

**Table 4.6.** Changes on the  $CO_2$  emission under Otto-FTP cycle, after CDA implementation compared to before CDA, during fuel-cut events only.

Cases	Strategy 1	Strategy 2	Strategy 3	Strategy 4	Strategy 5
With CDA: 80% flow	-0.1%	-0.1%	-0.1%	-0.1%	-0.1%
With CDA: 70% flow	-0.1%	-0.1%	-0.1%	-0.1%	-0.1%
With CDA: 60% flow	-0.1%	-0.2%	-0.1%	-0.1%	-0.1%

The overall emission control performance of CDA-during-fuel-cut of 70% flow and 60% flow are shown in Fig. 4.26 and Fig. 4.27, respectively. A detailed table of the percentage



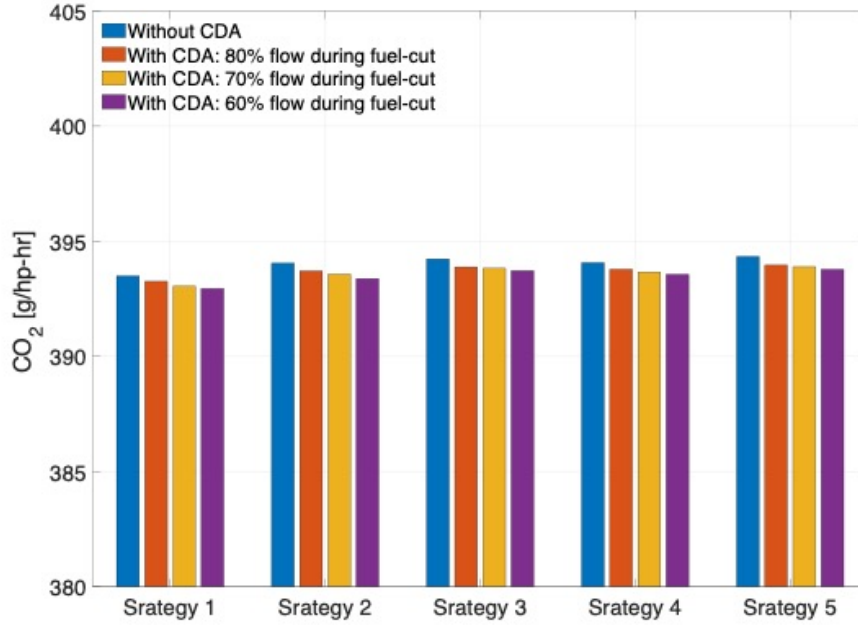


**Figure 4.25.**  $CO_2$  emission under Otto-FTP cycle, without CDA vs. with various CDA during fuel-cut events.

change of  $CO$ ,  $CH_4$  and  $NO_x$  emissions with various CDA flow reductions is shown in Table ??.

**Table 4.7.** Changes on the tailpipe emissions under Otto-FTP cycle, after CDA implementation compared to before CDA, during fuel-cut events only.

Cases	Strategy 1	Strategy 2	Strategy 3	Strategy 4	Strategy 5
$CO$ : CDA 80% flow	-1.2%	-4.0%	16.3%	3.5%	5.1%
$CO$ : CDA 70% flow	0.5%	11.9%	6.1%	2.9%	3.2%
$CO$ : CDA 60% flow	2.9%	2.8%	5.8%	2.3%	3.2%
$CH_4$ : CDA 80% flow	-6.9%	-4.1%	-7.7%	-8.7%	-8.7%
$CH_4$ : CDA 70% flow	-10.1%	-10.4%	-12.8%	-11.4%	-11.4%
$CH_4$ : CDA 60% flow	-18.9%	-10.2%	-16.3%	-14.4%	-14.9%
$NO_x$ : CDA 80% flow	-9.6%	-11.4%	-3.2%	-10.2%	-9.3%
$NO_x$ : CDA 70% flow	-10.7%	-17.7%	-6.9%	-9.4%	-15.6%
$NO_x$ : CDA 60% flow	-12.3%	-15.7%	-15.7%	-14.6%	-21.1%

By comparing CDA with various flow reductions with without CDA, same as stated before, the trends and differences among the 5 strategies still remains similar to what was

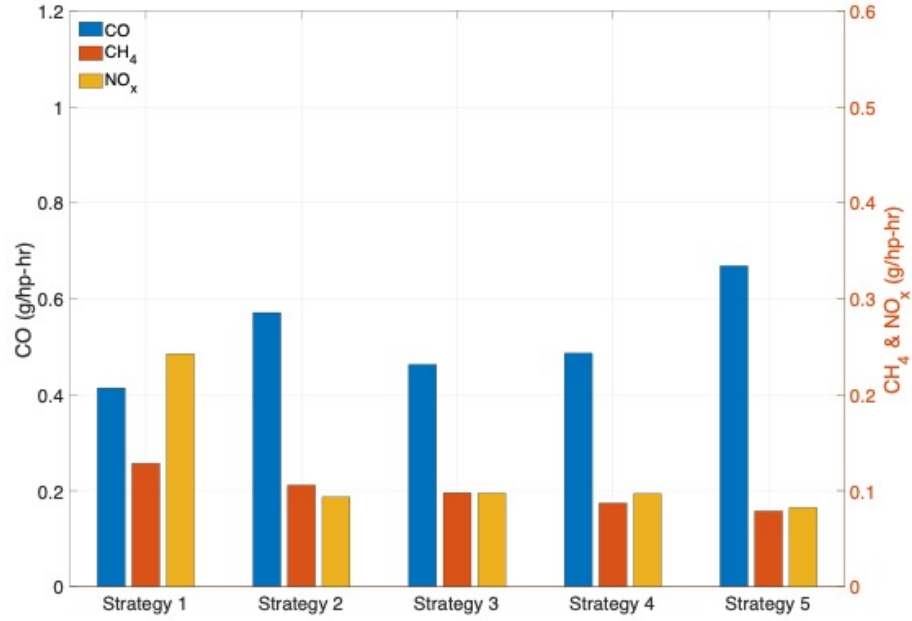


**Figure 4.26.** Tailpipe emissions under Otto-FTP cycle, with CDA of 70% flow during fuel-cut events.

before the CDA implementation. When looking at each strategy's emissions before and after CDA implementation, all strategies'  $CH_4$  and  $NO_x$  emissions are decreased with CDA implementation, mostly by 6% ~16%. Furthermore, the more reduced the mass flow during the fuel-cut events, the more the  $CH_4$  and  $NO_x$  emissions are decreased (or at least remains at the similar level). The  $CO$  emission is generally increased a little than before CDA, mostly by 2% ~6%, with 2 exceptions at more than 10%.

All the FOS-based controllers shows increasingly reduced  $CH_4$  and  $NO_x$  emissions with increasingly reduced mass flow during fuel-cut events. So it is recommended to have CDA implemented during fuel-cut for the sole purpose of reducing  $CH_4$  and  $NO_x$  emissions; and the more aggressive the CDA implementation, the more reduced the  $CH_4$  and  $NO_x$  emissions. However, it should be noted that, a more aggressive CDA implementation comes with a more radical transient change of dynamics and working environment during the process, which even if is theoretically feasible, can possibly cause other mechanical issues for longer term.

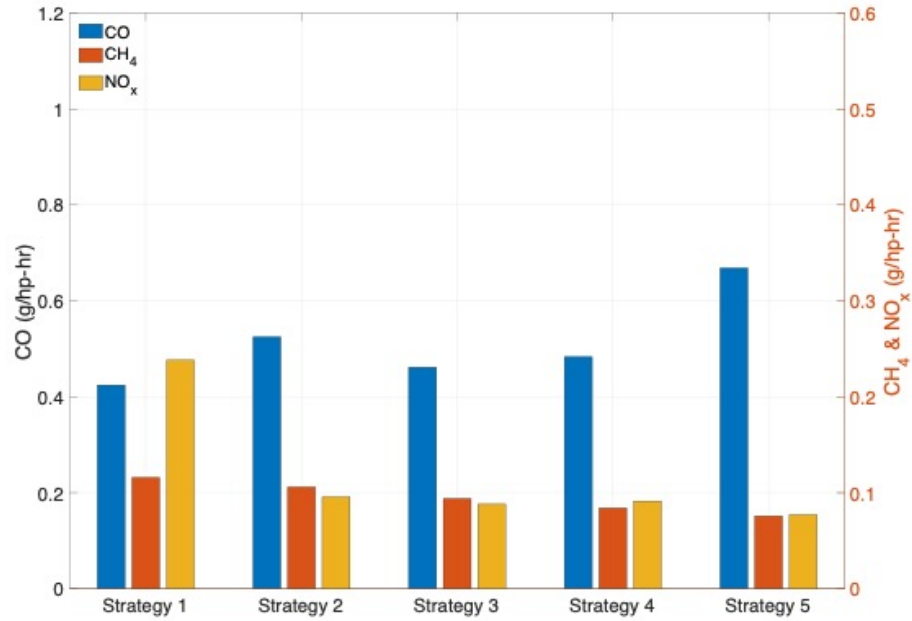


**Figure 4.27.** Tailpipe emissions under Otto-FTP cycle, with CDA of 60% flow during fuel-cut events.

Therefore, One should use caution when implement the CDA onto the engine in practice, and should start from a small reduced amount before increasing the CDA effort.

The next step (2nd part of the work) is to expand CDA implementation to low torque region. In this setup, a reduced mass flow rate mapping is implemented at below 150 Nm region, where the mass flow is reduced by 20% at 0 Nm by 5% at 150 Nm, with the flow reduction amount varying linearly with torque change.

The comparisons on overall fuel consumption is shown in Fig. 4.28. The CDA-on-fuel-cut-events-only with 80% flow is also included for reference. A detailed table of the percentage change of fuel consumption with different CDA implementation is shown in Table 4.8. There is a noticeable fuel reduction with full CDA implementation in low torque region, by around 2.4% for all strategies. This extra 2% of fuel reduction on top of the fuel-cut's fuel reduction is because of CDA's implementation at lower torque range causing a varying amount of mass flow reduction leading to less fuel consumption.

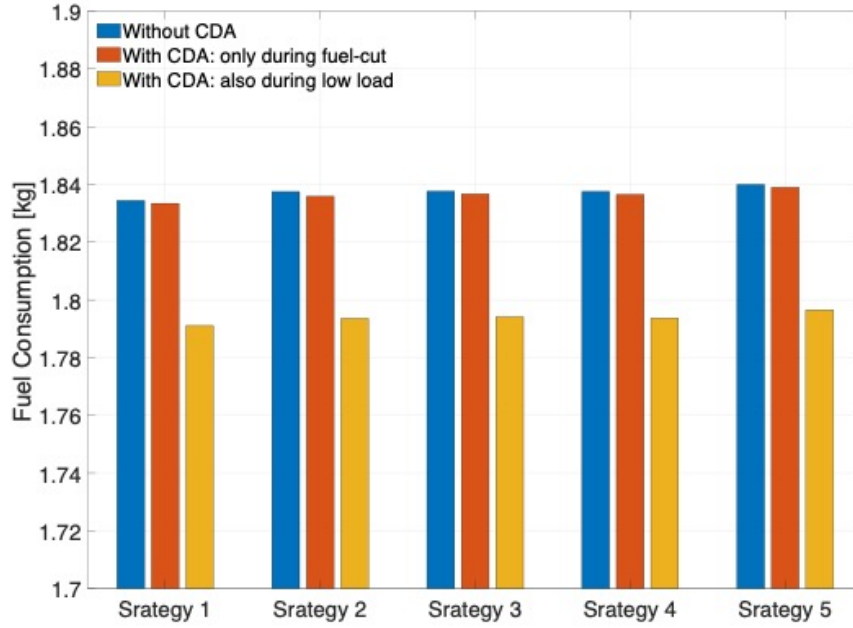


**Figure 4.28.** Fuel consumption under Otto-FTP cycle, without CDA vs. with CDA during fuel-cut events only vs. with full CDA.

**Table 4.8.** Changes on the fuel consumption under Otto-FTP cycle, after CDA implementation compared to before CDA.

Cases	Strategy 1	Strategy 2	Strategy 3	Strategy 4	Strategy 5
With CDA only at fuel-cuts	-0.1%	-0.1%	-0.1%	-0.1%	-0.1%
With full CDA at low torque	-2.4%	-2.4%	-2.4%	-2.4%	-2.4%

The comparisons on overall  $CO_2$  emission is shown in Fig. 4.29. The CDA-on-fuel-cut-events-only with 80% flow is also included for reference. A detailed table of the percentage change of  $CO_2$  emission with different CDA implementation is shown in Table 4.9. Again, similar to fuel consumption, there is a noticeable fuel reduction with full CDA implementation in low torque region, by around 2.4% for all strategies. This extra 2% of  $CO_2$  reduction on top of the fuel-cut’s  $CO_2$  reduction is beneficial environmentally.

The overall emission control performance improvement under Otto-FTP cycle is shown in Fig. 4.30. A detailed table of the percentage change of  $CO$ ,  $CH_4$  and  $NO_x$  emissions for the case “with CDA at fuel-cut events” and the case “with full CDA” compared with the case

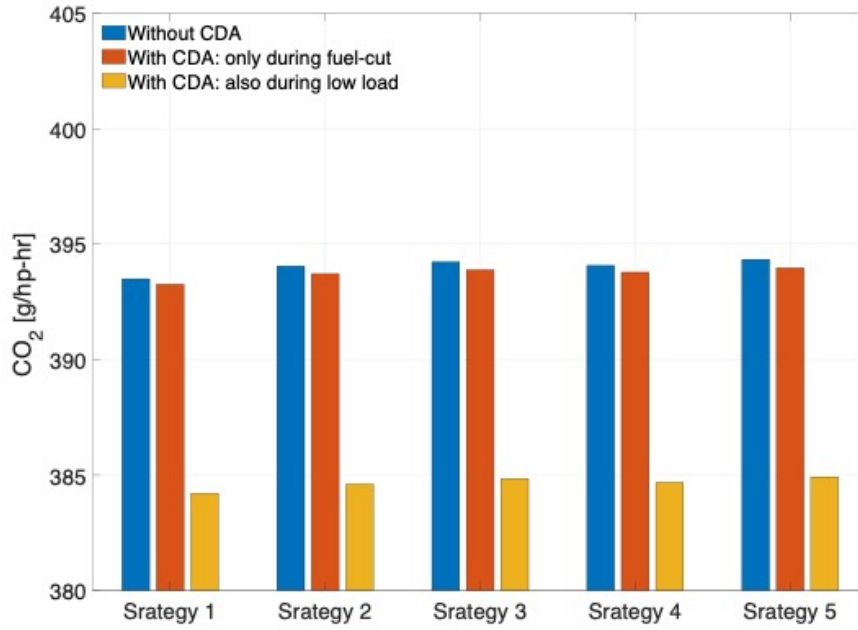


**Figure 4.29.**  $CO_2$  emission under Otto-FTP cycle, without CDA vs. with CDA during fuel-cut events only vs. with full CDA.

**Table 4.9.** Changes on the  $CO_2$  emission under Otto-FTP cycle, after CDA implementation compared to before CDA.

Cases	Strategy 1	Strategy 2	Strategy 3	Strategy 4	Strategy 5
With CDA only at fuel-cuts	-0.1%	-0.1%	-0.1%	-0.1%	-0.1%
With full CDA at low torque	-2.4%	-2.4%	-2.4%	-2.4%	-2.4%

“without CDA” is shown in Table 4.10. Firstly, same as before, the trends and differences among the 5 strategies still remains similar to what was before the CDA implementation. When looking at the statistics, the  $CH_4$  and  $NO_x$  emissions further reduce from CDA at fuel-cuts only, and they are all more than 9% less than what was before CDA implementation.

Therefore, for an engine with fuel cut-off feature, CDA can further improve the fuel economy at low torque ranges, on top of the already 2% fuel savings from engine fuel cut-off alone; at the same time, CDA can help reduce  $CH_4$  and  $NO_x$  emissions both during fuel-cut events and in low torque range. Environmentally (emission and fuel) and financially (fuel)

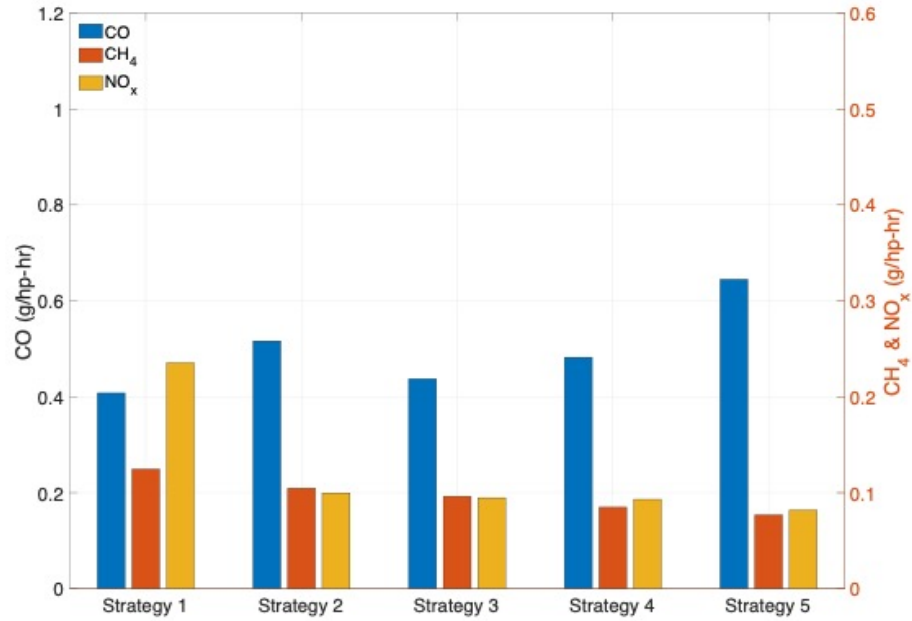


**Figure 4.30.** Tailpipe emissions under Otto-FTP cycle, with full CDA.

**Table 4.10.** Changes on the tailpipe emissions under Otto-FTP cycle, CDA during fuel-cut events only full CDA, compared to without CDA.

Cases	Strategy 1	Strategy 2	Strategy 3	Strategy 4	Strategy 5
<i>CO</i> : CDA only at fuel-cuts	-1.2%	-4.0%	16.3%	3.5%	5.1%
<i>CO</i> : full CDA at low torque	-1.1%	1.2%	0.3%	2.0%	-0.4%
<i>CH<sub>4</sub></i> : CDA only at fuel-cuts	-6.9%	-4.1%	-7.7%	-8.7%	-8.7%
<i>CH<sub>4</sub></i> : full CDA at low torque	-12.8%	-11.2%	-14.2%	-13.6%	-13.5%
<i>NO<sub>x</sub></i> : CDA only at fuel-cuts	-9.6%	-11.4%	-3.2%	-10.2%	-9.3%
<i>NO<sub>x</sub></i> : full CDA at low torque	-13.4%	-12.1%	-9.5%	-12.9%	-16.2%

speaking, CDA is beneficial and favored for implementation in internal combustion engines in general.

The third and last step is to implement the CDA to engine without fuel-cut feature as well, since it's shown its benefits for both fuel saving and emission reduction in engines with fuel-cut feature and is theoretically transferable to the non-fuel-cut case. So with the CDA implemented at low torque regions for engine without fuel-cuts, the comparisons on overall fuel consumption is shown in Fig. 4.31. A detailed table of the percentage change of

fuel consumption after CDA implementation is shown in Table 4.12. There is a noticeable fuel reduction with full CDA implementation in low torque region, by around 2.7% for all strategies. Similar to the engine with fuel-cut, this extra 2% of fuel reduction is because of CDA's implementation at lower torque range causing a varying amount of mass flow reduction leading to less fuel consumption.

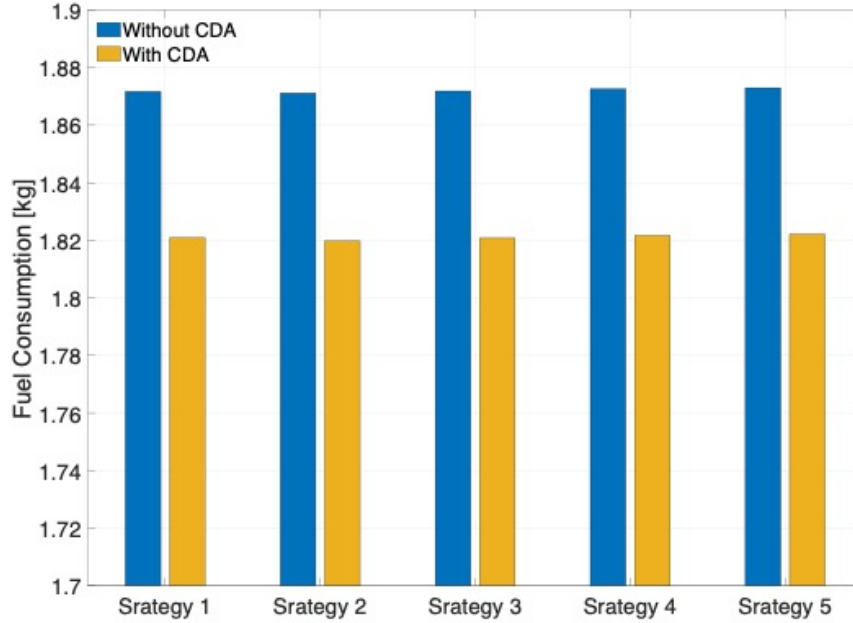


**Figure 4.31.** Fuel consumption under Otto-FTP cycle, without CDA vs. with full CDA, for engine without fuel-cut.

**Table 4.11.** Changes on the fuel consumption under Otto-FTP cycle, after CDA implementation compared to before CDA, for engine without fuel-cut.

Cases	Strategy 1	Strategy 2	Strategy 3	Strategy 4	Strategy 5
With full CDA at low torque	-2.7%	-2.7%	-2.7%	-2.7%	-2.7%

The comparisons on overall  $CO_2$  emission is shown in Fig. 4.32. A detailed table of the percentage change of  $CO_2$  emission after CDA implementation is shown in Table ???. As expected, there is a noticeable  $CO_2$  reduction with full CDA implementation in low torque region, by around 2.7% for all strategies.

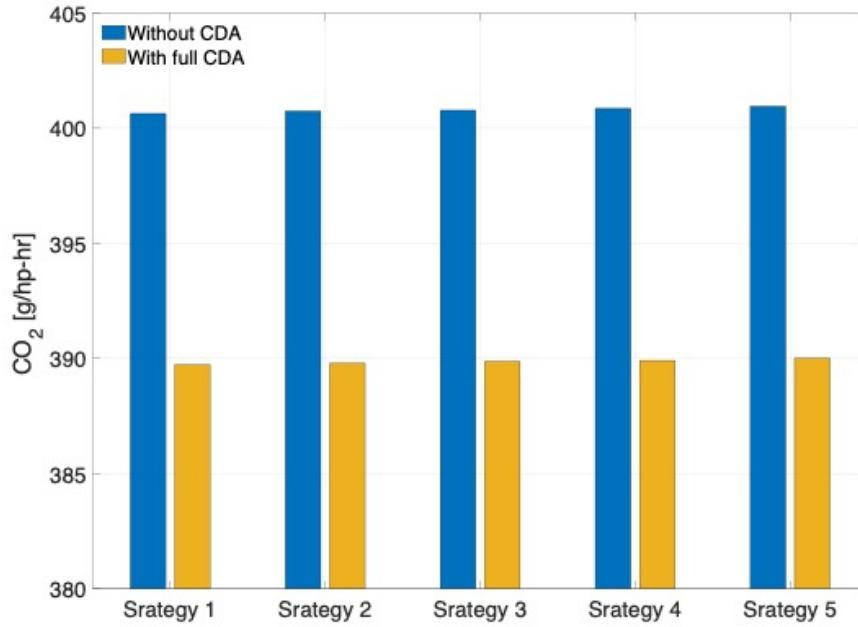


**Figure 4.32.**  $CO_2$  emission under Otto-FTP cycle, without CDA vs. with full CDA, for engine without fuel-cut.

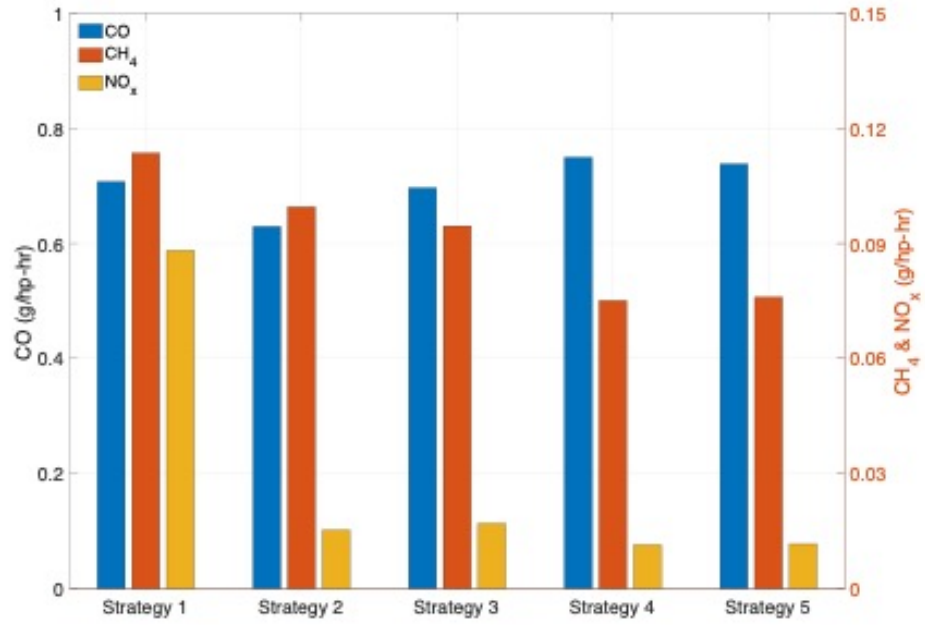
**Table 4.12.** Changes on the  $CO_2$  emission under Otto-FTP cycle, after CDA implementation compared to before CDA, for engine without fuel-cut.

Cases	Strategy 1	Strategy 2	Strategy 3	Strategy 4	Strategy 5
With full CDA at low torque	-2.7%	-2.7%	-2.7%	-2.7%	-2.7%

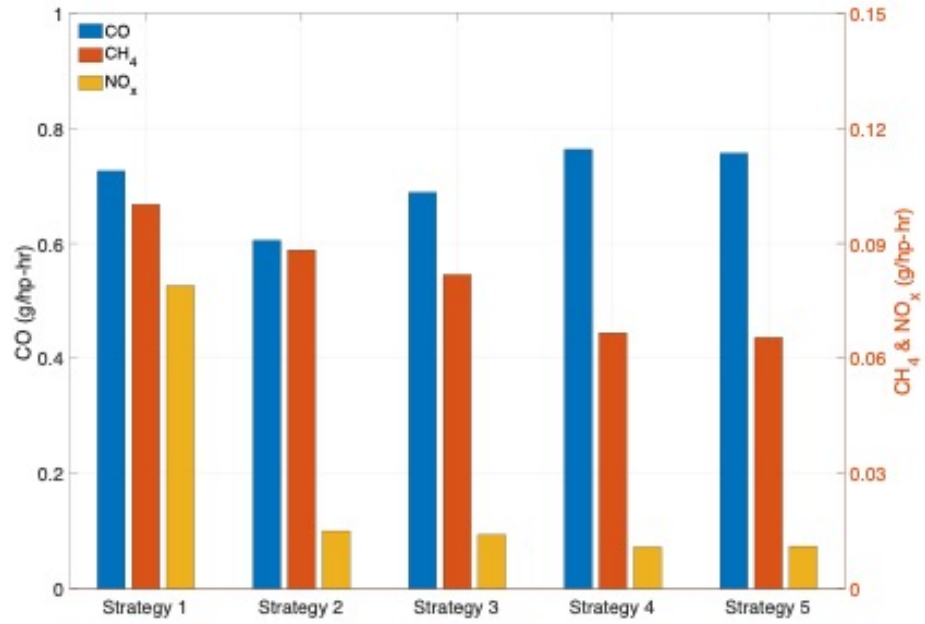
The overall emission control performance improvement under Otto-FTP cycle is shown in Fig. 4.33. The left figure is emission result of all 5 strategies without fuel cut-off, previously shown in Fig. 2.35 from Chapter 2, the right figure is the updated emission result of all 5 strategies without fuel cut-off, after the full CDA implementation at low torque range. By looking at Fig. 4.33b alone and in comparison with Fig. 4.33a, the trends and differences among the 5 strategies still remains similar to what was before the CDA implementation.

A detailed table of the percentage change of  $CO$ ,  $CH_4$  and  $NO_x$  emissions with full CDA compared with without CDA is shown in Table 4.13. As expected, the  $CH_4$  and  $NO_x$  emissions are both reduced from without CDA. The percentage of  $CH_4$  reductions are more than 11%, while the percentage of  $NO_x$  reductions are more than 10% for Strategies 1 & 3





(a) Without CDA implementation.



(b) With full CDA implementation.

**Figure 4.33.** Tailpipe emissions under Otto-FTP cycle, without CDA vs. with full CDA, for engine without fuel-cut.

and less than 6% for Strategies 2, 4 & 5. The percentage in  $NO_x$  is not as high as expected but they are based from an already very low emission database before CDA implementation.

**Table 4.13.** Changes on the tailpipe emissions under Otto-FTP cycle, with full CDA compared to without CDA, for engine without fuel-cut.

Cases	Strategy 1	Strategy 2	Strategy 3	Strategy 4	Strategy 5
$CO$ : full CDA	2.6%	-3.8%	-1.1%	1.9%	2.5%
$CH_4$ : full CDA	-11.8%	-11.3%	-13.4%	-11.2%	-13.8%
$NO_x$ : full CDA	-10.4%	-1.5%	-17.2%	-4.9%	-5.1%

From the work above, several conclusions can be drawn:

- Fuel cut-off feature is beneficial for fuel savings, by about 2% less than the same engine without fuel cut-off feature in Otto-FTP drive cycle. However, every-time during the fuel-cut events the TWC will be easily oxidized which leaves it incapable of reducing  $NO_x$  for a short period of time after the fuel-cut event, thus largely increase the  $NO_x$  emission compared with the same engine without fuel cut-off feature. Here we call it the “TWC over-oxidation” issue.
- Cylinder de-activation (CDA) is one of the VVA technologies where the engine shut off certain numbers of cylinders for the purpose of increasing active cylinder temperature, improving active cylinder combustion, and reducing fuel consumption. Implementing CDA only during fuel-cut events doesn’t further reduce fuel consumption, but helps reduce  $CH_4$  and  $NO_x$  emissions. The more aggressive the CDA is, in other words, the more restriction the CDA applies on the mass flow during fuel-cut events, the more emission reductions that we can possibly achieve. However, we wouldn’t want to go too aggressive on that path, because it, in practice, can cause some discontinuity, or even turbulence in the mass flow, which is undesirable.
- Implementing CDA at low torque range can help with both saving fuel (by more than 2%) and reducing  $CH_4$  and  $NO_x$  emissions, both for engine with fuel-cut and for engine without fuel-cut. It’s is proven in simulation results to be helpful for mitigating the “TWC over-oxidation” issue from fuel-cut.

## 5. SUMMARY AND FUTURE WORK

### 5.1 Summary

A novel two-loop estimation and control strategy is proposed to reduce the tail pipe emissions, with focus on the outer loop development. In the outer loop, an FOS estimator consisting of a TWC model and an extended Kalman-filter is used to estimate the real-time TWC fractional oxygen state (FOS), and a robust controller is used to control the TWC1's FOS by manipulating the desired engine  $\lambda$ . The outer loop estimator and controller are combined with an industry-production baseline inner loop controller, which controls the engine  $\lambda$  based on the desired  $\lambda$  value.

This novel control strategy is simulated with a high-fidelity TWC AVL Boost model under Otto-FTP drive cycle. The TWC AVL Boost model is built by our industrial partner and suggested for use as virtual truth reference for simulation verification. The simulation results of the proposed control strategy achieves good emission reduction performance and shows advantages over no-outer-loop control strategy and the conventional two-loop control strategies. The main takeaways from the work are:

1. Outer loop controller in general reduces more  $CH_4$  and  $NO_x$  emissions than not using outer loop feedback.  $CO$  emission is not reduced with outer loop controller since  $CO$ 's conversion efficiency is typically good at lean conditions and thus shows opposite trend than  $CH_4$  and  $NO_x$ .
2. FOS-based outer loop controllers gain better  $CH_4$  and  $NO_x$  emission reductions than  $\lambda_{dn}$ -based outer loop controllers. The advantage is much more significant for engine without fuel cut-off.
3. Cold start drive cycle would get worse emissions (for all three gases:  $CO$ ,  $CH_4$  and  $NO_x$ ) than warm start drive cycle. It is due to the fact that the beginning temperature is too low to activate catalyst reaction and require a significant amount of time to heat up both the engine and the catalyst. Low temperature is even more severe to  $CH_4$  reduction because  $CH_4$  (methane) requires even higher reaction temperature than other  $UHCs$ .
4. Fuel cut-off brings better fuel economy, but it has negative effect on after-treatment emission control because of TWC over-oxidation. By comparing simulation results with and

without fuel cut-off, it shows huge potential for much better emission result if fuel cut-off's side effect can be resolved or at least alleviated.

An industry-production Cummins B6.7N natural gas SI engine was installed in the Ray W. Herrick Laboratories for study of variable valve actuation (VVA) technologies, for the purpose of evaluating/improving stoichiometric SI engine's fuel efficiency, emission reduction, and engine knock resistance. A one-dimensional, physics-based natural gas SI engine model was investigated and calibrated. To calculate the burn rates in the cylinder, three different pressure analysis methods were investigated and implemented. It is observed that all six cylinders' pressure curves are different, which in turn renders different burn rates cylinder-to-cylinder. Cylinders with higher peak cylinder pressure have a faster burn rate. Each operating condition has its unique pressure curve, and their burn rates are different under different operating conditions. Considering that the burn rate profile can vary cylinder-to-cylinder and operation-to-operation, to make the GT combustion model work for a larger range of loads, a fixed burn rate model may help in the preliminary research phase, but a predictive combustion model is much more preferable.

Variable valve actuation (VVA) technologies consist of a range of technologies varying variable valve event timing, duration and/or lift. The intake valve closure (IVC) modulation and cylinder de-activation (CDA) are investigated in this work through the calibrated and updated GT model. IVC modulation affects engine performance by changing the intake valves' closure timing. A proper IVC modulation can be helpful in improving the open cycle efficiency and brake thermal efficiency, as well as improving the fuel economy. CDA modulation is mostly beneficial in the low torque region where certain numbers of cylinders are de-activated, and thus reduce the overall mass flow for fuel economy. CDA can also improve the closed cycle efficiency (CCE) by reducing heat transfer losses, and improve open cycle efficiency (OCE) by reducing pumping losses while increasing gross power output, which in consequence improves the overall brake thermal efficiency (BTE). The CDA is also implemented on the engine from the TWC FOS work, where it shows benefit to the entire system by both reducing fuel consumption and reducing the  $CH_4$  &  $NO_x$  emissions.

## 5.2 Future work

The natural gas VVA project is still at its early phase, and there are a lot of potentials and opportunities in this project to discover and study about. The calibrated GT model is expected to serve as a virtual testing and verification tool to help with the project in conducting preliminary verification and provide data at certain positions where the test cell may have difficulty in accessing. With more test cell VVA results available, some minor calibration can be done on the GT model, including the effects of VVA on spark timing, boundary condition, as well as controller priorities and inter-correlation, etc.

The implemented CDA for outer-loop TWC control, although simplified and not having made full use of the GT model, has already shown the benefit of the CDA with the preliminary results. In the future when the natural gas VVA system in the test cell is calibrated, the group can install the after-treatment three-way catalyst (TWC) and emission measurement system to either build our own virtual TWC model from experimental data, or conduct hardware-in-loop experiment with the MATLAB/Simulink based outer loop controller. It will be very exciting to physically combine both inner (engine) loop and outer (TWC) loop control strategies in the test cell.

## REFERENCES

- [1] J. B. Heywood, *Internal combustion engine fundamentals*. McGraw-Hill Education, 2018.
- [2] L. Farrell, “Integrating ultra-low nox technology presents challenges,” SAE COMVEC Digital Summit, Tech. Rep., 2020.
- [3] A. Raj, “A review of mobile and stationary source emissions abatement technologies for natural gas engines,” *Johnson Matthey Technol Rev*, vol. 60, no. 4, pp. 228–235, 2016.
- [4] P. Nevalainen, N. M. Kinnunen, A. Kirveslahti, *et al.*, “Formation of nh<sub>3</sub> and n<sub>2</sub>o in a modern natural gas three-way catalyst designed for heavy-duty vehicles: The effects of simulated exhaust gas composition and ageing,” *Applied Catalysis A: General*, vol. 552, pp. 30–37, 2018.
- [5] L. Eriksson and L. Nielsen, *Modeling and control of engines and drivelines*. John Wiley & Sons, 2014.
- [6] T. S. Auckenthaler, *Modelling and control of three-way catalytic converters*. ETH Zurich, 2005.
- [7] J. Gong, D. Wang, J. Li, N. Currier, and A. Yezerets, “Dynamic oxygen storage modeling in a three-way catalyst for natural gas engines: A dual-site and shrinking-core diffusion approach,” *Applied Catalysis B: Environmental*, vol. 203, pp. 936–945, 2017.
- [8] D. N. Tsinoglou, G. C. Koltsakis, and J. C. Peyton Jones, “Oxygen storage modeling in three-way catalytic converters,” *Industrial & engineering chemistry research*, vol. 41, no. 5, pp. 1152–1165, 2002.
- [9] P. Kumar, I. Makki, J. Kerns, K. Grigoriadis, M. Franchek, and V. Balakotaiah, “A low-dimensional model for describing the oxygen storage capacity and transient behavior of a three-way catalytic converter,” *Chemical engineering science*, vol. 73, pp. 373–387, 2012.
- [10] R. J. Möller, “Modeling and control of three-way catalysts,” Ph.D. dissertation, ETH Zurich, 2009.
- [11] L. Guzzella and C. Onder, *Introduction to modeling and control of internal combustion engine systems*. Springer Science & Business Media, 2009.

- [12] G. Fiengo, J. W. Grizzle, J. A. Cook, and A. Y. Karnik, "Dual-uego active catalyst control for emissions reduction: Design and experimental validation," *IEEE Transactions on Control Systems Technology*, vol. 13, no. 5, pp. 722–736, 2005.
- [13] R. W. Schallock, K. R. Muske, and J. C. P. Jones, "Model predictive functional control for an automotive three-way catalyst," *SAE International Journal of Fuels and Lubricants*, vol. 2, no. 1, pp. 242–249, 2009.
- [14] P. Kumar and I. Makki, "Model based control of a three-way catalytic converter based on the oxygen storage level of the catalyst," SAE Technical Paper, Tech. Rep., 2017.
- [15] E. P. Brandt, Y. Wang, and J. W. Grizzle, "Dynamic modeling of a three-way catalyst for si engine exhaust emission control," *IEEE Transactions on control systems technology*, vol. 8, no. 5, pp. 767–776, 2000.
- [16] E. P. Brandt, *Modeling and diagnostics of three-way catalysts for advanced emissions control systems*. University of Michigan, 1998.
- [17] K. Shiki and T. Iura, *Fuel cut-off device for internal combustion engine*, US Patent 4,638,781, Jan. 1987.
- [18] S. Kaleemuddin, S. Shaikh, and S. Bhattacharya, "Experimental study on two-cylinder direct injection diesel engine for bs-iii emission compliant," *Innovations in Fuel Economy and Sustainable Road Transport*, p. 211, 2011.
- [19] D. B. Gosala, C. M. Allen, A. K. Ramesh, *et al.*, "Cylinder deactivation during dynamic diesel engine operation," *International Journal of Engine Research*, vol. 18, no. 10, pp. 991–1004, 2017.
- [20] K. R. Vos, G. M. Shaver, M. C. Joshi, and J. McCarthy Jr, "Implementing variable valve actuation on a diesel engine at high-speed idle operation for improved aftertreatment warm-up," *International Journal of Engine Research*, vol. 21, no. 7, pp. 1134–1146, 2020.
- [21] C. M. Allen, M. C. Joshi, D. B. Gosala, G. M. Shaver, L. Farrell, and J. McCarthy, "Experimental assessment of diesel engine cylinder deactivation performance during low-load transient operations," *International Journal of Engine Research*, vol. 22, no. 2, pp. 606–615, 2021.

## VITA

# Yunpeng Xu

Ray W. Herrick Laboratories

177 S. Russell St.

West Lafayette, IN 47907-2099

Cell: 317-987-6660

Email: [xu967@purdue.edu](mailto:xu967@purdue.edu)

LINKEDIN: <https://www.linkedin.com/in/yunpengxu/>

### Current position

*Ph.D. candidate*, School of Mechanical Engineering, Purdue University

### Areas of specialisation

PID Control; MIMO Control; Modeling and Simulation;

Internal Combustion Engine and After-treatment Systems.

### Previous Education

2014-2016 MENG in Mechanical Engineering, IMT Mines Alès

2010-2014 BENG in Mechanical Engineering, Shanghai Jiao Tong University

### Courses in Plan of Study

ME500: Advanced Thermodynamics

ME563: Mechanical Vibrations

ME575: Design Control Systems



ME584: System Identification

ME689: Adaptive Control

ECE569: Introduction to Robotic Systems

ECE600: Random Variables

ECE675: Introduction to Analysis of Nonlinear Systems

MA511: Linear Algebra Applications

MA514: Numerical Analysis